

博士論文

**Study on Hydrogen Selective Silica-based Membrane
for Ethane Dehydrogenation over Cr/ZSM-5 Catalyst**

(ZSM-5 担持クロム触媒を用いたエタンの脱水素化の膜反応器に関する研究)

安 少珍

Thesis Evaluation Committee

Professor Kazunari Domen, The University of Tokyo

Professor Akiyoshi Sakoda, The University of Tokyo

Professor Yoshiko Tsuji, The University of Tokyo

Professor Ryuji Kikuchi, The University of Tokyo

Professor Kazuki Akamatsu, Kogakuin University

Professor S. Ted Oyama (Supervisor), The University of Tokyo

Acknowledgements

First of all, I would like to express my sincere gratitude to my advisor, Prof. S. Ted Oyama for his guidance, thoughtful advice, continuous support and encouragements. I also appreciate the efforts made by the evaluation committee, Prof. Kazunari Domen, Prof. Akiyoshi Sakoda, Prof. Yoshiko Tsuji, Prof. Ryuji Kikuchi and Prof. Kazuki Akamatsu.

During my PhD course, I had a lot of help from all the members of Oyama-Kikuchi laboratory. Especially I would like to show my sincere gratitude to Prof. Riyuji Kikuchi, Dr. Atsushi Takagaki and Mr. Takashi Sugawara for their careful advice and continuous encouragement. Especially I would like to show my sincere gratitude to Dr. Bando, Dr. Tyron, Dr. Souha, Kageyama, Aono for their help and comment for my research. I also thanks to our past and current group members for their help and kindness.

Whenever I had a hard time, my family was always beside of me. I would like to give special gratitude and love to my family, Heung-Gyu Ahn, Byeong-Sun Lee and So-Hee Ahn for their sacrifices and understandings. I also appreciate my family in law their support and encouragement. Without my family, it would have been difficult to finish my course.

Finally, I would like to give my special thanks to my husband, Gwang-Nam, for his love, the continuous encouragement and understandings all of my research and life. Without his sacrifices throughout my life in Japan, this thesis would not have been possible. I also thanks to α -5 members, Hyemin, Jeonghyun, Saemi and Soomin, for their encouragement. All the time I had with α -5 made me happy and allowed me to come here.

Abstract

Ethylene is one of the most important petrochemicals due to its extensive use as feedstock for the production of a vast array of chemicals. Catalytic dehydrogenation of ethane is considered efficient technology for producing ethylene with hydrogen as a byproduct, an important reagent in refineries. A membrane reactor combined the reaction has advantages not only separate products, but also overcome the equilibrium limitation of the reaction by extracting hydrogen continuously from the catalyst bed.

This dissertation describes preparation and characterization of silica-based inorganic membranes and their application in membrane reactor for dehydrogenation of ethane, which is equilibrium limited reaction and required enhancement of ethylene yield. First, silica-based membranes were developed to improve their permeability and hydrothermal stability by modifying precursors using chemical vapor deposition (CVD) method. The morphology and structure of prepared silica-based membranes were discussed, and permeance mechanisms of small and large gases through the membranes were studied with experimental and simulated data. Second, the effect of various reaction conditions, including feed flow rates, pressures and temperatures on dehydrogenation of ethane over Cr/ZSM-5 catalyst were investigated in a conventional packed-bed reactor (PBR) and in a membrane reactor (MR) fitted with modified silica membranes. A performance of membrane reactor was evaluated by model simulation with various H_2 permeances and H_2/C_2H_6 selectivities.

Contents

| | |
|---|-----------|
| Chapter 1 General Introduction | 1 |
| 1.1. Global ethylene production | 1 |
| 1.1.1. General ethane dehydrogenation | 2 |
| 1.1.2. Ethane dehydrogenation assisted with CO ₂ | 4 |
| 1.2. Hydrogen selective inorganic membrane | 5 |
| 1.2.1. Silica-based membranes | 6 |
| 1.2.2. Hydrothermal stability of silica-based membranes | 7 |
| 1.2.3. Pore size controlled silica-based membranes | 7 |
| 1.3. Mechanisms of gas permeation through inorganic membranes | 10 |
| 1.3.1. Hagen-Pouisselle mechanism | 10 |
| 1.3.2. Knudsen diffusion mechanism | 12 |
| 1.3.3. Surface diffusion mechanism | 12 |
| 1.3.4. Gas-translational mechanism | 13 |
| 1.3.5. Solid-state diffusion mechanism | 13 |
| 1.4. Catalytic membrane reactor for ethane dehydrogenation | 14 |
| 1.5. Outline of the dissertation | 15 |
| | |
| Chapter 2 Permeation Properties of Silica-Zirconia Composite Membranes | |
| Supported on Porous Alumina Substrates | 25 |
| 2.1. Introduction | 25 |
| 2.2. Experimental | 29 |
| 2.2.1. Preparation of γ -alumina intermediate layer | 29 |
| 2.2.2. Preparation of silica-zirconia composite membranes | 30 |

| | |
|--|----|
| 2.2.3. Characterization | 32 |
| 2.2.4. Permeance and hydrothermal stability measurements | 32 |
| 2.3. Results and discussion | 33 |
| 2.3.1. Preparation of silica-zirconia composite membranes | 33 |
| 2.3.2. Morphology and structure of the silica-zirconia membranes | 37 |
| 2.3.3. Permeation mechanism through silica-zirconia membrane | 38 |
| 2.3.4. Hydrothermal stability of silica-zirconia composite membranes | 44 |
| 2.4. Conclusions | 46 |

Chapter 3 Synthesis and Characterization of Hydrogen Selective Silica

Membrane Prepared by Chemical Vapor Deposition of

Vinyltriethoxysilane 51

| | |
|---|----|
| 3.1. Introduction | 51 |
| 3.2. Experimental | 55 |
| 3.2.1. Preparation and characterization of VTES-derived silica membrane | 55 |
| 3.2.2. Fourier transform infrared (FTIR) analysis | 58 |
| 3.2.3. Permeance and hydrothermal stability test for VTES-derived silica membrane | 59 |
| 3.3. Results and discussion | 60 |
| 3.3.1. Preparation of VTES-derived membrane | 60 |
| 3.3.2. Morphology and structure of VTES-derived membrane | 61 |
| 3.3.3. Hydrothermal stability of the VTES-derived membrane | 63 |
| 3.3.4. Permeation mechanism through the VTES-derived membrane before and after hydrothermal stability test | 65 |

| | |
|---|------------|
| 3.4. Conclusions | 71 |
| Chapter 4 Dehydrogenation of Ethane over Cr/ZSM-5 Catalyst in a Hydrogen Selective Silica Membrane Reactor | 77 |
| 4.1. Introduction | 77 |
| 4.2. Experimental | 79 |
| 4.2.1. Preparation and characterization of the silica membrane | 79 |
| 4.2.2. Preparation and characterization of Cr/ZSM-5 catalyst | 79 |
| 4.2.3. Reactivity test with catalytic membrane reactor | 80 |
| 4.2.4. Modeling of ethane dehydrogenation in a membrane reactor | 83 |
| 4.3. Results and discussion | 85 |
| 4.3.1. Preparation of VTES-derived membrane | 85 |
| 4.3.2. Characterization of catalyst | 86 |
| 4.3.3. Catalytic performance of 5 wt% Cr/ZSM-5 in dehydrogenation of ethane | 89 |
| 4.3.4. Effect of feed flow rate on ethane dehydrogenation in PBR and MR | 90 |
| 4.3.5. Effect of total pressure on ethane dehydrogenation in PBR and MR | 93 |
| 4.3.6. Effect of temperature on ethane dehydrogenation in PBR and MR | 94 |
| 4.3.7. Effect of membrane properties on yield enhancement | 97 |
| 4.4. Conclusions | 99 |
| Chapter 5 General Conclusions | 101 |

List of Tables

| | | |
|------------------|---|----|
| Table 2.1 | Past work on silica-zirconia membranes | 28 |
| Table 2.2 | CVD conditions for the preparation of membranes | 31 |
| Table 2.3 | Calculated parameters for the silica-zirconia composite membrane (solubility site model) | 41 |
| Table 2.4 | Activation energy and pre-exponential factor, $k_{0,i}$, for silica-zirconia composite membrane (gas translational method) | 43 |
| Table 3.1 | Calculated parameters for the VTES-derived membrane based on the surface diffusion model | 68 |
| Table 3.2 | Calculated parameters for the VTES-derived membrane based on the gas-translational model | 70 |
| Table 3.3 | Calculated parameters for the VTES-derived membrane based on the gas-translational model | 70 |
| Table 4.1 | Model equations for the one-dimensional model | 81 |
| Table 4.2 | Reaction rate expression and kinetic parameters for ethane dehydrogenation | 82 |
| Table 4.3 | BET surface areas, pore volumes and crystallite size of the ZSM-5 support, and the fresh and spent Cr/ZSM-5 catalyst samples | 87 |
| Table 4.4 | Curve-fitting results for Cr/ZSM-5 catalyst after pretreatment | 88 |
| Table 4.5 | Enhancement of C ₂ H ₄ yield for dehydrogenation of ethane in membrane reactor with different membranes at 823 K and 0.1 MPa with 20 cm ³ min ⁻¹ of 20 % ethane | 97 |

List of Figures

| | | |
|-------------------|---|----|
| Figure 1.1 | Ethylene production capacity | 1 |
| Figure 1.2 | Illustration of general ethane dehydrogenation | 2 |
| Figure 1.3 | Illustration of CO ₂ -assisted ethane dehydrogenation | 4 |
| Figure 1.4 | Various gas separation mechanisms through inorganic membranes | 11 |
| Figure 2.1 | Experimental setup for chemical vapor deposition (CVD) process and permeability test (Conditions: CVD and hydrothermal stability test at 923 K, 101 kPa, permeance test at 923 K, $\Delta P = 0.24$ MPa) | 31 |
| Figure 2.2 | Changes in H ₂ and N ₂ permeance and H ₂ /N ₂ selectivity with CVD time (923 K, $\Delta P = 0.24$ MPa). (a) Pure silica membrane (b) 025Si-Zr (c) 05Si-Zr (d) 10Si-Zr (e) 15Si-Zr | 35 |
| Figure 2.3 | Permeation properties of membranes with the different molar ratios of ZTB/TEOS of 0-0.15 (923 K, $\Delta P = 0.24$ MPa) | 36 |
| Figure 2.4 | SEM images of the silica-zirconia composite membrane. (a) cross-section of the γ -alumina intermediate layer coated on macroporous α -alumina support (b) cross-section of the membrane 10Zr-Si (c) surface of the membrane 10Zr-Si | 37 |
| Figure 2.5 | Permeance of various gases as a function of kinetic diameter at 923 K and $\Delta P = 0.24$ MPa | 38 |

| | | |
|-------------------|--|----|
| Figure 2.6 | Temperature dependence of the permeances of He, Ne and H ₂ through the 10Si-Zr membrane (solubility site model) | 39 |
| Figure 2.7 | Temperature dependence of the permeances of He, Ne and H ₂ through the 10Si-Zr membrane (gas translational model) | 42 |
| Figure 2.8 | Effect of water upon H ₂ and N ₂ permeances. Pure silica and silica-zirconia composite membranes prepared using different molar ratios of ZTB/TEOS. Exposure to 16 mol% of water vapor at 923 K and 101 kPa for 48 h. (a) Changes of H ₂ permeance (top) (b) Changes of N ₂ permeance (bottom) | 45 |
| Figure 3.1 | Comparison of H ₂ permeance for various silica membranes as a function of their estimated pore size | 52 |
| Figure 3.2 | Schematic of experimental setup for membrane preparation and testing (a) Chemical vapor deposition (CVD) process and hydrothermal stability test (873 K, 0.1 MPa) (b) Permeability test (473-873 K, $\Delta P = 0.25$ MPa) | 56 |
| Figure 3.3 | Schematic of experimental setup for the FTIR apparatus | 58 |
| Figure 3.4 | Changes in H ₂ and N ₂ permeance and H ₂ /N ₂ selectivity with CVD time (CVD conditions: 873 K, 0.25 MPa) | 60 |
| Figure 3.5 | SEM images of the cross-section of the VTES-derived silica membrane. (a) Overall structure at low magnification (b) Surface layer at high magnification | 62 |
| Figure 3.6 | Infrared spectra of the calcined γ -alumina disk before and after CVD, after 1h exposure Ar and 1 h exposure 16 mol% water. All treatments and measurements were carried out at 873 K | 63 |

| | | |
|-------------------|--|----|
| Figure 3.7 | Changes in the H ₂ and N ₂ permeances of the VTES-derived silica membrane with exposure to 16 mol% of water vapor at 873 K for 72 h | 64 |
| Figure 3.8 | Temperature dependence of the permeances of various gases through the VTES-derived membrane before (a) and after (b) the hydrothermal stability test at 873 K with 16 mol% of water vapor | 65 |
| Figure 4.1 | Schematic of catalytic membrane reactor for ethane dehydrogenation | 81 |
| Figure 4.2 | Schematic reaction model for simulations | 83 |
| Figure 4.3 | Permeance of various gases before and after CVD (CVD temperature: 873 K, measurement temperature: 573 K) | 84 |
| Figure 4.4 | XRD patterns of ZSM-5 support, fresh and spent Cr/ZSM-5 catalysts | 86 |
| Figure 4.5 | (a) XANES spectra of the Cr/ZSM-5 catalyst after He treatment at 298-823 K and (b) EXAFS spectra after He treatment at 823 K. Spectra were taken at room temperature. | 87 |
| Figure 4.6 | Conversion of C ₂ H ₆ and yields of C ₂ H ₄ , H ₂ and CH ₄ as a function of time for the dehydrogenation of ethane in the PBR with 20 cm ³ min ⁻¹ of 20% C ₂ H ₆ diluted in Ar at 823 K and 0.1 MPa. | 89 |
| Figure 4.7 | Conversion of C ₂ H ₆ and yields of C ₂ H ₄ , H ₂ and CH ₄ for dehydrogenation of ethane at feed flow rates in the range of 20-100 cm ³ min ⁻¹ at 823 K and 0.1 MPa using 20 % C ₂ H ₆ diluted in | 91 |

Ar. (a) PBR (b) MR (c) Yield enhancement and H₂ permeance as feed flow fate

- Figure 4.8** Conversion of C₂H₆ and yields of C₂H₄, H₂ and CH₄ for dehydrogenation of ethane at various total pressures 0.1-0.5 MPa and 823 K. (a) PBR (b) MR (c) Yield enhancement and H₂ permeance as feed total pressure 92
- Figure 4.9** Productivity of H₂ for dehydrogenation of ethane in the MR and PBR at various total pressures 0.1-0.5 MPa and 823 K. 94
- Figure 4.10** Conversion of C₂H₆ and yields of C₂H₄, H₂ and CH₄ for dehydrogenation of ethane at various temperatures from 723 K to 823 K and 0.1 MPa. (a) PBR (b) MR (c) Yield enhancement and H₂ permeance as temperature 96
- Figure 4.11** Experimental and calculated values of the C₂H₄ yield as a function of contact time (top) and the enhancement of C₂H₄ as a function of OLC (bottom) 98

List of Abbreviations

| | |
|--------|------------------------------------|
| BTESE | bis(triethoxysilyl)ethane |
| BTESM | bis(triethoxysilyl)methane |
| CVD | Chemical vapor deposition |
| DMDPS | Dimethoxydiphenylsilane |
| DTEOS | Dodecyltriethoxysilane |
| FTIR | Fourier transform infrared |
| HEDS | Hexaethoxydisiloxane |
| MR | Membrane reactor |
| MTMOS | Methyltrimethoxysilane |
| NKP | Normalized Knudsen-based permeance |
| OLC | Operability level coefficient |
| PBR | Packed-bed reactor |
| PhTMOS | Phenyltrimethoxysilane |
| PrTMOS | Propyltrimethoxysilane |
| PTMS | Phenyltrimethoxysilane |
| PVA | Polyvinyl alcohol |
| SEM | Scanning electron microscopy |
| TEDMDS | Tetraethoxydimethyldisiloxane |
| TEOS | Tetraethylorthosilicate |
| TMMOS | Trimethylmethoxysilane |
| TMOS | Tetramethoxysilane |
| TPMS | Triphenylmethoxysilane |

| | |
|-------|--------------------------------------|
| VTES | Vinyltriethoxysilane |
| XANES | X-ray absorption near edge structure |
| ZTB | Zirconium (IV) <i>tert</i> -butoxide |

Chapter 1

General Introduction

1.1. Global ethylene production

Ethylene is an important petrochemical compound which is extensively used as feedstock for production of several chemicals, including polymers (e.g., polyethylene, polyester, and polystyrene), oxygenates (e.g., ethylene oxide, ethylene glycol, and acetaldehyde), and chemical intermediates (e.g., ethyl benzene and ethylene dichloride). The global ethylene capacity has been steadily increasing across the world, rising from 80 million tons in 1995 to 165 million tons in 2015, as shown in Figure 1.1 [1].

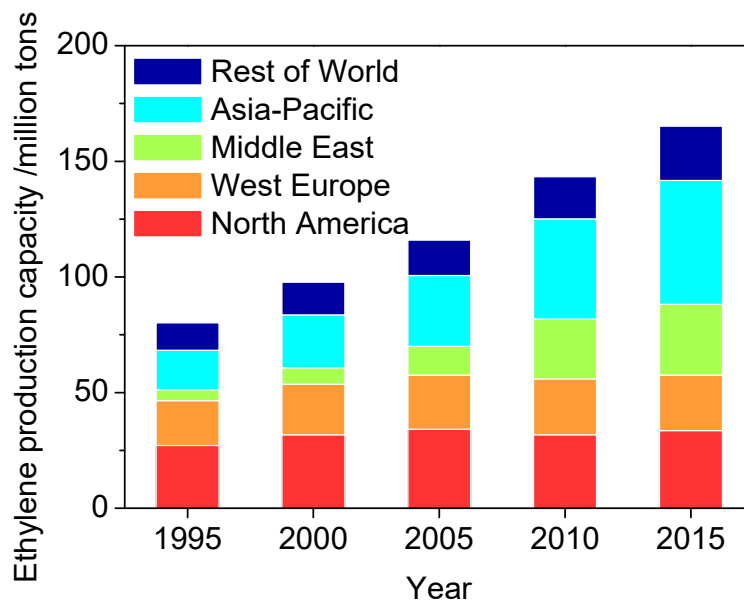


Figure 1.1. Ethylene production capacity

Nature gas is the main feedstock in production of ethylene because it contains ethane (2.5 %) and is one of the cleanest and safest. Furthermore, price of the natural gas was gradually alleviated due to imposition of shale gas, which also contains ethane [2].

Steam cracking is the most common process used to produce olefins such as ethylene, propylene and butadiene from a wide range of hydrocarbon feedstock, such as gaseous feedstock (ethane and propane) and heavier feedstock (naphtha, gas oil and gas condensates). However, this process faces several challenges, such as high-energy demand (high operation temperature around 1123 K), low selectivity with substantial production of methane and coke as byproducts, depletion of petroleum reserves, and increasing oil price.

In this respect, catalytic dehydrogenation of ethane has been proposed as an alternative for ethylene production due to the process being less energy intensive (lower operation temperatures around 973-1073 K), the high availability of relatively cheap natural gas and shale gas, specifically ethane, and the exclusive ethylene yield.

1.1.1. General ethane dehydrogenation

General dehydrogenation is a one-step reaction involving the conversion of ethane to the corresponding ethylene and hydrogen as illustrated in Figure 1.2.

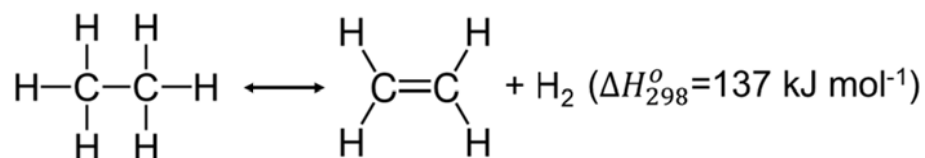


Figure 1.2. Illustration of general ethane dehydrogenation

Typically, two types of catalysts, noble metal (Pt) and metal oxides (CrO_x , GaO_x , VO_x , MoO_x , and InO_x), have been extensively studied for the general dehydrogenation reaction. Platinum is the most effective metal due to its superior activity for the activation of paraffinic C-H bonds and low activity for C-C bond cleavage [2]. However, re-adsorption of ethylene on pure Pt surface results in low ethylene selectivity and rapid coke deposition, leading to catalyst deactivation [3]. For that reason, Pt is alloyed with a second metal, such as Sn, Ga, In, etc. to make the catalyst less prone to deactivation by coke deposition. The group of Bell recently studied various Pt-based bimetallic catalysts, including PtSn/Mg(Al)O [4], PtGa/Mg(Al)O [5,6], and PtIn/Mg(Al)O [7] for ethane dehydrogenation. The authors reported that the activity and selectivity of a novel Pt/Mg(In)(Al)O catalyst are strongly affected by In/Pt ratio, in which a In/Pt ratio of 0.48 presented the highest activity ($29 \mu\text{mol s}^{-1} \text{ g}_{\text{cat.}}^{-1}$) and selectivity (100 %) [7]. Both geometric and electronic effects of the second metals have been proposed to explain their roles in modifying the catalyst surface and changing the surface chemistry involved in ethane dehydrogenation [8]. Their recent study about effect of metal particle size of platinum catalysts suggests that small and Sn-promoted catalyst should be used to avoid coke formation [9]. This result was supported by quantum calculations by the same group, which revealed that the presence of Sn on the surface of Pt enhances the dissociative adsorption of ethane but suppresses the adsorption of ethylene [10].

Chromium oxides have also been reported as effective catalysts for ethane dehydrogenation by several researchers, and are also employed for commercial process by Universal Oil Products (UOP) [2]. Rao et al. [11] reported that pore-expanded mesoporous MCM-41 silica-supported chromium oxide showed moderate ethane conversion (23%) and high ethylene selectivity (~ 99 %) at 823 K. The reaction is

accompanied by the adsorption of ethane on C-O sites, and thus studies focusing on the working state of Cr are critical for catalyst optimization. For example, *in situ* UV and X-ray absorption near edge structure (XANES) measurements of CrO_x catalyst revealed mainly Cr³⁺ species are observed during the dehydrogenation reaction, although some Cr⁶⁺ species associated to the precursor is also observed; therefore, Cr³⁺ species is concluded to be the active sites [12 , 13]. Despite these promising results, dehydrogenation of ethane has some drawbacks: the reaction is thermodynamically limited and highly endothermic, and hence high reaction temperature and/or lower ethylene partial pressure is required to achieve high conversions.

1.1.2. Ethane dehydrogenation assisted with CO₂

Dehydrogenation of ethane has been carried out in the presence of CO₂, which is a hydrogen acceptor, as shown in Figure 1.3 [14]. This process has the potential to overcome the major technical problems associated with general dehydrogenation. Furthermore, CO₂ works as a mild oxidant to remove carbon (Boudart reaction: C+CO₂→ 2CO) on the catalyst surface providing enhancement of catalyst durability.

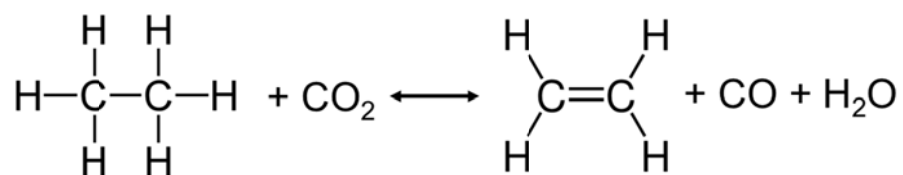


Figure 1.3. Illustration of CO₂-assisted ethane dehydrogenation

Several studies for CO₂-assisted dehydrogenation of ethane to ethylene has been reported on various catalysts, such as Cr₂O₃/ZrO₃ [15,16], Cr/H-ZSM-5 [17], Cr/TS-1

[18], Fe–Cr/ZrO₂ [19], Ga₂O₃/TiO₂ [20,21], Mo₂C/SiO₂ [22], and VO_x/Al₂O₃ [23]. Cheng et al. studied ethane dehydrogenation with CO₂ on a series of submicron ZSM-5-supported chromium oxide catalysts and found high activity (conversion: 65 %, ethylene yield: 49 %) without significant deactivation for 50 h [24]. Wang et al. studied the effects of Cr₂O₃ loading and various supports for ethane dehydrogenation with CO₂, and found the optimal Cr₂O₃ loading to be 8 wt. % and the activity of different supported catalysts follows the order: Cr₂O₃/SiO₂ > Cr₂O₃/ZrO₂ > Cr₂O₃/Al₂O₃ > Cr₂O₃/TiO₂, due to the influence of the support influence on the nature of chromium species and redox properties [15]. Indeed, Mimura et al. [25] used Fourier transform infrared spectroscopy and X-ray desorption fine structure measurements to propose redox reactions mechanism for the highly active Cr species for CO₂-assisted ethane hydrogenation, and found that ethane pretreatment reduced Cr⁶⁺ species to Cr³⁺ species, while CO₂ pretreatment reoxidized Cr species to the Cr⁶⁺ species. Therefore, the Cr redox cycle is important for a high dehydrogenation rate.

1.2. Hydrogen selective inorganic membrane

Membrane technology has been developed in the field of water treatment, air separation, nature gas sweetening and hydrogen recovery from ammonia pure gas with advantages of energy-efficiency, cost-effective and environmental compatibility. As emerging hydrogen economy, membranes with high permeability and selectivity could contribute to the development of new hydrogen separation technology, and have been researched extensively.

1.2.1. Silica-based membranes

Silica-based membranes are promising materials for high purity hydrogen production and separation with high chemical resistance and thermal stability. They are easily fabricated into an ultra-microporous thin layer that exhibits an excellent molecular sieving property [26].

Silica-based membranes have been prepared on porous supports by sol-gel methods and chemical vapor deposition (CVD) methods. Generally, sol-gel routes provide membrane with relatively high gas permeation, but the low selectivity because the pore structure of the material is based on particle packing [27]. The CVD methods generally provide denser structures resulting in lower permeance. However CVD-derived membranes have been reported higher selectivities and better stability and durability than sol-gel derived membranes. In addition, the process of the CVD method is easier than the sol-gel method.

Since the first reports of silica-based membranes by Okubo and Inoue and the group of Gavalas, tetraethylorthosilicate (TEOS)-derived silica-based membranes have been prepared by sol-gel methods and chemical vapor deposition (CVD) methods. Morooka et al. [28] reported that the modified membrane prepared by thermal decomposition of TEOS exhibited high H₂ permeance (10^{-8} mol m⁻² s⁻¹ Pa⁻¹) and low N₂ permeance (10^{-11} mol m⁻² s⁻¹ Pa⁻¹). Gu et al. [29] developed an ultrathin (20–30 nm) silica layer membrane which exhibited a high H₂/CO₂ ideal selectivity of 1500 with the H₂ permeance of about 5×10^{-8} mol m⁻² s⁻¹ Pa⁻¹ at 1 atm and 873 K. However, the instability of silica materials, especially in the presence of steam, limits their use in applications such as high temperature membrane reactors. Prolonged exposure of the silica to water vapor at elevated temperatures causes rapid densification that leads to a

decrease in the permeability of the membranes.

1.2.2. Hydrothermal stability of silica-based membranes

An approach to improve the hydrothermal stability of silica membranes is the formation of mixed silicates with other inorganic oxides such as alumina, titania, zirconia, cobalt, and nickel. Gu et al. [30] studied the silica–titania membranes and it was found that after 130 h exposure in 75 mol% H₂O at 923 K, the H₂ permeance was reduced by only 30 %, compared to a pure silica membrane which suffered a loss of 90 %. Fotou et al. [31] reported the alumina-doped silica membranes and improved hydrothermal stability because of the network modification which led to more resistant to densification in the presence of steam. Liu et al. [32] studied cobalt silica membranes for hydrothermal stability investigation on steam exposure to 25 mol% vapor at 823 K for 100 h. Gu et al. [33] reported that silica-alumina membrane enhanced the hydrothermal stability for periods in excess of 500 h at 873 K in 16% steam, allowing the H₂ permeance to remain above $10^{-7} \text{ mol m}^{-2} \text{ s}^{-1} \text{ Pa}^{-1}$.

1.2.3. Pore size controlled silica-based membranes

Furthermore, the small size of the openings and low hydrothermal stability of TEOS-derived pure silica membranes have limited the widespread applications of the membranes, and hence development of a controllable silica network size and improvement of hydrothermal stability are highly desirable [34,35]. Precursors in which the siloxanes are substituted with large pendant groups give rise to a connected pore structure and enhanced permeance in certain cases [36]. In addition, the organic moieties can improve hydrothermal stability because of their hydrophilicity [37,38,39].

Since Raman and Brinker first proposed a novel template method to control the pore size of microporous silica membranes by the sol-gel method [40], there have been a number of reports on the tuning of the network size of silica membranes by using various silica precursors via both the sol-gel and CVD methods. Kanezashi et al. prepared organic-inorganic hybrid silica membranes by the sol-gel method using bridged alkoxides such as bis(triethoxysilyl)methane (BTESM), bis(triethoxysilyl)ethane (BTESE) as silica precursors [41,42]. The pore size distribution determined by fitting to a normalized Knudsen-based permeance (NKP) suggested that the average pore size was in the following order: BTESE-derived silica (0.64 nm) > BTESM-derived silica (0.55 nm) > TEOS-derived silica (0.34 nm). It should be noted that the BTESM-derived membranes showed a high C₃H₆ permeance of $6.32 \times 10^{-7} \text{ mol m}^{-2} \text{ s}^{-1} \text{ Pa}^{-1}$ with a selectivity over C₃H₈ of 8.8 at 323 K indicating reasonably good pore size control. Lee et al. prepared silica membranes by the sol-gel method using disiloxanealkoxides such as tetraethoxydimethyldisiloxane (TEDMDS) and hexaethoxydisiloxane (HEDS) [43,44]. The order of estimated pore size was TEDMDS-derived silica (0.70 nm) > HEDS-derived silica (0.50 nm) > TEOS-derived silica (0.32 nm). The TEDMDS-derived membrane had high H₂ permeance of the order of $10^{-6} \text{ mol m}^{-2} \text{ s}^{-1} \text{ Pa}^{-1}$, but low H₂/N₂ selectivity below 20 indicating that permeance occurred through the pores. Kusakabe et al. prepared silica membranes by the sol-gel method using mixtures of TEOS and pendant-type alkoxides with carbon chain substitution such as octyltriethoxysilane, dodecyltriethoxysilane (DTEOS) and octadecyl-triethoxysilane. The TEOS-DTEOS-derived membrane showed a higher pore size distribution than the TEOS-derived membrane of around 0.3-0.4 nm, which was estimated based on single gas permeation tests [45]. Nomura et al. prepared a silica membrane by the counter

diffusion CVD method using tetramethoxysilane (TMOS) and O₂ [46]. The membrane had H₂ permeance of 1.5×10^{-7} mol m⁻² s⁻¹ Pa⁻¹ and H₂/N₂ selectivity over 1000, and was stable under the typical steam-reforming conditions of methane (76 kPa of steam at 773 K) for 21 h. Nomura et al. also prepared silica membranes using various pendant type alkoxides such as methyltrimethoxysilane (MTMOS), trimethylmethoxysilane (TMMOS), propyltrimethoxysilane (PrTMOS), phenyltrimethoxysilane (PhTMOS) [47]. The membranes prepared using methyl substituted precursors had H₂ permeance of 0.6- 1.4×10^{-7} mol m⁻² s⁻¹ Pa⁻¹ and H₂/N₂ selectivity over 200 with estimated pore sizes of about 0.3 nm. The membranes prepared using larger functional group (PrTMOS, PhTMOS) showed an order of magnitude higher H₂ permeance but smaller H₂/N₂ selectivity below 40 with maximum pore sizes around 0.5 nm. Thus, the authors concluded that the pore size of the silica membranes can be controlled by changing the type of silica precursors. Nakao and collaborators prepared silica membranes by the counter-diffusion CVD method using methoxysilanes with different numbers of substituted phenyl groups such as phenyltrimethoxysilane (PTMS), dimethoxydiphenylsilane (DMDPS) and triphenylmethoxysilane (TPMS) at 873 K [48,49]. The order of estimated pore size based on the normalized Knudsen-based permeance was TPMS-derived silica (0.486 nm) > DMDPS-derived silica (0.42 nm) > PTMS-derived silica. The DMDPS and TPMS-derived membranes had high H₂ permeances of the order of 10^{-6} mol m⁻² s⁻¹ Pa⁻¹ and high H₂/SF₆ selectivity of over 6800 and 12000, respectively. However, SF₆ is a large species and high selectivities are expected. Generally it was demonstrated that the silica network size was enlarged when the number of phenyl groups on the silicon source increased because larger spaces surrounded the aromatic moieties. However, in this study and many others cited above

the measurement of He, H₂ and Ne were not carried out, and this determination is crucial for determining the permeation mechanism [50].

1.3. Mechanisms of gas permeation through inorganic membranes

An investigation of the gas permeation mechanism is important to understand the nature and structure of the membranes. This is necessary for developing efficient gas separation membranes. Generally gas transport in inorganic membranes can occur through a number of possible mechanisms such as bulk Poiseuille flow for large pores, Knudsen fusion for intermediate size pores, size-restricted diffusion and surface diffusion for small pores, and bulk diffusion for very small pores or no pores [51,52,53]. The combination mechanism also can be considered as the conditions and the properties of the permeating molecules.

1.3.1. Hagen-Pouisselle mechanism

The Hagen-Pouisselle mechanism takes place when the pore diameter is larger (0.1-10 μm) than the mean free path of the molecules. Gas transport occurs by bulk fluid flow through the large pores (Figure 1.4 (a)). The Hagen-Pouisselle permeability, P_M [mol m⁻¹ s⁻¹ Pa⁻¹], is given by Eq. (1.1).

$$P_M = \frac{\rho \varepsilon^3}{2(1-\varepsilon)^2 \mu \tau a_v^2} \quad (1.1)$$

where ρ is the density of the gas molecules [kg m⁻³], ε the porosity of the membrane, μ the viscosity [kg m s⁻¹], τ the tortuosity of the membrane, a_v the pore area per membrane volume.

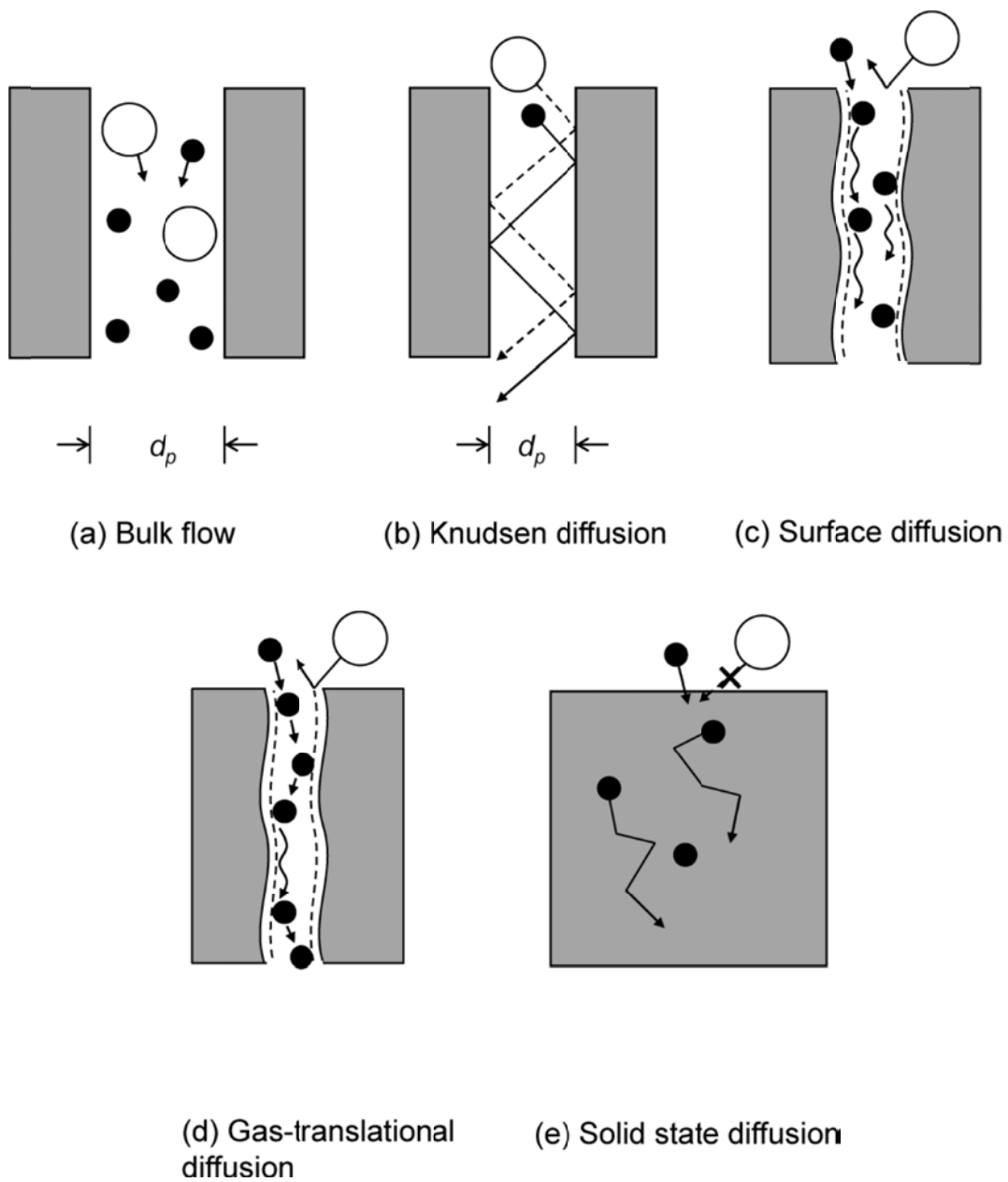


Figure 1.4. Various gas separation mechanisms through inorganic membranes [54]

1.3.2. Knudsen diffusion mechanism

The Knudsen diffusion occurs when pore diameter is smaller than the mean free path of the gas molecules, and transport is mainly by collisions between gas molecules and the pore wall rather than between the gas molecules themselves (Figure 1.4 (b)). The Knudsen permeance, \overline{P}_K [mol m⁻¹ s⁻² Pa⁻¹], is expressed by Eq. (1.2).

$$\overline{P}_K = \frac{\varepsilon d_p}{\tau L} \left(\frac{8RT}{9\mu M} \right)^{1/2} \quad (1.2)$$

where d_p is the pore diameter [nm], R the gas constant, T the temperature [K], L the thickness of the membrane [m], M the molecular weight of the diffusion gas [g mol⁻¹] and others are same as above.

1.3.3. Surface diffusion mechanism

The surface diffusion occurs when the interaction between the gas molecules and the inner surface becomes strong compared to their kinetic energy at low temperature range. Gas transport occurs by adsorbing the gas molecules onto the surface onto the pore entrance, diffusing through the membrane and desorbing at the pore exit (Figure 1.4 (c)). The permeance of surface diffusion model, \overline{P}_{SD} [mol m⁻¹ s⁻² Pa⁻¹], is written by Eq. (1.3).

$$\overline{P}_{SD} = \frac{\rho K_0 D_0}{L} \exp\left(\frac{-\Delta H_a - \Delta E_{SD}}{RT}\right) \quad (1.3)$$

where K_0 is the adsorption equilibrium constant, D_0 the diffusion coefficient [m² s⁻¹], ΔH_a the enthalpy of adsorption [J mol⁻¹], ΔE_{SD} the energy barrier for moving to the

other adsorption site [J mol⁻¹] and others are same as above.

1.3.4. Gas-translational mechanism

The gas-translational mechanism occurs in small pore sizes (order of 0.2-5 nm), and transport is a combination of the Knudsen diffusion model and the surface diffusion model (Figure 1.4 (d)). The permeance of gas-translation model, \overline{P}_{GT} [mol m⁻¹ s⁻² Pa⁻¹], can be expressed by Eq. (1.4).

$$\overline{P}_{GT} = \frac{\varepsilon d_P \rho_g}{\tau L} \left(\frac{8}{\pi MRT} \right)^{1/2} \exp \left(\frac{\Delta E_a}{RT} \right) \quad (1.4)$$

where ΔE_a is the kinetic energy to overcome the diffusion barrier [J mol⁻¹] and others are same as above.

1.3.5. Solid-state diffusion mechanism

The solid-state diffusion occurs in dense membrane materials when the gas interacts strongly with the membrane material. Gas transport occurs by the gas molecules jumps between solubility sites, and the behavior is similar to that in the surface diffusion except here is not through the pore (Figure 1.4 (e)). The permeance of solid-state diffusion through the silica-based material, \overline{P}_{SS} [mol m⁻¹ s⁻² Pa⁻¹], is expressed by Eq. (1.5).

$$\overline{P}_{SS} = \frac{1}{6L} \left(\frac{d^2}{h} \right) \left(\frac{h^2}{2\pi m_i kT} \right)^{3/2} \left(\frac{\sigma h^2}{8\pi^2 l kT} \right)^\alpha \times \frac{(N_s/N_A)}{(e^{hv^*/2kT} - e^{-hv^*/2kT})^2} e^{-\Delta E_a/RT} \quad (1.5)$$

where d is the jump distance, m_i the mass of the species i , h Planck's constant, k Boltzmann's constant, N_A Avogadro's number, α an exponent accounting for incomplete loss of rotation (0 for He and Ne, and 0.2 for H_2), σ the symmetry factor of the species (2 for H_2), I the moment of inertia, N_s the number of solubility sites per m^3 of membrane volume, ν^* the vibrational frequency of the species in the passageways between the sorption sites, ΔE_a the activation energy of diffusion.

1.4. Catalytic membrane reactor for ethane dehydrogenation

Interest in the development of catalytic membrane reactors has intensified due to its unique capability to combine two separate unit operations, reaction and separation processes, into a single operation. The main feature of the membrane is to selectively remove products, which will enhance reaction performance over its equilibrium conversions, and consequently allow for mild operation conditions.

There has been limited previous work on the dehydrogenation of ethane in membrane reactors. Jiang et al. [55] reported a novel coupling strategy to produce hydrogen and ethylene in a perovskite $BaCo_xFe_yZr_{1-x-y}O_{3-\delta}$ hollow-fiber membrane reactor and achieved high ethylene yield (55 %) and hydrogen production rate ($1.0 \text{ cm}^3 \text{ min}^{-1} \text{ cm}^{-2}$) at 1073 K. Avila et al. [56] studied ethane dehydrogenation on neutral mordenite membrane disk coupled to a Pt/ Al_2O_3 packed bed reactor and achieved an increase in ethane conversion and ethylene yield compared to their equilibrium values. Champagnie et al. [57] studied a high temperature catalytic membrane reactor, containing a Pt impregnated alumina ceramic membrane tube, for ethane dehydrogenation and found 6 times higher conversions than the equilibrium conversions. Gonina et al. [58] reported that a membrane consisting of a thin layer of Pd-23 wt% Ag

on porous Vucor glass attained 8 times higher ethane conversion than conventional fixed-bed reactor while using high sweep flow rates. Most of the studies have concluded that the enhancement of the performance is attributed to the exclusive and continuous permeation of hydrogen via the membrane.

Furthermore, it has been reported that catalytic membranes are used not only for H₂ separation but also for oxygen supply to the reaction. Wang et al. [59] applied a material (Ba_{0.5}Sr_{0.5}Co_{0.8}Fe_{0.2}O_{3-δ}) as oxygen permeable membrane as well as catalysts for oxidative dehydrogenation of ethane and it attained 90 % ethylene selectivity at 923 K. Coronas et al. [60] reported a ceramic membrane reactor with Li/MgO catalyst for the oxidative dehydrogenation of ethane and this gave higher yield up to 57 %. Akin et al. [61] studied selective oxidation of ethane in a dense tubular ceramic membrane prepared by oxygen ion conducting fluorite structured Bi_{1.5}Y_{0.3}Sm_{0.2}O₃ and it achieved 56 % ethylene yield and 80 % selectivity at 1148 K.

1.5. Outline of the dissertation

This thesis deals with the study of hydrogen selective silica-based membranes with application in a catalytic membrane reactor. The reaction studied is ethane dehydrogenation to ethylene over a Cr/ZSM-5 catalyst, a typical reaction for hydrogen generation where the net number of moles increases. In order to enhance the ethylene yield in the catalytic membrane reactor, high H₂ permeance and moderate H₂/C₂H₆ selectivity are required. First, silica-based membranes were developed to improve their permeability and hydrothermal stability by modifying their composition (Chapter 2) and using an organic functional group (Chapter 3). Specifically, the effect of alloying silica with zirconia (Chapter 2) and the effect of adding a vinyl substituent (Chapter 3)

were studied. The method of membrane synthesis was chemical vapor deposition (CVD). The morphology and structure of prepared membranes were determined, and the permeance mechanisms of small and large gases through the membranes were studied with experimental and simulated data. Second, the dehydrogenation reaction of ethane over the Cr/ZSM-5 catalyst was studied by examining the effect of various reaction conditions, including feed flow rates, pressures and temperatures. The reaction was carried out in a conventional packed-bed reactor (PBR) and in a membrane reactor (MR) fitted with silica membranes in described earlier (Chapters 2 and 3). Importantly, the reaction was studied at a range of pressures above atmospheric pressure. The performance of the membrane reactor was evaluated by model simulation with experimentally determined kinetics and H₂ permeances and H₂/C₂H₆ selectivities.

Chapter 2 described zirconia modified silica membranes prepared on porous alumina substrates by employing CVD with varying molar ratios Zr and Si. The precursors used were zirconium (IV) *tert*-butoxide (ZTB) and tetraethylorthosilicate (TEOS). This is the first report of the use of the ZTB precursor, and considerable enhancements in performance were obtained over previous reports. The permeation properties, hydrothermal stability, and permeation mechanism of the prepared membranes are discussed in detail.

Chapter 3 described silica membranes prepared on porous alumina substrates (60 nm) by employing the CVD of vinyltriethoxysilane (VTES), a precursor that has not been studied before, to investigate the effect of the vinyl group on the silica structure and stability of the membrane. Scanning electron microscopy (SEM) and in situ Fourier transform infrared (FTIR) measurements were used to characterize the morphology and structure of the membrane after CVD. This is the first time an in situ spectroscopic

method has been used to study functional groups in silica membranes. The permeation properties, including those of He, H₂, and Ne, hydrothermal stability, and permeation mechanism of the prepared membranes are discussed in detail.

Chapter 4 described the dehydrogenation of ethane conducted over a 5 wt% Cr/ZSM-5 catalyst coupled to a H₂ selective silica membrane. Various reaction conditions were varied such as feed flow rates (20-100 cm³ min⁻¹), total pressures (0.1-0.5 MPa) and temperatures (723-823 K) and were applied to a packed bed reactor (PBR) and a membrane reactor (MR). A general parameter, the operability level coefficient (OLC), the ratio between the actual permeation rate and the actual formation rate of a H₂ in a membrane reactor, was used to correlate the performance of the membrane reactor. High pressure studies of membrane reactors are rare, and this is the first time that high pressure was employed to study the ethane dehydrogenation reaction.

Chapter 5 describes general conclusions of the thesis, including the findings of the modified silica-based membranes and ethane dehydrogenation in membrane reactor with the prepared hydrogen selective silica-based membranes. The use of the silica-zirconia and vinyl-substituted membranes allowed a broad parameter space to be explored for the obtention of general results. Important conclusions were that high pressure is beneficial for membrane reactors even for reactions such as dehydrogenation reactions where the net number of moles increase, and that a product selectivity of 100 is sufficient to get good enhancements. It also presents suggestions for future work, which would lead to the improvement of the performance of membrane reactors for ethane dehydrogenation.

Reference

- [1] L. Bewley, His Wpc 2012: Shale reshapes ethylene markets, *Chemical Week*. 174 (2012) 15.
- [2] J.J.H.B. Sattler, J. Ruiz-Martinez, E. Santillan-Jimenez, B.M. Weckhuysen, Catalytic dehydrogenation of light alkanes on metals and metal oxides, *Chem. Rev.* 114 (2014) 10613-10653.
- [3] A. Virnovskaia, E. Rytter, U. Olsbye, Kinetic and isotopic study of ethane dehydrogenation over a semicommercial Pt₂Sn/Mg(Al)O catalyst, *Ind. Eng. Chem. Res.* 47 (2008) 7167-7177.
- [4] V. Galvita, G. Siddiqi, P. Sun, A.T. Bell, Ethane dehydrogenation on Pt/Mg(Al)O and PtSn/Mg(Al)O catalysts, *J. Catal.* 271 (2010) 209-219.
- [5] P. Sun, G. Siddiqi, M. Chi, A.T. Bell, Synthesis and characterization of a new catalyst Pt/Mg(Ga)(Al)O for alkane dehydrogenation, *J. Catal.* 274 (2010) 192-199.
- [6] G. Siddiqi, P. Sun, V. Galvita, A.T. Bell, Catalyst performance of novel Pt/Mg(Ga)(Al)O catalysts for alkane dehydrogenation, *J. Catal.* 274 (2010) 200-206.
- [7] P. Sun, G. Siddiqi, W.C. Vining, M. Chi, A.T. Bell, Novel Pt/Mg(In)(Al)O catalysts for ethane and propane dehydrogenation, *J. Catal.* 282 (2011) 165-174.
- [8] A.W. Hauser, J. Gomes, M. Bajdich, M. Head-Gordon, A.T. Bell, Subnanometer-sized Pt/Sn alloy cluster catalysts for the dehydrogenation of linear alkanes, *Phys. Chem. Chem. Phys.* 15 (2013) 20727-20734.
- [9] J. Wu, Z. Peng, A.T. Bell, Effects of composition and metal particle size on ethane dehydrogenation over Pt_xSn_{100-x}/Mg(Al)O ($70 \leq x \leq 100$), *J. Catal.* 311 (2014) 161-168.
- [10] J.M. Essen, J. Haubrich, C. Becker, K. Wandelt, Adsorption of ethene on Pt(111) and ordered Pt_xSn/Pt(111) surface alloys: A comparative HREELS and DFT investigation, *Surf. Sci.* 601 (2007) 3472-3480.
- [11] T.V.M. Rao, E.M. Zahidi, A. Sayari, Ethane dehydrogenation over pore-expanded mesoporous silica-supported chromium oxide: 2. Catalytic properties and nature of active sites, *J. Mol. Catal. A: Chem.* 301 (2009) 159-165.

-
- [12] M.S. Kumar, N. Hammer, M. Ronning, A. Holmen, D. Chen, J.C. Walmsley, G. Oye, The nature of active chromium species in Cr-catalysts for dehydrogenation of propane: New insights by a comprehensive spectroscopic study, *J. Catal.* 261 (2009) 116-128.
- [13] P. Michorczyk, J. Ogonowski, K. Zenczak, Activity of chromium oxide deposited on different silica supports in the dehydrogenation of propane with CO₂ - A comparative study, *J. Mol. Catal. A: Chem.* 349 (2011) 1-12.
- [14] F. Cavani, F. Trifiro, The oxidative dehydrogenation of ethane and propane as an alternative way for the production of light olefins, *Catal. Today* 24 (1995) 307-313.
- [15] S. Wang, K. Murata, T. Hayakawa, S. Hamakawa, K. Suzuki, Dehydrogenation of ethane with carbon dioxide over supported chromium oxide catalysts, *Appl. Catal. A: Gen.* 196 (2000) 1-8.
- [16] M. Ji, D.Y. Hong, J.S. Chang, V.P. Vislovskiy, J.S. Yoo, S.E. Park, Oxidative dehydrogenation of ethane with carbon dioxide over supported chromium oxide catalysts, *Carbon Dioxide Utilization for Global Sustainability* 153 (2004) 339-342.
- [17] N. Mimura, I. Takahara, M. Inaba, M. Okamoto, K. Murata, High-performance Cr/H-ZSM-5 catalysts for oxidative dehydrogenation of ethane to ethylene with CO₂ as an oxidant, *Catal. Commun.* 3 (2002) 257-262.
- [18] X. Zhao, X. Wang, Oxidative dehydrogenation of ethane to ethylene by carbon dioxide over Cr/TS-1 catalysts, *Catal. Commun.* 7 (2006) 633-638.
- [19] S. Deng, S. Li, H. Li, Y. Zhang, Oxidative dehydrogenation of ethane to ethylene with CO₂ over Fe-Cr/ZrO₂ catalysts, *Ind. Eng. Chem. Res.* 48 (2009) 7561-7566.
- [20] K. Nakagawa, C. Kajita, K. Okumura, N. Ikenaga, M. Nishitani-Gamo, T. Ando, T. Kobayashi, T. Suzuki, Role of carbon dioxide in the dehydrogenation of ethane over gallium-loaded catalysts, *J. Catal.* 203 (2001) 87-93.
- [21] K. Nakagawa, M. Okamura, N. Ikenaga, T. Suzuki, K. T. Kobayashi, Dehydrogenation of ethane over gallium oxide in the presence of carbon dioxide, *Chem. Commun.* (1998) 1025-1026.
- [22] F. Solymosi, R. Nemeth, The oxidative dehydrogenation of ethane with CO₂ over Mo₂C/SiO₂ catalyst, *Catal. Lett.* 62 (1999) 197-200.

-
- [23] T. Blasco, A. Galli, J.M.L. Nieto, F. Trifiro, Oxidative dehydrogenation of ethane and n-butane on VO_x/Al₂O₃ catalysts, *J. Catal.* 169 (1997) 203-211.
- [24] Y. Cheng, F. Zhang, Y. Zhang, C. Miao, W. Hua, Y. Yue, Z. Gao, Oxidative dehydrogenation of ethane with CO₂ over Cr supported on submicron ZSM-5 zeolite, *Chin. J. Catal.* 36 (2015) 1242-1248.
- [25] N. Mimura, M. Okamoto, H. Yamashita, S.T. Oyama, K. Murata, Oxidative dehydrogenation of ethane over Cr/ZSM-5 catalysts using CO₂ as an oxidant, *J. Phys. Chem. B* 110 (2006) 21764-21770.
- [26] P. Li, Z. Wang, Z. Qiao, Y. Liu, X. Cao, W. Li, J. Wang, S. Wang, Recent developments in membranes for efficient hydrogen purification, *J. Membr. Sci.* 495 (2015) 130-168.
- [27] S.J. Khatib, S.T. Oyama, Silica membranes for hydrogen separation prepared by chemical vapor deposition (CVD), *Sep. Purif. Technol.* 111 (2013) 20-42.
- [28] S. Morooka, S. Yan, K. Kusakabe, Y. Akiyama, Formation of hydrogen-permselective SiO₂ membrane in macropores of α -alumina support tube by thermal decomposition of TEOS, *J. Membr. Sci.* 101 (1995) 89-98.
- [29] Y. Gu, S.T. Oyama, Ultrathin, hydrogen-selective silica membranes deposited on alumina-graded structures prepared from size-controlled boehmite sols, *J. Membr. Sci.* 306 (2007) 216-227.
- [30] Y. Gu, S.T. Oyama, Permeation properties and hydrothermal stability of silica-titanic membranes supported on porous alumina substrates, *J. Membr. Sci.* 345 (2009) 267-275.
- [31] G.P. Fotou, Y.S. Lin, S.E. Pratsinis, Hydrothermal stability of pure and modified microporous silica membranes, *J. Mater. Sci.* 30 (1995) 2803-2808.
- [32] L. Liu, D.K. Wang, D.L. Martens, S. Smart, J.C.D. da Costa, Binary gas mixture and hydrothermal stability investigation of cobalt silica membranes, *J. Membr. Sci.* 493 (2015) 470-477.
- [33] Y. Gu, P. Hacırlıoğlu, S.T. Oyama, Hydrothermally stable silica-alumina composite membranes for hydrogen separation, *J. Membr. Sci.* 310 (2008) 28-37.
- [34] H.M. van Veen, Y.C. van Delft, C.W.R. Engelen, P.P.A.C. Pex, Dewatering of organics by pervaporation with silica membranes, *Sep. Purif. Technol.* 22-23 (2001) 361-366.

-
- [35] M. Asaeda, J. Yang, Y. Sakou, Porous silica-zirconia (50%) membranes for pervaporation of iso-propyl alcohol (IPA)/water mixtures, *J. Chem. Eng. Jpn.* 35 (2002) 365-371.
- [36] I. Agirre, P.L. Arias, H.L. Castricum, M. Creatore, J.E. ten Elshof, G.G. Paradis, P.H.T. Ngamou, H.M. van Veen, J.F. Vente, Hybrid organosilica membranes and processes: Status and outlook, *Sep. Purif. Technol.* 121 (2014) 2-12.
- [37] R.M. de Vos, W.F. Maier, H. Verweij, Hydrophobic silica membranes for gas separation, *J. Membr. Sci.* 158 (1999) 277-288.
- [38] H.L. Castricum, A. Sah, R. Kreiter, D.H.A. Blank, J.F. Vente, J.E. ten Elshof, Hybrid ceramic nanosieves: stabilizing nanopores with organic links, *Chem. Commun.* (2008) 1103-1105.
- [39] J. Campaniello, C.W.R. Engelen, W.G. Haije, P.P.A.C. Pex, J.F. Vente, Long-term pervaporation performance of microporous methylated silica membranes, *Chem. Commun.* (2004) 834-835.
- [40] N.K. Raman, C.J. Brinker, Organic "template" approach to molecular sieving silica membranes, *J. Membr. Sci.* 105 (1995) 273-279.
- [41] M. Kanezashi, K. Yada, T. Yoshioka, T. Tsuru, Organic-inorganic hybrid silica membranes with controlled silica network size: Preparation and gas permeation characteristics, *J. Membr. Sci.* 348 (2010) 310-318.
- [42] M. Kanezashi, M. Kawano, T. Yoshioka, T. Tsuru, Organic-inorganic hybrid silica membranes with controlled silica network size for propylene/propane separation, *Ind. Eng. Chem. Res.* 51 (2012) 944-953.
- [43] H.R. Lee, M. Kanezashi, Y. Shimomura, T. Yoshioka, T. Tsuru, Evaluation and fabrication of pore-size-tuned silica membranes with tetraethoxydimethyl-disiloxane for gas separation, *AIChE J.* 57 (2011) 2755-2765.
- [44] H.R. Lee, T. Shibata, M. Kanezashi, T. Mizumo, J. Ohshita, T. Tsuru, Pore-size-controlled silica membranes with disiloxane alkoxides for gas separation, *J. Membr. Sci.* 383 (2011) 152-158.
- [45] K. Kusakabe, S. Sakamoto, T. Saie, S. Morooka, Pore structure of silica membranes formed by a sol-gel technique using tetraethoxysilane and alkyltriethoxysilanes, *Sep. Purif. Technol.* 16 (1999) 139-146.

-
- [46] M. Nomura, K. Ono, S. Gopalakrishnan, T. Sugawara, S.-I. Nakao, Preparation of a stable silica membrane by a counter diffusion chemical vapor deposition method, *J. Membr. Sci.* 251 (2005) 151-158.
- [47] M. Nomura, T. Nagayo, K. Monma, Pore size control of a molecular sieve silica membrane prepared by a counter diffusion CVD method, *J. Chem. Eng. Jpn.* 40 (2007) 1235-1241.
- [48] Y. Ohta, K. Akamatsu, T. Sugawara, A. Nakao, A. Miyoshi, S. Nakao, Development of pore size-controlled silica membranes for gas separation by chemical vapor deposition, *J. Membr. Sci.* 315 (2008) 93-99.
- [49] X.-L. Zhang, H. Yamada, T. Saito, T. Kai, K. Murakami, M. Nakashima, J. Ohshita, K. Akamatsu, S. Nakao, Development of hydrogen-selective triphenylmethoxysilane-derived silica membranes with tailored pore size by chemical vapor deposition, *J. Membr. Sci.* 499 (2016) 28-35.
- [50] S.-J. Ahn, A. Takagaki, T. Sugawara, R. Kikuchi, S.T. Oyama, Permeation properties of silica-zirconia composite membranes supported on porous alumina substrates, *J. Membr. Sci.* 526 (2017) 409-416.
- [51] J. Dong, Y.S. Lin, M. Kanezashi, Z. Tang, Microporous inorganic membranes for high temperature hydrogen purification, *J. Appl. Phys.*, 104 (2008) 121301.
- [52] G.Q. Lu, J.C. Diniz da Costa, M. Duke, S. Giessler, R. Socolow, R.H. Williams, T. Kreutz, Inorganic membranes for hydrogen production and purification: a critical review and perspective, *J. Colloid. Interface Sci.* 314 (2007) 589-603.
- [53] T. Tsuru, Nano/subnano-tuning of porous ceramic membranes for molecular separation, *J. Sol-gel Sci. Technol.* 46 (2008) 349-361.
- [54] S.T. Oyama, M. Yamada, T. Sugawara, A. Takagaki, R. Kikuchi, Review on mechanisms of gas permeation through inorganic membranes, *J. Jpn. Petrol. Inst.* 54 (2001) 298-309.
- [55] H.Q. Jiang, Z.W. Cao, S. Schirrmeister, T. Schiestel, J. Caro, A coupling strategy to produce hydrogen and ethylene in a membrane reactor, *Angew. Chem.* 49 (2010) 5656-5660.
- [56] A.M. Avila, Z. Yu, S. Fazli, J.A. Sawada, S.M. Kuznicki, Hydrogen-selective natural mordenite in a membrane reactor for ethane dehydrogenation, *Microporous Mesoporous Mater.* 190 (2014) 301-308.

-
- [57] A.M. Champagnie, T.T. Tsotsis, R.G. Minet, I.A. Webster, A high-temperature catalytic membrane reactor for ethane dehydrogenation, *Chem. Eng. Sci.* 45 (1990) 2423-2429.
- [58] E. Gobina, R. Hughes, Ethane dehydrogenation using a high-temperature catalytic membrane reactor, *J. Membr. Sci.* 90 (1994) 11-19.
- [59] H. Wang, Y. Cong, W. Yang, High selectivity of oxidative dehydrogenation of ethane to ethylene in an oxygen permeable membrane reactor, *Chem. Commun.* (2002) 1468-1469.
- [60] J. Coronas, M. Menendez, J. Santamaria, Use of a ceramic membrane reactor for the oxidative dehydrogenation of ethane to ethylene and higher hydrocarbons, *Ind. Eng. Chem. Res.* 34 (1995) 4229-4234.
- [61] F.T. Akin, Y.S. Lin, Selective oxidation of ethane to ethylene in a dense tubular membrane reactor, *J. Membr. Sci.* 209 (2002) 457-467.

Chapter 2

Permeation Properties of Silica-Zirconia Composite Membranes Supported on Porous Alumina Substrates

This chapter is a modified version of a paper published in the Journal of Membrane Science: S.J. Ahn, A. Takagaki, T. Sugawara, R. Kikuchi, S.T. Oyama, Permeation properties of silica-zirconia composite membranes supported on porous alumina substrates, *J. Membr. Sci.* 526 (2017) 409-416.

2.1. Introduction

Hydrogen is an important feedstock which is used extensively in chemicals production and refinery operations, and has potential in fuel cell applications. It is considered a promising fuel for the future as it offers the possibility of reducing environment pollution [1,2]. Membranes with high permeability and selectivity could contribute to the development of new hydrogen separation technology, and have been researched extensively. Hydrogen selective membranes include organic polymers, microporous ceramics, dense metals, and silica glasses [3,4,5]. The silica-based materials are promising for high purity hydrogen production and separation with high chemical resistance and thermal stability, as well as moderate cost [6]. However, the instability of silica materials, especially in the presence of steam, limits their use in applications such as high temperature membrane reactors. Prolonged exposure of the

silica to water vapor at elevated temperatures causes rapid densification that leads to a decrease in the permeability of the membranes [7,8]. An approach to improve the hydrothermal stability of silica membranes is the formation of mixed silicates with other inorganic oxides such as alumina, titania, zirconia, cobalt, and nickel. These combination materials have been prepared by sol-gel techniques [9,10,11,12] or chemical vapor deposition (CVD) [13,14].

Since the first reports of silica-based membranes by Okubo and Inoue [15] and the group of Gavalas [16], many silica-alloys have been studied, among them silica-zirconia membranes. Table 2.1 summarizes the work done with zirconia. Ohya et al. [17,18] prepared a 60 mol% of $ZrO_2-SiO_2-Y_2O_3$ composite membrane, which included 1.8 mol% of Y_2O_3 , by a sol-gel method for use in thermochemical water decomposition processes. Tsuru et al. [19,20] prepared a 10% ZrO_2-SiO_2 membrane by a sol-gel method and studied its properties for nanofiltration in non-aqueous solutions of ethanol and methanol. Gu et al. [21] reported a pure ZrO_2 membrane prepared by a sol-gel method that was more hydrothermally stable than the pure $\gamma-Al_2O_3$ and silica membranes with only 5% reduction of H_2 permeance with exposure to 3 mol% water vapor at 423 K for 70 h. Urtiaga et al. [22] and Araki et al. [23] prepared a 50% ZrO_2-SiO_2 membrane by a sol-gel method and a CVD method, and studied their properties for pervaporation of water-propanol mixtures. Choi et al. [24] reported a 50% ZrO_2-SiO_2 membrane prepared by CVD method at 923 K for application in the HI decomposition reaction with H_2 permeance of $7.3 \times 10^{-8} \text{ mol m}^{-2} \text{ s}^{-1} \text{ Pa}^{-1}$ and H_2/N_2 selectivity of 25 that was stable in water vapor for 105 h. Li and Qi [25] reported a pure ZrO_2 membrane prepared by a sol-gel method for use in steam-reforming of hydrocarbons and the water-gas shift reaction with H_2 permeance of $2.4 \times 10^{-8} \text{ mol m}^{-2} \text{ s}^{-1} \text{ Pa}^{-1}$ and H_2/CO_2

selectivity of 28 that was stable in 100 kPa of steam for 1250 h. In spite of the efforts to improve the permeance properties and hydrothermal stability of silica-zirconia composite membranes, they still remain poorly understood and improvements are needed to enhance their permeance properties. Especially there are few publications about silica-zirconia composite membranes prepared by the CVD method.

This chapter describes zirconia modified silica membranes prepared on porous alumina substrates by chemical vapor deposition (CVD) with varying molar ratios of Zr and Si. Precursors used in the synthesis were zirconium (IV) *tert*-butoxide (ZTB) and tetraethylorthosilicate (TEOS) delivered by vaporization from bubblers. The objectives were to improve the H₂ permeability and stability of the silica-based membranes and to apply them in a catalytic membrane reactor. The permeation properties, hydrothermal stability, and permeation mechanism of the prepared membranes are discussed in detail. The present study can be distinguished from previous work for the obtention of high permeance and selectivity (Table 2.1), as well as for providing an understanding of the mechanism of permeation.

Table 2.1. Past work on silica-zirconia membranes

| Composition mol% ZrO ₂ Comment | ZrO ₂ Precursor | Thickness / μm | Separation | T / K | Permeance / mol m ⁻² s ⁻¹ Pa ⁻¹ | Selectivity / - | Year Ref. |
|--|-------------------------------|-------------------|--|-----------------|---|--------------------|--------------|
| 60% ZrO ₂ /ceramic | Zr-n- propoxide | 2.6-3.3 | HBr/H ₂ O | 423 - 773 | HBr 1.5×10^{-8} / mol m ⁻² s ⁻¹ | 36 | 1994 [17] |
| 10% ZrO ₂ /α-Al ₂ O ₃ Aqueous | Zr-tetra- butoxide | NR | Molecules with different weight | 298 | H ₂ O 6.2×10^{-10} | NR | 1998 [19] |
| 100% ZrO ₂ /α-Al ₂ O ₃ 3 kPa Steam 70 h | Zr-n- propoxide | NR | H ₂ /CO ₂ | 423 | H ₂ 4.9×10^{-6} | 6 | 2003 [21] |
| 50% ZrO ₂ /α-Al ₂ O ₃ pervaporation | Zr-n- butoxide | 0.5 | Isopropanol (or acetone) /water | 323 | H ₂ O 0.093 / mol m ⁻² s ⁻¹ | NR | 2006 [22] |
| 50% ZrO ₂ /α-Al ₂ O ₃ pervaporation | Zr-n- butoxide | 0.9 | Isopropanol /water | 348 | H ₂ O 0.021 / mol m ⁻² s ⁻¹ | 62 | 2011 [23] |
| 50% ZrO ₂ /α-Al ₂ O ₃ Steam 105 h | Zr-n- propoxide | 0.75-1 | H ₂ /N ₂ | 873 | H ₂ 7.3×10^{-8} | 25 | 2013 [24] |
| 100% ZrO ₂ /α-Al ₂ O ₃ 100 kPa Steam 1250 h | Zr-n- propoxide | NR | H ₂ /CO ₂ | 473 | H ₂ 2.4×10^{-8} | 28 | 2015 [25] |
| 10% ZrO ₂ /α-Al ₂ O ₃ 16 kPa Steam 48 h | Zr-tert- butoxide | 0.03 | H ₂ /N ₂ | 923 | H ₂ 1.5×10^{-7} | 5700 | This work |

NR: Not reported

2.2. Experimental

2.2.1. Preparation of γ -alumina intermediate layer

A γ -alumina intermediate layer was prepared on a macroporous α -alumina support by a dipping-calcining method. The preparation involved several steps. First, a commercial α -alumina tube (Noritake Corporation, O.D.= 6 mm, I.D.= 4 mm) with nominal pore size of 60 nm was cut to a length of 30 mm with a diamond cutter and connected to non-porous alumina tubes using glass joints (Nippon Electric Glass Co., Ltd) by heating at 1273 K for 10 min. After cooling to room temperature, the outside of the support was wrapped with Teflon tape to treat only the inside of the support. Second, the support was dipped into a dipping solution containing boehmite sols for 10 s and dried in air for 6 h. Third, the dried support was heated to 923 K in air at a rate of 1.5 K min^{-1} and calcined at 923 K for 3 h. The dipping-calcining process was repeated two times using different dipping solutions with 80 nm and 60 nm particle size of boehmite sols to produce a uniform and defect free membrane surface.

The dipping solutions were synthesized by mixing the boehmite sols with a polyvinyl alcohol (PVA, Polysciences, Inc. M.W. \sim 78,000) solution and diluting with distilled water to obtain a 0.15 M concentration of the sol and a 0.35 wt. % concentration of the PVA. This procedure was similar to that described previously by the group of Oyama [26]. The boehmite sols were synthesized using a sequence of hydrolysis of aluminum alkoxides and acid peptization, with first 0.13 mol of aluminum isopropoxide (Aldrich, 98%) added to 200 ml of distilled water at 371 K, and stirred with 550 rpm for 24 h. Then, a quantity of nitric acid (Wako, 60%) was slowly added to the mixture to give a molar ratio of H^+ /alkoxide of 0.025 or 0.07 and was then stirred for 24 h.

2.2.2. Preparation of silica-zirconia composite membranes

The silica-zirconia composite membranes were prepared on the γ -alumina intermediate layer by the CVD method. A schematic of the CVD apparatus is shown in Figure 2.1 (a). The apparatus shows a back-pressure regulator, but that was used only for permeance measurements described in the next section, not for the syntheses of the steam stability measurements, which were conducted at 101 kPa (atmospheric pressure). The system also incorporates a bubbler, which is a common means of vaporizing liquids [27]. The CVD procedure was carried out in a concentric tubular apparatus with an outer stainless steel tube using tetraethylorthosilicate (TEOS, Aldrich, 98 %) as silica precursor, zirconium (IV) *tert*-butoxide (ZTB, Aldrich, 99.999 %) as zirconia precursor. Argon was used as carrier, dilution and balance gas. After heating the apparatus to 923 K at a rate of 1.5 K min⁻¹, 13 cm³ (NTP) min⁻¹ (9.7 μ mol s⁻¹) of balance gas was introduced to the outside of the support and 13 cm³ (NTP) min⁻¹ (9.7 μ mol s⁻¹) of premixed gas, which included 3.5 cm³ (NTP) min⁻¹ (2.6 μ mol s⁻¹) of carrier gas and 6 cm³ (NTP) min⁻¹ (4.5 μ mol s⁻¹) of dilution gas, was introduced to the inside of the support with the ZTB/TEOS molar ratio varied from 0 to 0.15. The CVD was conducted at 923 K with the TEOS bubbler temperature at 298 K and the ZTB bubbler temperature at 306-319 K. The CVD parameters are summarized in Table 2.2. The CVD was interrupted periodically to check the H₂ permeance and H₂/N₂ selectivity of the membrane, and was conducted until an adequate H₂ permeance and H₂/N₂ selectivity were obtained.

Table 2.2. CVD conditions for the preparation of membranes

| CVD parameter \ Membrane | Si | 025Si-Zr | 05Si-Zr | 10Si-Zr | 15Si-Zr |
|---|----|----------|---------|---------|---------|
| ZTB bubbler temperature (K) | - | 229 | 306 | 314 | 319 |
| ZTB concentration x 10 ³ (mol % in inlet flow) | - | 1.70 | 3.25 | 6.45 | 9.66 |
| ZTB/TEOS (molar) | 0 | 0.025 | 0.05 | 0.10 | 0.15 |

ZTB = Zirconium (IV) *tert*-butoxide, TEOS = Tetraethylorthosilicate

CVD reactor at 101 kPa, 923 K

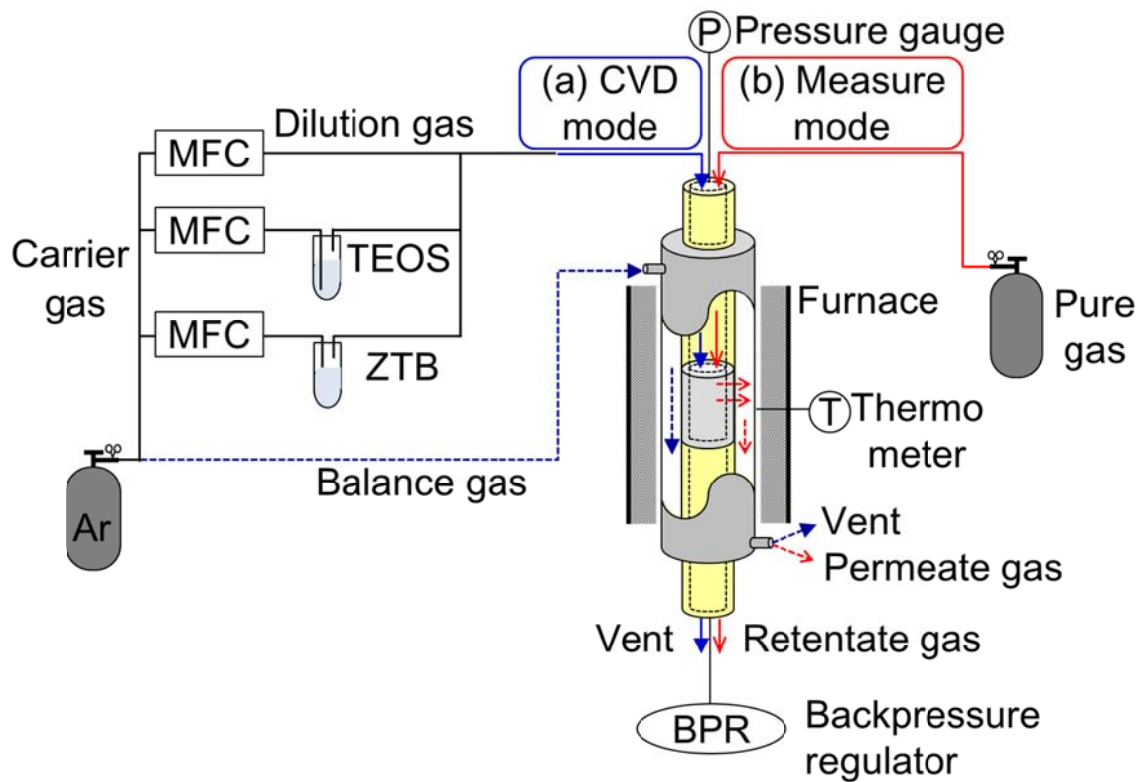


Figure 2.1. Experimental setup for chemical vapor deposition (CVD) process and permeability test (Conditions: CVD and hydrothermal stability test at 923 K, 101 kPa, permeance test at 923 K, $\Delta P = 0.24$ MPa)

2.2.3. Characterization

The particle size of the boehmite sols in the dipping solutions were measured by a dynamic light scattering analyzer (Horiba Model LB-550). The analyzer was calibrated using standard polystyrene latex microsphere solutions with mean diameter of 50 nm and 100 nm (Polysciences, Inc.).

The morphology of the membranes was obtained using a field emission scanning electron microscope (FE-SEM, Hitachi S-900). The samples were lightly coated with Pt-Pd by ion sputtering (E-1030, Hitachi) with a current of 15 mA for 15 s.

For permeance calculations gas flow rates over 0.2 ml min^{-1} were measured by a flow meter (Agilent Technologies, AD1000), and concentrations for gas flow rates below 0.2 ml min^{-1} were measured using a micro gas chromatograph (micro GC, Agilent Technologies, 490 micro GC, A molecular sieve 5A column was used for N_2 and a Porapak Q column was employed for CO_2 and CH_4).

2.2.4. Permeance and hydrothermal stability measurements

The gas permeance measurements were carried out using gases such as He, Ne, H_2 , CO_2 , N_2 and CH_4 at 923 K. A pure gas was introduced to the inside of the support at a pressure of around 0.3 MPa, and the inside of the support was pressurized by closing a backpressure regulator (BPR), and then the flow rate of permeate gas was measured on the outside (Figure 2.1 (b)). The permeance of gases was calculated by using Eq. (2.1):

$$\bar{P}_i = \frac{F_i}{A\Delta P_i} \quad (2.1)$$

where \bar{P}_i is the permeance of species i [$\text{mol m}^{-2} \text{ s}^{-1} \text{ Pa}^{-1}$], F_i is the molar flow rate of the gas i [mol s^{-1}], A is the surface area of the membrane [m^2] and ΔP_i is the partial pressure difference of gas i between the inner and the outer side of the membrane tube

[Pa].

The ideal selectivity was defined as the ratio of the single-gas permeances as given by Eq. (2.2).

$$\alpha_{ij}^* = \frac{\bar{P}_i}{\bar{P}_j} \quad (2.2)$$

where α_{ij}^* is the ideal selectivity of a species i over j [-], \bar{P}_i and \bar{P}_j are the permeances of species i and j , respectively [$\text{mol m}^{-2} \text{s}^{-1} \text{Pa}^{-1}$].

A hydrothermal stability test was conducted under an Ar flow containing 16 mol% of water vapor at 923 K for 48 h. For this condition, $10 \text{ cm}^3 \text{ (NTP) min}^{-1}$ ($7.4 \text{ } \mu\text{mol s}^{-1}$) of Ar flow was passed through a heated bubbler containing distilled water at 329 K, and the gas was introduced to the inside of the support while flowing $10 \text{ cm}^3 \text{ (NTP) min}^{-1}$ ($7.4 \text{ } \mu\text{mol s}^{-1}$) of Ar on the outside of the support. The H_2 permeance was measured periodically during the test.

2.3. Results and discussion

2.3.1. Preparation of silica-zirconia composite membranes

In order to investigate the effect of zirconia content on the permeation properties of the silica-zirconia composite membranes, the permeances of H_2 and N_2 were measured with different molar ratios of ZTB/TEOS (0-0.15) by changing ZTB bubbler temperature (Table 2.2), and the ideal selectivity of H_2/N_2 was calculated from the individual H_2 and N_2 permeances. Figure 2.2 (a-e) show the changes of H_2 and N_2 permeance and H_2/N_2 ideal selectivity as a function of the CVD time through the pure silica membrane and silica-zirconia composite membranes, which were prepared with molar ratios of ZTB/TEOS of 0.025, 0.05, 0.1 and 0.15 at 923 K. Before the CVD, the prepared γ -alumina intermediate layer substrate had high H_2 and N_2 permeances of the

order of 10^{-6} mol m⁻² s⁻¹ Pa⁻¹ but low H₂/N₂ ideal selectivity of 3.4, which was close to the value of 3.7 predicted by Knudsen diffusion.

In order to investigate the effect of zirconia content on the permeation properties of the silica-zirconia composite membranes, the permeances of H₂ and N₂ were measured with different molar ratios of ZTB/TEOS (0-0.15) by changing ZTB bubbler temperature (Table 2.2), and the ideal selectivity of H₂/N₂ was calculated from the individual H₂ and N₂ permeances. Figure 2.2 (a-e) show the changes of H₂ and N₂ permeance and H₂/N₂ ideal selectivity as a function of the CVD time through the pure silica membrane and silica-zirconia composite membranes, which were prepared with molar ratios of ZTB/TEOS of 0.025, 0.05, 0.1 and 0.15 at 923 K. Before the CVD, the prepared γ -alumina intermediate layer substrate had high H₂ and N₂ permeances of the order of 10^{-6} mol m⁻² s⁻¹ Pa⁻¹ but low H₂/N₂ ideal selectivity of 3.4, which was close to the value of 3.7 predicted by Knudsen diffusion.

The CVD was carried out for different amounts of time that depended on the permeation properties of the membranes. The properties were measured periodically by interrupting the CVD process, and measuring the H₂ and N₂ permeance and obtaining the corresponding H₂/N₂ selectivity. The CVD was completed at a level where the H₂ permeance was above 10^{-7} mol m⁻² s⁻¹ Pa⁻¹, and where the H₂/N₂ selectivity was high. The progress of the synthesis for various Zr/Si ratios is shown in Figure 2.3. The figure shows that for the silica membrane the CVD required only 30 min, while for the low Zr content membranes the time required rose to 45 min, and for the high Zr content membranes the time needed increased to 60 min. This indicates that the reactivity of the Zr precursor was smaller than that of the TEOS, or that the presence of Zr inhibited the growth of silica chains.

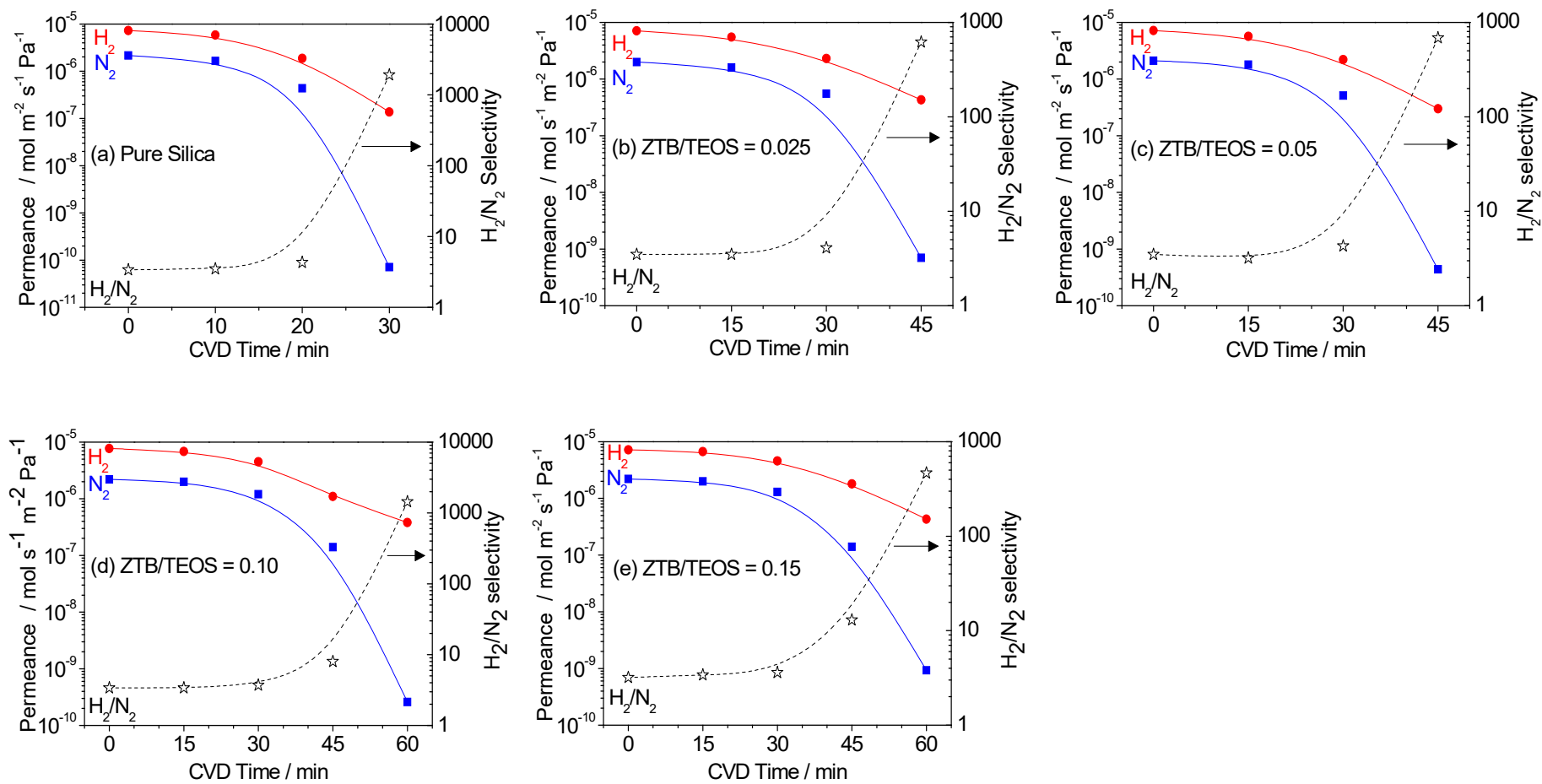


Figure 2.2. Changes in H₂ and N₂ permeance and H₂/N₂ selectivity with CVD time (923 K, ΔP = 0.24 MPa). (a) Pure silica membrane (b) 0.025Si-Zr (c) 0.05Si-Zr (d) 0.10Si-Zr (e) 0.15Si-Zr

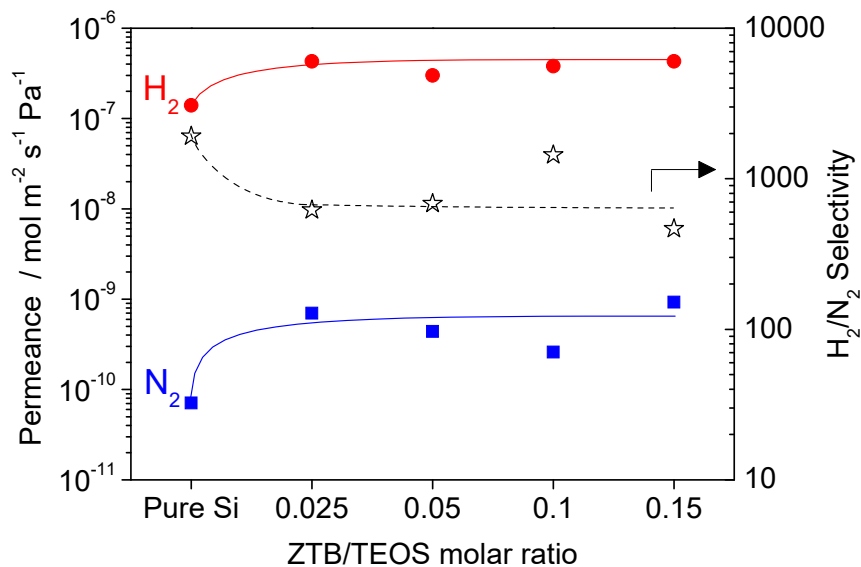


Figure 2.3. Permeation properties of membranes with the different molar ratios of ZTB/TEOS of 0-0.15 (923 K, $\Delta P = 0.24$ MPa)

Although the deposition rates on the membrane support decreased slightly with increasing molar ratio of ZTB/TEOS, the permeation properties of the membranes showed a similar behavior. At the beginning of the CVD, the H₂ and N₂ permeance decreased slowly, with the H₂/N₂ selectivity almost unchanged. With further progress of the CVD, the H₂ permeance continued to decrease slowly but the N₂ permeance dropped rapidly, resulting in an increase in the H₂/N₂ selectivity.

To compare the permeation properties of the prepared membranes in detail, the H₂ and N₂ permeances and H₂/N₂ selectivity are shown as a function of molar ratio of ZTB/TEOS in Figure 2.3. The H₂ permeance of the pure silica membrane prepared on the γ -alumina intermediate layer substrate after 30 min of CVD was 1.4×10^{-7} mol m⁻² s⁻¹ Pa⁻¹ and the selectivity was 1950, which are similar to values reported in previous studies [28,29,30]. For a molar ratio of ZTB/TEOS of 0.025, the H₂ and N₂ permeances increased slightly with a faster increase of the N₂ permeance than the H₂ permeance,

resulting in a decrease in the H_2/N_2 selectivity. With further increase of the molar ratio of ZTB/TEOS, the H_2 and N_2 permeances reached constant values at close to 4.3×10^{-7} mol $m^{-2} s^{-1} Pa^{-1}$ and 6.5×10^{-10} mol $m^{-2} s^{-1} Pa^{-1}$, while the H_2/N_2 selectivity stabilized at 660. The higher permeance of the silica-zirconia membrane is probably related to the bond lengths in the siloxane-based ring. Hacırlıoğlu et al. [31] reported that a zirconium substituted siloxane ring had longer Zr-O and Si-O bond lengths than those of the pure siloxane ring. The larger overall size of the siloxane ring containing Zr leads to lower activation energy for diffusion of gases, and enhances the permeance, but results in lower selectivities.

2.3.2. Morphology and structure of the silica-zirconia membranes

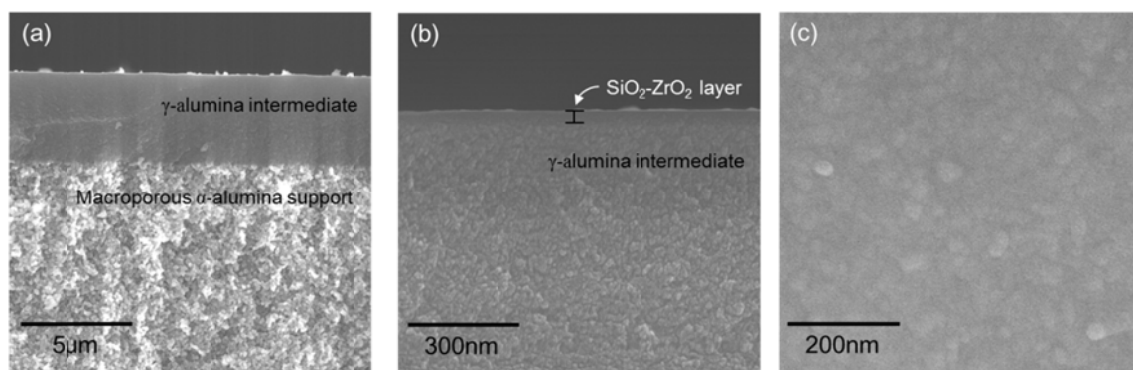


Figure 2.4. SEM images of the silica-zirconia composite membrane. (a) cross-section of the γ -alumina intermediate layer coated on macroporous α -alumina support (b) cross-section of the membrane 10Zr-Si (c) surface of the membrane 10Zr-Si

Figure 2.4 (a) shows a cross-sectional image of the γ -alumina intermediate layer and the macroporous α -alumina support, and Figure 2.4 (b-c) display a cross-sectional and surface image of the silica-zirconia composite membrane 10Si-Zr, which was prepared with a ZTB/TEOS molar ratio of 0.1. The γ -alumina intermediate layer, which

was prepared by sequentially placing coatings of boehmite sols of 80 nm and 60 nm of particle sizes, was well formed on the macroporous α -alumina support without visible cracking or infiltration. The overall thickness of the intermediate layer was around 3 μm . After 60 min of CVD on the alumina multilayer substrate, a thin and dense layer of silica-zirconia was formed on the top of the multilayer substrate, as observed in Figure 2.4 (b). The thickness of the composite top layer was measured to be around 30 nm. Figure 2.4 (c) shows that the surface of silica-zirconia composite layer is smooth and defect-free.

2.3.3. Permeation mechanism through silica-zirconia membrane

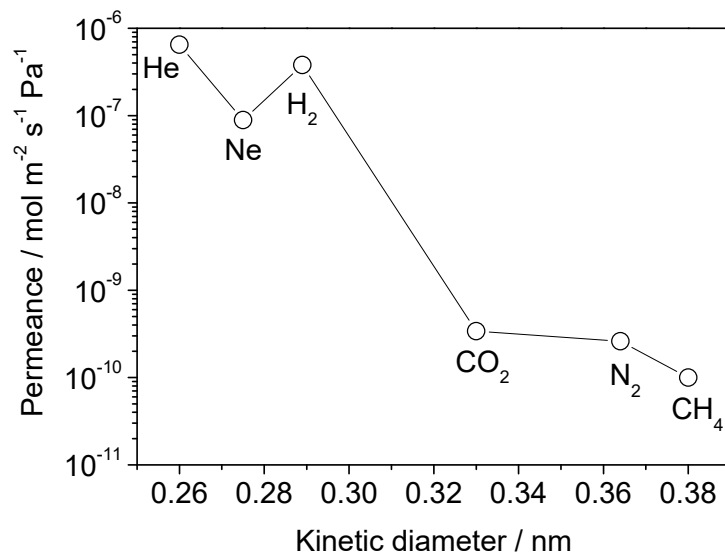


Figure 2.5. Permeance of various gases as a function of kinetic diameter at 923 K and $\Delta P = 0.24$ MPa

To investigate the permeation mechanism through the silica-zirconia composite membrane, permeance tests were conducted on the 10Si-Zr membrane, which was prepared by CVD for 60 min at 923 K with a molar ratio of ZTB/TEOS of 0.1, with

various pure gases such as He, Ne, H₂, CO₂, N₂ and CH₄ at 923 K. Figure 2.5 shows the permeance of the various gases as a function of their kinetic diameter. The order of permeance generally followed the molecular sizes of the gases. Smaller species such as He, Ne and H₂ had high permeance, while larger molecules like CO₂, N₂ and CH₄ had low permeance. However, the permeance of gases with molecular size smaller than 0.3 nm did not follow species size (H₂ = 0.289 nm, Ne = 0.275 nm, He = 0.26 nm) nor molecular weight (Ne = 20 g/mol, He = 4 g/mol, H₂ = 2 g/mol). This unusual order was also found in silica-based membranes, and was explained by the occurrence of a solid-state permeation mechanism involving jumps of permeating molecules between solubility sites [13,32]. The solubility and transport of small gaseous species in silicious materials is well known [33,34,35]. However, it was not until the solubility site mechanism was developed that the permeance in these materials could be fully understood.

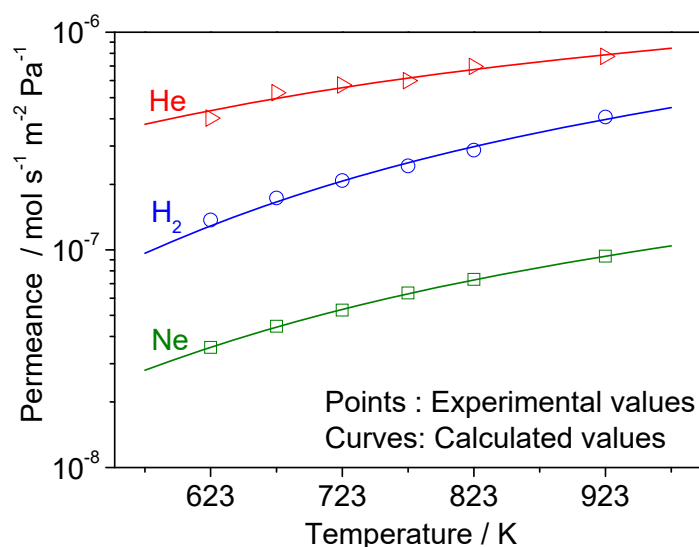


Figure 2.6. Temperature dependence of the permeances of He, Ne and H₂ through the 10Si-Zr membrane (solubility site model)

The experimental temperature dependence of the permeance of He, H₂ and Ne through this composite membrane is shown in Figure 2.6 as points. The permeance of the all gases increased with temperature, indicating an activated diffusion transport mechanism through the membrane for these small gases.

In order to quantitatively explain the mechanism of permeation of the small-sized gases through the silica-zirconia composite membrane, use was made of Eq. (2.3), derived earlier [36] using statistical mechanics. The equation has as parameters the number of solubility sites per m³ of membrane volume (N_s), the vibrational frequency of the species in the passageways between the sorption sites (ν^*), the activation energy of diffusion (ΔE_a) and the jump distance (d).

$$\bar{P}_i = \frac{1}{6L} \left(\frac{d^2}{h} \right) \left(\frac{h^2}{2\pi m_i kT} \right)^{3/2} \left(\frac{\sigma h^2}{8\pi^2 I kT} \right)^\alpha \times \frac{(N_s/N_A)}{(e^{h\nu^*/2kT} - e^{-h\nu^*/2kT})^2} e^{-\Delta E_a/RT} \quad (2.3)$$

where \bar{P}_i is the permeance of the gas i through the silica-zirconia composite top layer [$\text{mol m}^{-2} \text{s}^{-1} \text{Pa}^{-1}$], L the thickness of the top layer, m_i the mass of the species i , T temperature [K], h Planck's constant, k Boltzmann's constant, N_A Avogadro's number, R the gas constant, α an exponent accounting for incomplete loss of rotation (0 for He and Ne, and 0.2 for H₂), σ the symmetry factor of the species (2 for H₂), I the moment of inertia. The membrane thickness was 30 nm as obtained from the SEM image in Figure 2.4 (b). The permeance of the silica-zirconia composite layer was obtained by subtracting the resistance of γ -alumina intermediate layer (before CVD) from the resistance of silica-zirconia composite layer on the alumina substrate (after CVD):

$$\frac{1}{\bar{P}_{\text{silica-zirconia layer}}} = \frac{1}{\bar{P}_{\text{after CVD}}} - \frac{1}{\bar{P}_{\text{before CVD}}} \quad (2.4)$$

The calculated permeance is shown in Figure 2.6 as curves, and fits well the experimental points. The fitted parameters are summarized in Table 2.3. The number of

solubility sites N_S is in the order He>Ne>H₂, which follows the species size. This result is understandable since on average smaller molecules will fit into more solubility sites. The order of activation energy ΔE_a has an inverse relation with N_S because the larger molecules must overcome a larger barrier to squeeze through the silica-based rings. However, size is not the only factor that determines the permeance order. Another property that affects permeance is the jump frequency between sites and this has an inverse relationship with the mass of the species. This can be understood from consideration of the vibrational frequency of a harmonic oscillation, $\nu = \frac{1}{2\pi} \sqrt{\frac{k}{m}}$, which decreases as the reciprocal of the square root of the mass. As captured in Eq. (2.3), the permeance depends on both species size and mass, and gives rise to the order observed.

Table 2.3. Calculated parameters for the silica-zirconia composite membrane (solubility site model)

| Gases | Kinetic diameter / nm | Weight / a.u. | N_s / site m ⁻³ | ν^* / s ⁻¹ | ΔE_a / kJ mol ⁻¹ | d / nm | Regression coefficient |
|----------------|-----------------------|---------------|------------------------------|---------------------------|-------------------------------------|----------|------------------------|
| He | 0.260 | 4 | 9.32×10^{26} | 6.70×10^{12} | 6.0 | 0.8306 | 0.962 |
| Ne | 0.275 | 20 | 9.20×10^{26} | 3.90×10^{12} | 12.1 | 0.8308 | 0.999 |
| H ₂ | 0.289 | 2 | 9.10×10^{26} | 7.03×10^{12} | 15.8 | 0.8309 | 0.992 |

The activation energies in Table 2.3 are in the order He < Ne < H₂. This follows the order of sizes of He, Ne, and H₂, and make sense, as the species have to squeeze through openings between the solubility sites, and this is more difficult for the larger species. The activation energies are low, and this agrees with earlier results for silica membranes [13,14,32], and for vitreous glasses [33,34] and fused quartz [37]. Even for H in palladium it is found that activation energies for solid-state diffusion are small (30

kJ/mol) compared to those for adsorption or dissociation [38,39].

An alternative analysis for the permeance in silica-zirconia composite membrane has been recently proposed by Kanezashi et al. [40] using Eq. (2.5), which is based on a modified gas translation (GT) model [41].

$$P_i = \frac{\varepsilon}{3\tau L} (d_p - d_i) \frac{(d_p - d_i)^2}{d_p^2} \sqrt{\frac{8}{\pi M_i RT}} \exp\left(-\frac{E_{p,i}}{RT}\right)$$

$$= \frac{k_{0,i}}{\sqrt{M_i RT}} \exp\left(-\frac{E_{p,i}}{RT}\right) \quad (2.5)$$

$$k_{0,i} = \frac{\varepsilon}{3\tau L} \frac{(d_p - d_i)^3}{d_p^2} \sqrt{\frac{8}{\pi}} = a(d_p - d_i)^3 \quad (2.6)$$

where ε is the porosity, τ the tortuosity, d_p the pore size, d_i the molecular size of component i , and the others symbols are the same as above.

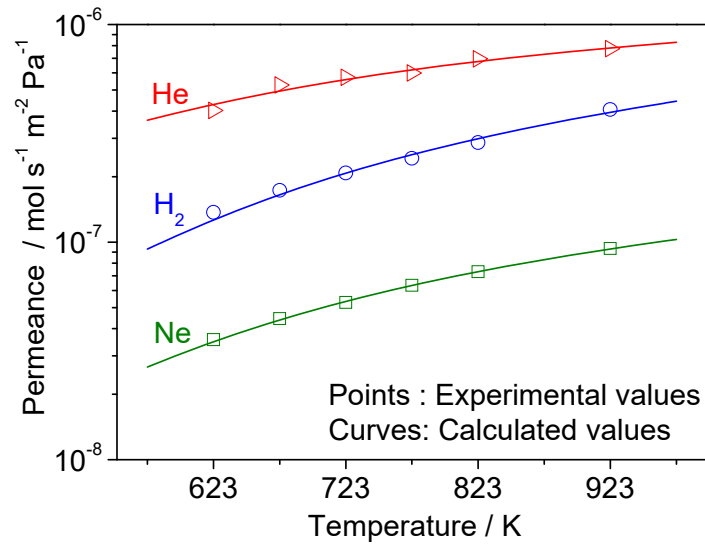


Figure 2.7. Temperature dependence of the permeances of He, Ne and H₂ through the 10Si-Zr membrane (gas translational model)

Although there is good fit between the experimental points and the calculated

permeance as shown in Figure 2.7 as curves, which are almost as good as those obtained by the statistical model above, the calculated parameters are not physically realistic. In particular, the pre-exponential factor $k_{0,i}$ are expected from Eq. (2.6), to increase with decreasing species size, since it should be easier for smaller species to fit through the presumed pored. However, this is not observed, and the calculated factor $k_{0,i}$ decrease with decreasing species size. Kanezashi et al. suggested that this unusual order is related to an effective molecular size, but this would result in molecular sizes that are impossible physically and would have no basis on theory. The failure to account for the species properties leads to the conclusion that the analysis by Kanezashi et al. is incorrect [32]. The interpretation of past work [42,43], which was based on the belief on a connected porous structure is brought into question. Our studies here show that jumps between solubility sites are involved in the mechanism of permeation of compact silica structures, and that this can be assessed by measurements of He, Ne, and H₂ permeance.

Table 2.4. Activation energy and pre-exponential factor, $k_{0,i}$, for silica-zirconia composite membrane (gas translational method)

| Gases | ΔE_a / kJ mol ⁻¹ | $k_{0,i}$ /- | Regression coefficient |
|----------------|--|----------------------|---------------------------|
| He | 12.6 | 2.2×10^{-5} | 0.968 |
| Ne | 18.7 | 1.3×10^{-5} | 0.999 |
| H ₂ | 21.2 | 2.5×10^{-5} | 0.988 |

The activation energies from the gas translational model (Table 2.4) follow the order He < Ne < H₂, which agree with the solubility site mechanism.

2.3.4. Hydrothermal stability of silica-zirconia composite membranes

Figure 2.8 (a) shows the H₂ permeance and Figure 2.8 (b) shows the N₂ permeance of the pure silica membrane and the silica-zirconia composite membranes as a function of exposure time to 16 mol% water vapor in Ar at 923 K. The H₂ permeance of the silica membrane decreased continuously to 68 % of the original value over the studied period of 48 h and showed no evidence of stabilization. Past work [13,14] indicated that this was due to densification which opens up pores. For the 10Si-Zr and 05Si-Zr membranes, the H₂ permeances decreased to 56 % and 67 %, respectively, which are slightly smaller levels of decrease than the pure silica membrane. However, the permeance curves are seen to be leveling off, which indicates that the membranes have hydrothermal stability. In particular, the H₂ permeance of the 10Si-Zr membrane was still above the order of 10^{-7} mol m⁻² s⁻¹ Pa⁻¹, which is the threshold level for practical applications [44]. Importantly, in contrast to the H₂ permeance, N₂ permeance decreased considerably with the increase of ZTB/TEOS molar ratio (Figure 2.8 (b)), so that the H₂/N₂ selectivity of the 10Si-Zr membrane showed the highest value of 5700 while the H₂/N₂ selectivity of the silica membrane showed the lowest value of 800.

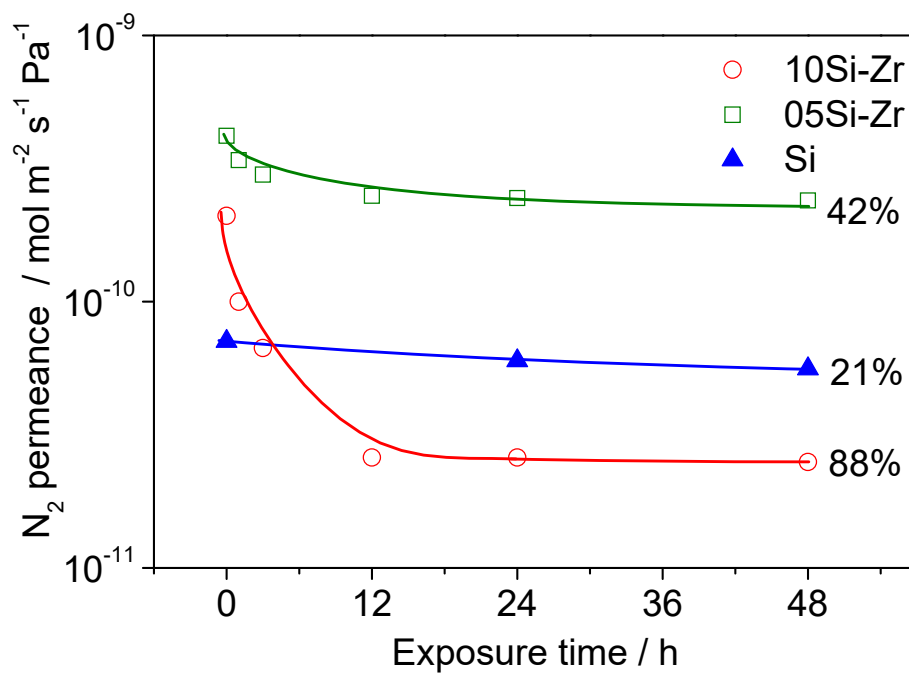
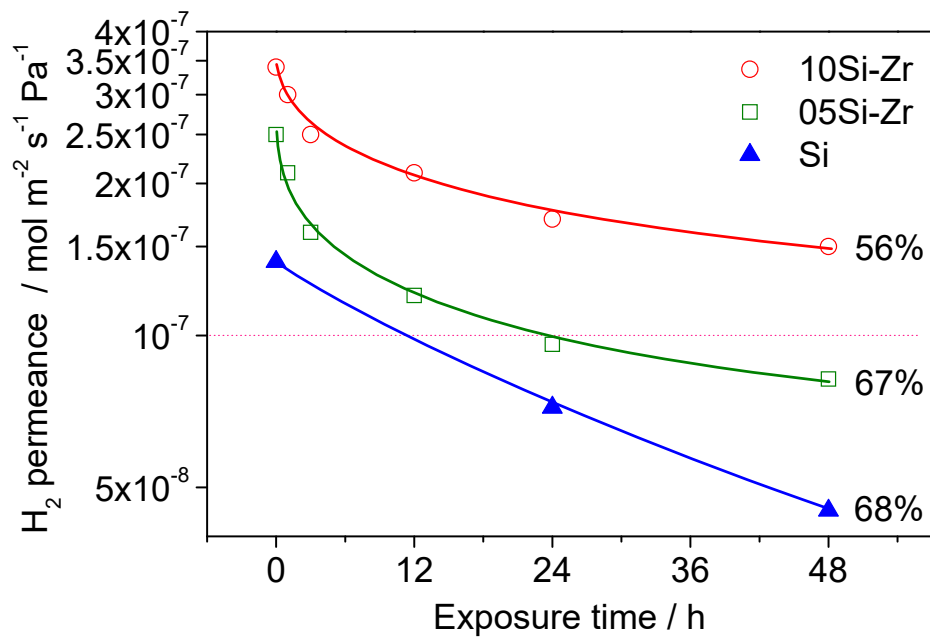


Figure 2.8. Effect of water upon H₂ and N₂ permeances. Pure silica and silica-zirconia composite membranes prepared using different molar ratios of ZTB/TEOS. Exposure to 16 mol% of water vapor at 923 K and 101 kPa for 48 h. (a) Changes of H₂ permeance (top) (b) Changes of N₂ permeance (bottom)

2.4. Conclusions

Hydrogen selective and hydrothermally stable silica-zirconia composite membranes were successfully prepared on a macroporous alumina support by chemical vapor deposition (CVD) with various molar ratios of zirconium (IV) *tert*-butoxide (ZTB) and tetraethylorthosilicate (TEOS) (0-0.15) at 923 K. With increase of the molar ratio of ZTB/TEOS, the H₂ and N₂ permeance increased slightly to a plateau, while the H₂/N₂ selectivity decreased slightly, and leveled off because of the more rapid increase of the N₂ permeance than the H₂ permeance.

Studies of the 10Si-Zr membrane, which was prepared with a molar ratio of ZTB/TEOS of 0.1, were carried out to determine the mechanism of permeance. Levels of H₂ permeance of 3.9×10^{-7} mol m⁻² s⁻¹ Pa⁻¹ and H₂/N₂ selectivity of 780 were attained. The thickness of this membrane was around 30-35 nm as measured by SEM. Results of permeation tests of He, H₂, and Ne as a function of temperature were well described by a solid-state permeation mechanism involving jumps between solubility sites. The fitting parameters were physically realistic, and described the results well. An alternative theory based on a gas-translational method was shown not to be valid because it gave physically incorrect parameters and trends. To determine the mechanism of permeance in silica membranes it is essential to analyze the results of He, H₂, and Ne probes.

After exposure to 16 mol% water vapor at 923 K for 48 h, the H₂ permeance through 10Si-Zr membrane decreased by 56 %, but stabilized at an order of 10^{-7} mol m⁻² s⁻¹ Pa⁻¹. Thus, hydrothermally stable membranes were achieved by the formation of silica-zirconia composite membranes.

Reference

- [1] R. Chaubey, S. Sahu, O.O. James, S. Maity, A review on development of industrial processes and emerging techniques for production of hydrogen from renewable and sustainable sources, *Renew. Sust. Energy Rev.* 23 (2013) 443-462.
- [2] S.J. Khatib, K. de Souza, F.B. Noronha, S.T. Oyama, Review of silica membranes for hydrogen separation prepared by chemical vapor deposition (CVD) in *Inorganic, Polymeric, and Composite Membranes: Structure-Function and Other Correlations*, S. Ted Oyama, Susan Michelle Stagg-Williams, Eds. Elsevier, Amsterdam, 2011, pp. 25-60, *Membr. Sci. Technol.* 14 (2011) 25-60.
- [3] H.B. Wang, Y.S. Lin, Highly stable bilayer MFI zeolite membranes for high temperature hydrogen separation, *J. Membr. Sci.* 450 (2014) 425-432.
- [4] A.E. Lewis, H. Zhao, H. Syed, C.A. Wolden, J.D. Way, PdAu and PdAuAg composite membranes for hydrogen separation from synthetic water-gas shift streams containing hydrogen sulfide, *J. Membr. Sci.* 465 (2014) 167-176.
- [5] S.J. Khatib, S.T. Oyama, Review of silica membranes for hydrogen separation prepared by chemical vapor deposition (CVD), *Separ. Purif. Technol.* 111 (2013) 20-42.
- [6] F. Gallucci, E. Fernandez, P. Corengia, M.S. Annaland, Recent advances on membranes and membrane reactors for hydrogen production, *Chem. Eng. Sci.* 92 (2013) 40-66.
- [7] Y.S. Lin, Microporous and dense inorganic membranes: current status and prospective, *Sep. Purif. Tech.* 25 (2001) 39-55.
- [8] T. Tsuru, K. Yamaguchi, M. Asaeda, Methane steam reforming by microporous catalytic membrane reactors, *AIChE J.* 50 (2004) 2794-2805.
- [9] G.P. Fotou, Y.S. Lin, S.E. Pratsinis, Hydrothermal stability of pure and modified microporous silica membranes, *J. Mater. Sci.* 30 (1995) 2803-2808.
- [10] J.H.A. Hekkink, R.S.A. de Lange, A.A. Ten Hoeve, P.J.A.M. Blankenvoorde, K.Keizer,A.J. Burggraaf, Characterization and permeation properties of binary SiO₂-TiO₂ and SiO₂-Al₂O₃ modified gamma-alumina membranes, *Key Eng. Mater.* 61&62 (1991) 375-378.
- [11] K. Yoshida, Y. Hirano, H. Fujii, T. Tsuru, M. Asaeda, Hydrothermal stability and performance of silica-zirconiz membranes for hydrogen separation in

-
- hydrothermal conditions, *J. Chem. Eng. Jpn.* 34 (2001) 523-530.
- [12] L. Liu, D.K. Wang, D.L. Martens, S. Smart, J.C. Diniz da Costa, Binary gas mixture and hydrothermal stability investigation of cobalt silica membranes, *J. Membr. Sci.* 493 (2015) 470-477.
- [13] Y. Gu, P. Hacıoğlu, S.T. Oyama, Hydrothermally stable silica-alumina composite membranes for hydrogen separation, *J. Membr. Sci.* 310 (2008) 28-37.
- [14] Y. Gu, S.T. Oyama, Permeation properties and hydrothermal stability of silica-titania membranes supported on porous alumina substrates, *J. Membr. Sci.* 345 (2009) 267-275.
- [15] T. Okubo, H. Inoue, Introduction of specific gas selectivity to porous glass membranes by treatment with tetraethoxysilane, *J. Membr. Sci.* 42 (1989) 109-117.
- [16] G.R. Gavalas, C.E. Megiris, S.W. Nam, Deposition of H₂-permselective SiO₂ films, *Chem. Eng. Sci.* 44 (1989) 1829-1835.
- [17] H. Ohya, H. Nakajima, N. Togami, M. Aihara, Y. Negishi, Separation of hydrogen from thermochemical processes using zirconia-silica composite membrane, *J. Membr. Sci.* 97 (1994) 91-98.
- [18] H. Ohya, H. Nakajima, N. Togami, H. Ohashi, M. Aihara, S. Tanisho, Y. Negishi, Hydrogen purification using zirconia-silica composite membranes for thermochemical process, *Int. J. Hydrogen Energy*, 22 (1997) 509-515.
- [19] T. Tsuru, S. Wada, S. Izumi, M. Asaeda, Silica-zirconia membranes for nanofiltration, *J. Membr. Sci.* 149 (1998) 127-135.
- [20] T. Tsuru, T. Sudoh, T. Yoshioka, M. Asaeda, Nanofiltration in non-aqueous solutions by porous silica-zirconia membranes, *J. Membr. Sci.* 185 (2001) 235-261.
- [21] Y.F. Gu, B.H. Jeong, K.I. Sotowa, K. Kusakabe, The effect of humidity on the durability of inorganic membranes, *J. Chem. Eng.* 20 (2003) 1079-1084.
- [22] A. Urriaga, C. Casado, M. Asaeda, I. Ortiz, Comparison of SiO₂-ZrO₂-50% and commercial SiO₂ membranes on the pervaporative dehydration of organic solvents, *Desalination*. 193 (2006) 97-102.
- [23] S. Araki, Y. Kiyohara, S. Imasaka, S. Tanaka, Y. Miyake, Preparation and pervaporation properties of silica-zirconia membranes, *Desalination*. 266 (2011)

46-50.

- [24] H.S. Choi, C.H. Ryu, G. J. Hwang, Obtention of ZrO₂-SiO₂ hydrogen permselective membrane by chemical vapor deposition method, *Chem. Eng. J.* 232 (2013) 302-309.
- [25] L. Li, H. Qi, Gas separation using sol-gel derived microporous zirconia membranes with high hydrothermal stability, *Chin. J. Chem. Eng.* 23 (2015) 1300-1306.
- [26] Y. Gu, S.T. Oyama, Ultrathin, hydrogen-selective silica membranes deposited on alumina-graded structures prepared from size-controlled boehmite sols, *J. Membr. Sci.* 306 (2007) 216-227.
- [27] X. Zhang, H. Yamada, T. Saito, T. Kai, K. Murakami, M. Nakashima, J. Ohshita, K. Akamatsu, S.-I. Nakao, Development of hydrogen-selective triphenylmethoxysilane-derived silica membranes with tailored pore size by chemical vapor deposition, *J. Membr. Sci.* 499 (2016) 28-35.
- [28] D. Lee, L. Zhang, S.T. Oyama, S. Niu, R.F. Saraf, Synthesis, characterization, and gas permeation properties of a hydrogen permeable silica membrane supported on porous alumina, *J. Membr. Sci.* 231 (2004) 117-126.
- [29] M. Nomura, K. Ono, S. Gopalakrishnan, T. Sugawara, S.-I. Nakao, Preparation of a stable silica membrane by a counter diffusion chemical vapor deposition method, *J. Membr. Sci.* 251 (2005) 151-158.
- [30] S. Gopalakrishnan, Y. Yoshino, M. Nomura, B.N. Nair, S.-I. Nakao, A hybrid processing method for high performance hydrogen-selective silica membranes, *J. Membr. Sci.* 297 (2007) 5-9.
- [31] P. Hacıoğlu, L. Achenie, S.T. Oyama, Ab initio studies of silica-based membranes: Activation energy of permeation, *Membr. Sci. Technol.* 14 (2011) 79-90.
- [32] S.T. Oyama, M. Yamada, T. Sugawara, A. Takagaki, R. Kikuchi, Review on mechanisms of gas permeation through inorganic membranes, *J. Jpn. Petrol. Inst.* 54 (2011) 298-309.
- [33] J.E. Shelby, Pressure dependence of helium and neon solubility in vitreous silica, *J. Appl. Phys.* 47 (1976) 135.

-
- [34] J.E. Shelby, Molecular diffusion and solubility of hydrogen isotopes in vitreous silica, *J. Appl. Phys.* 48 (1977) 3387.
- [35] R.M. Barrer, D.E.W. Vaughan, Solution and diffusion of helium and neon in tridymite and cristobalite, *Trans. Faraday Soc.* 63 (1967) 2275.
- [36] S.T. Oyama, D. Lee, P. Hacırlıoğlu, R.F. Saraf, Theory of hydrogen permeability in nonporous silica membranes, *J. Membr. Sci.* 244 (2004) 45-33.
- [37] R.W. Lee, R.C. Frank, D.E. Swets, Diffusion of hydrogen and deuterium in fused quartz, *J. Chem. Phys.* 36 (1962) 1062.
- [38] A. Caravella, F. Scura, G. Barbieri, E. Drioli, Sieverts law empirical exponent for Pd based membranes: critical analysis in pure H₂ permeation, *J. Phys. Chem. B* 114 (2010) 6033–6047.
- [39] S. Yoon, S. T. Oyama, Correlations in palladium membranes for hydrogen separation: A review, *J. Membr. Sci.* 375 (2011) 28-45.
- [40] M. Kanezashi, T. Sasaki, H. Tawarayama, H. Nagasawa, T. Yoshioka, K. Ito, T. Tsuru, Experimental and theoretical study on small gas permeation properties through amorphous silica membranes fabricated at different temperatures, *J. Phys. Chem.* 118 (2014) 20323-20331.
- [41] H.R. Lee, M. Kanezashi, Y. Shimomura, T. Yoshioka, T. Tsuru, Evaluation and fabrication of pore-size-tuned silica membranes with tetraethoxydimethyl disiloxane for gas separation, *AIChE J.* 57 (2011) 2755-2765.
- [42] M. Kanezashi, K. Yada, T. Yoshioka, T. Tsuru, Organic-inorganic hybrid silica membranes with controlled silica network size: Preparation and gas permeation characteristics, *J Membr Sci.* 384 (2010) 310–318.
- [43] T. Tsuru, Y. Takata, H. Kondo, F. Hirano, T. Yoshioka, M. Asaeda, Characterization of sol-gel derived membranes and zeolite membranes by nanoporometry, *Sep Purif Technol.* 32 (2003) 23–27.
- [44] H. Lim, Y. Gu, S.T. Oyama, Studies of the effect of pressure and hydrogen permeance on the ethanol steam reforming reaction with palladium- and silica-based membranes, *J. Membr. Sci.* 396 (2012) 115-127.

Chapter 3

Synthesis and Characterization of Hydrogen Selective Silica Membrane Prepared by Chemical Vapor Deposition of Vinyltriethoxysilane

3.1. Introduction

Gas separation membrane technology has been receiving increasing attention because of its inherent advantages in energy-efficiency, cost-effectiveness and environmental compatibility over other methods like distillation or pressure swing adsorption [1,2]. Among gas separation membranes, inorganic silica membranes are promising materials at high temperatures due to their excellent hydrogen separation properties with high chemical resistance and thermal stability, as well as moderate cost [3]. Since the first reports of silica-based membranes by Okubo and Inoue [4] and the group of Gavalas [5], tetraethylorthosilicate (TEOS)-derived silica-based membranes have been intensely studied and synthesis by sol-gel methods [6,7,8,9] and chemical vapor deposition (CVD) methods [10,11,12,13] have been reported. From previous studies TEOS-derived membranes are comprised of a silica network with isolated solubility sites of about 0.3 nm that allow only small molecules such as helium (0.260 nm), neon (0.275 nm) and hydrogen (0.289 nm) to permeate by a solid-state hopping mechanism, resulting in high hydrogen selectivity over large molecules such as nitrogen (0.364 nm) and methane (0.380 nm) [14,15]. For that reason TEOS-derived membranes have been used in various applications, such as methane-steam reforming, where

hydrogen separation is important [16,17]. However, the small size of the openings and low hydrothermal stability of TEOS-derived pure silica membranes have limited the widespread applications of the membranes, and hence development of a controllable silica network size and improvement of hydrothermal stability are highly desirable [18,19]. Precursors in which the siloxanes are substituted with large pendant groups give rise to a connected pore structure and enhanced permeance in certain cases [20]. In addition, the organic moieties can improve hydrothermal stability because of their hydrophilicity [21,22,23].

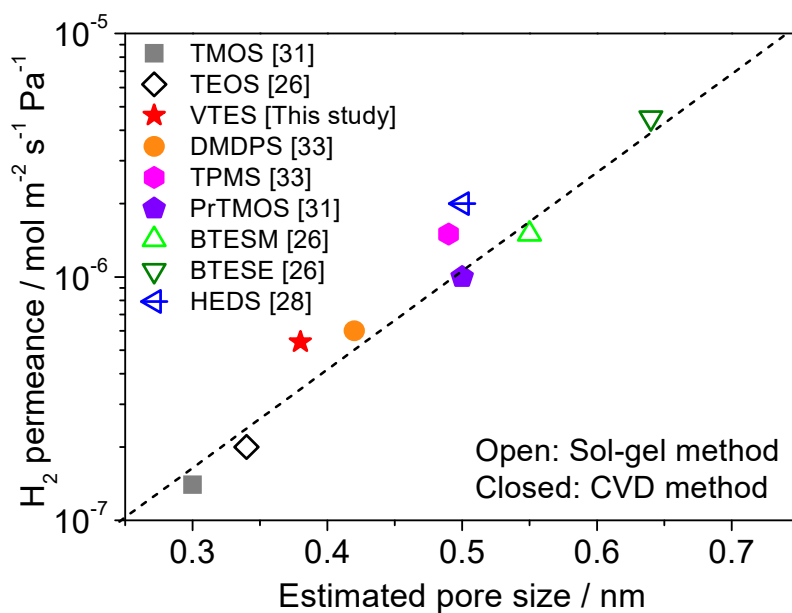


Figure 3.1. Comparison of H₂ permeance for various silica membranes as a function of their estimated pore size

Although H₂-selective, pure silica membranes prepared by CVD consist of a continuous silicious network with pores only present as defects, it is possible to design materials with pores useful for the separation of larger gaseous molecules. Raman and

Brinker first proposed a method to control the pore size of microporous silica membranes by using templates in the sol-gel method [24], and since then there have been a number of reports on the tuning of the network size of silica membranes by using various silica precursors via both the sol-gel and CVD methods. Figure 3.1 shows the H₂ permeance of silica membranes derived from different silica precursors as a function of their estimated pore size. Kanezashi et al. prepared organic-inorganic hybrid silica membranes by the sol-gel method using bridged alkoxides such as bis(triethoxysilyl)methane (BTESM), bis(triethoxysilyl)ethane (BTESE) as silica precursors [25,26]. The pore size distribution determined by fitting to a normalized Knudsen-based permeance (NKP) suggested that the average pore size was in the following order: BTESE-derived silica (0.64 nm) > BTESM-derived silica (0.55 nm) > TEOS-derived silica (0.34 nm). It should be noted that the BTESM-derived membranes showed a high C₃H₆ permeance of $6.32 \times 10^{-7} \text{ mol m}^{-2} \text{ s}^{-1} \text{ Pa}^{-1}$ with a selectivity over C₃H₈ of 8.8 at 323 K indicating reasonably good pore size control. Lee et al. prepared silica membranes by the sol-gel method using disiloxanealkoxides such as tetraethoxydimethyldisiloxane (TEDMDS) and hexaethoxydisiloxane (HEDS) [27,28]. The order of estimated pore size was TEDMDS-derived silica (0.70 nm) > HEDS-derived silica (0.50 nm) > TEOS-derived silica (0.32 nm). The TEDMDS-derived membrane had high H₂ permeance of the order of $10^{-6} \text{ mol m}^{-2} \text{ s}^{-1} \text{ Pa}^{-1}$, but low H₂/N₂ selectivity below 20 indicating that permeance occurred through the pores. Kusakabe et al. prepared silica membranes by the sol-gel method using mixtures of TEOS and pendant-type alkoxides with carbon chain substitution such as octyltriethoxysilane, dodecyltriethoxysilane (DTEOS) and octadecyl-triethoxysilane. The TEOS-DTEOS-derived membrane showed a higher pore size distribution than the TEOS-derived

membrane of around 0.3-0.4 nm, which was estimated based on single gas permeation tests [29]. Nomura et al. prepared a silica membrane by the counter diffusion CVD method using tetramethoxysilane (TMOS) and O₂ [30]. The membrane had H₂ permeance of 1.5×10^{-7} mol m⁻² s⁻¹ Pa⁻¹ and H₂/N₂ selectivity over 1000, and was stable under the typical steam-reforming conditions of methane (76 kPa of steam at 773 K) for 21 h. Nomura et al. also prepared silica membranes using various pendant type alkoxides such as methyltrimethoxysilane (MTMOS), trimethylmethoxysilane (TMMOS), propyltrimethoxysilane (PrTMOS), phenyltrimethoxysilane (PhTMOS) [31]. The membranes prepared using methyl substituted precursors had H₂ permeance of 0.6- 1.4×10^{-7} mol m⁻² s⁻¹ Pa⁻¹ and H₂/N₂ selectivity over 200 with estimated pore sizes of about 0.3 nm. The membranes prepared using larger functional group (PrTMOS, PhTMOS) showed an order of magnitude higher H₂ permeance but smaller H₂/N₂ selectivity below 40 with maximum pore sizes around 0.5 nm. Thus, the authors concluded that the pore size of the silica membranes can be controlled by changing the type of silica precursors. Nakao and collaborators prepared silica membranes by the counter-diffusion CVD method using methoxysilanes with different numbers of substituted phenyl groups such as phenyltrimethoxysilane (PTMS), dimethoxydiphenylsilane (DMDPS) and triphenylmethoxysilane (TPMS) at 873 K [32,33]. The order of estimated pore size based on the normalized Knudsen-based permeance was TPMS-derived silica (0.486 nm) > DMDPS-derived silica (0.42 nm) > PTMS-derived silica. The DMDPS and TPMS-derived membranes had high H₂ permeances of the order of 10^{-6} mol m⁻² s⁻¹ Pa⁻¹ and high H₂/SF₆ selectivity of over 6800 and 12000, respectively. However, SF₆ is a large species and high selectivities are expected. Generally, it was demonstrated that the silica network size was enlarged when

the number of phenyl groups on the silicon source increased because larger spaces surrounded the aromatic moieties. However, in the latter investigation and many others cited above, the measurement of He, H₂ and Ne were not carried out, and this determination is crucial for determining the permeation mechanism and whether pores are actually present [34].

This chapter describes the preparation of silica membranes on porous alumina substrates (60 nm) by chemical vapor deposition (CVD) of vinyltriethoxysilane (VTES), a precursor containing a vinyl group that has not been studied before. The objectives were to investigate the effect of the vinyl group on the H₂ permeance and H₂/C₂H₆ selectivities. Scanning electron microscopy (SEM) and in situ Fourier transform infrared (FTIR) measurements were used to characterize the morphology and structure of the membrane after CVD. The permeation properties, including those of He, H₂, and Ne, hydrothermal stability, and permeation mechanism of the prepared membranes are discussed in detail.

3.2. Experimental

3.2.1. Preparation and characterization of VTES-derived silica membrane

The VTES-derived silica membrane in this work consisted of three layers: a macroporous α -alumina support, a γ -alumina intermediate layer and a VTES-derived silica layer. A commercial porous α -alumina support was used (Noritake Corporation, O.D.= 6 mm, I.D.= 4 mm, length = 30 mm, nominal pore size = 60 nm) which was attached to non-porous alumina tubes using glass joints obtained by melting a glass paste (Nippon Electric Glass Co., Ltd) at 1273 K for 10 min.

The γ -alumina intermediate layer was prepared by a dipping-calcining method on

the macroporous α -alumina support. First, the outside of the support was wrapped with Teflon, then the tube was immersed into a dipping solution containing a boehmite sol of size 80 nm for 10 s, and finally the tube was dried in air for 6 h. Following this, the dried support was heated to 923 K in air at a rate of 1.5 K min⁻¹ and calcined at 923 K for 3 h. In order to prepare a uniform and defect free membrane surface, this dipping-calcining process was repeated two times using different dipping solutions containing boehmite sols of particle size 80 nm and 60 nm.

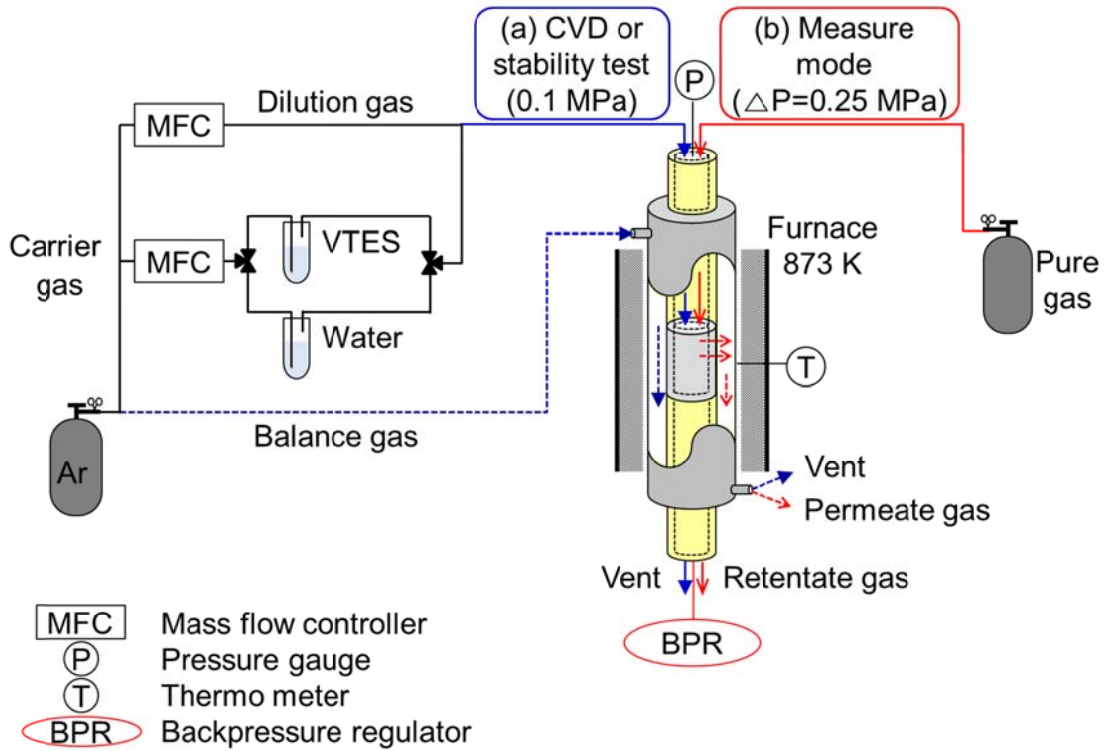


Figure 3.2. Schematic of experimental setup for membrane preparation and testing (a) Chemical vapor deposition (CVD) process and hydrothermal stability test (873 K, 0.1 MPa) (b) Permeability test (473-873 K, $\Delta P = 0.25$ MPa)

The dipping solutions were synthesized by mixing the boehmite sols with a

polyvinyl alcohol (PVA, Polysciences, Inc. M.W. ~78,000) solution and diluting with distilled water to obtain a 0.15 M concentration of the sol and a 0.35 wt. % concentration of the PVA. This procedure is similar to that described previously by the group of Oyama [35]. The boehmite sols were synthesized using a sequence of hydrolysis of aluminum alkoxides and acid peptization, with first 0.13 mol of aluminum isopropoxide (Aldrich, 98%) added to 200 ml of distilled water at 371 K, and stirred with 550 rpm for 24 h. Then, a quantity of nitric acid (Wako, 60%) was slowly added to the solution to give a molar ratio of H^+ /alkoxide of 0.025 or 0.07, after which the mixture was stirred for 24 h. The mean diameters of the sols were measured by a dynamic light scattering analyzer (Horiba Model LB-550), which was calibrated using standard polystyrene latex microsphere solutions with mean diameter of 50 nm and 100 nm (Polysciences, Inc.): the measured mean diameters were 80 nm and 60 nm for molar ratios of H^+ /alkoxide of 0.025 and 0.07, respectively.

The VTES-derived silica layer was prepared by the CVD method on the γ -alumina intermediate layer. Figure 3.2 (a) shows a schematic of the CVD apparatus. The CVD was conducted using vinyltriethoxysilane (VTES, TCI, 98 %) as silica precursor at 873 K and 0.1MPa with the VTES bubbler maintained at room temperature. After heating the apparatus to 873 K at a rate of 1.5 K min^{-1} , 13 cm^3 (NTP) min^{-1} (9.7 $\mu mol s^{-1}$) of 0.14 mol% VTES gas, which included 3.5 cm^3 (NTP) min^{-1} (2.6 $\mu mol s^{-1}$) of VTES containing carrier gas and 9.5 cm^3 (NTP) min^{-1} (7.1 $\mu mol s^{-1}$) of dilution gas, was flowed on the inside of the support and 13 cm^3 (NTP) min^{-1} (9.7 $\mu mol s^{-1}$) of balance gas was introduced to the outside of the support. The CVD was conducted until an adequate H_2 permeance and H_2/N_2 selectivity were obtained by interrupting the CVD and checking the performance of the membrane periodically. The permeance was

measured without removing the membrane from the CVD unit, and the procedure is explained in section 3.2.3.

The morphology of the VTES-derived silica membrane was obtained using a field emission scanning electron microscope (FE-SEM, Hitachi S-900). The cross-section and surface of the membrane were lightly coated with Pt-Pd by ion sputtering (E-1030, Hitachi) with a current of 15 mA for 15s.

3.2.2. Fourier transform infrared (FTIR) analysis

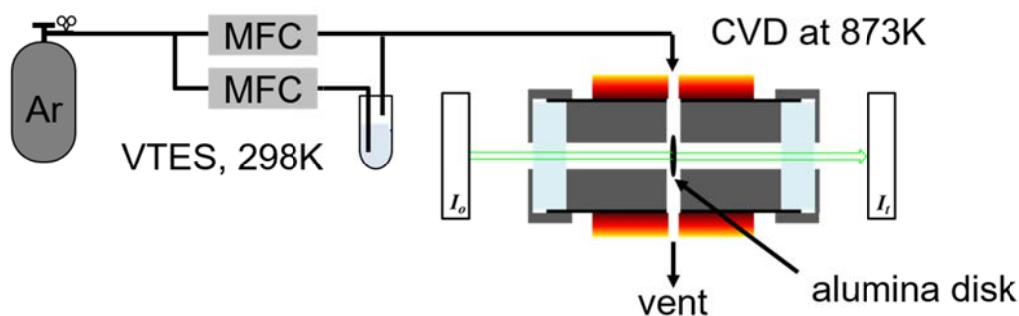


Figure 3.3. Schematic of experimental setup for the FTIR apparatus

The Fourier transform infrared (FTIR) spectra of the VTES-derived layer on a γ -alumina disk were recorded using a FTIR spectrometer (FT/IR-6100, JASCO). A schematic of the apparatus is shown in Figure 3.3. The self-supporting γ -alumina disk of diameter 1 cm (20 mg) was prepared with the calcined boehmite sol of particle size of 60 nm used in the preparation of the membranes, and was placed in the center of a cell equipped with KBr windows which were cooled to 303 K by a circulation cooler. Prior to the measurements, background spectra were recorded at 873 K. In the same manner as the CVD procedure, Ar flow was introduced via a bubbler containing VTES to the cell for 130 min at 873 K. The bubbler was kept at 298 K to give 0.14 mol% of VTES in

Ar. After the CVD, 16 mol% of water was treated to the cell for 1 h in the same manner as the hydrothermal stability test. Spectra were recorded in the absorbance mode at 873 K with a resolution of 4 cm^{-1} using 200 scans in the region of $4,000\text{--}700\text{ cm}^{-1}$.

3.2.3. Permeability and hydrothermal stability test for VTES-derived silica membrane

The permeance of various gases such as He, Ne, H₂, CO₂, N₂, CO, and CH₄ were measured at temperatures ranging from 573 K to 873 K. The temperature was varied downward and upward in the order: 873, 673, 473, 573 and 773 K to verify that the membrane was not changing in the course of the measurements. After purging the inside of the support under a flow of the corresponding pure gas for 10 min, the inside of the support was pressurized to around 0.35 MPa by closing a backpressure regulator (BPR) (Figure 3.2 (b)). Then the flow rate of permeate gas was measured directly with a flow meter (Agilent Technologies, AD1000) for large flow rates or with a micro gas chromatograph (micro GC, Agilent Technologies, 490 micro GC, a molecular sieve 5A column was used for N₂ and CO and a Porapak Q column was employed for CO₂ and CH₄) for small flow rates, where the concentration of the permeate in a known flow of carrier was measured.

A hydrothermal stability test was carried out with 16 mol% of water vapor diluted in Ar flow at 873 K and 0.1 MPa for 72 h. For this condition, $10\text{ cm}^3\text{ (NTP) min}^{-1}$ ($7.4\text{ }\mu\text{mol s}^{-1}$) of carrier gas, which was passed through a heated bubbler containing distilled water at 329 K and 0.1 MPa, was introduced to the inside of the support while flowing $10\text{ cm}^3\text{ (NTP) min}^{-1}$ ($7.4\text{ }\mu\text{mol s}^{-1}$) of Ar on the outside of the support. The permeances of H₂ and N₂ were measured periodically during the test.

The permeance of pure gases was calculated by using Eq. (3.1):

$$\bar{P}_i = \frac{F_i}{A\Delta P_i} \quad (3.1)$$

where \bar{P}_i is the permeance of species i [$\text{mol m}^{-2} \text{s}^{-1} \text{Pa}^{-1}$], A is the surface area of the membrane [m^2], F_i is the molar flow rate of the gas i [mol s^{-1}] and ΔP_i is the partial pressure difference of gas i between the inner and the outer side of the membrane tube [Pa].

The ideal selectivity was defined as the ratio of the single-gas permeances as given by Eq. (3.2).

$$S_{i,j} = \frac{\bar{P}_i}{\bar{P}_j} \quad (3.2)$$

where $S_{i,j}$ is the ideal selectivity of a species i over j , \bar{P}_i and \bar{P}_j are the permeances of species i and j , respectively [$\text{mol m}^{-2} \text{s}^{-1} \text{Pa}^{-1}$].

3.3. Results and discussion

3.3.1. Preparation of VTES-derived membrane

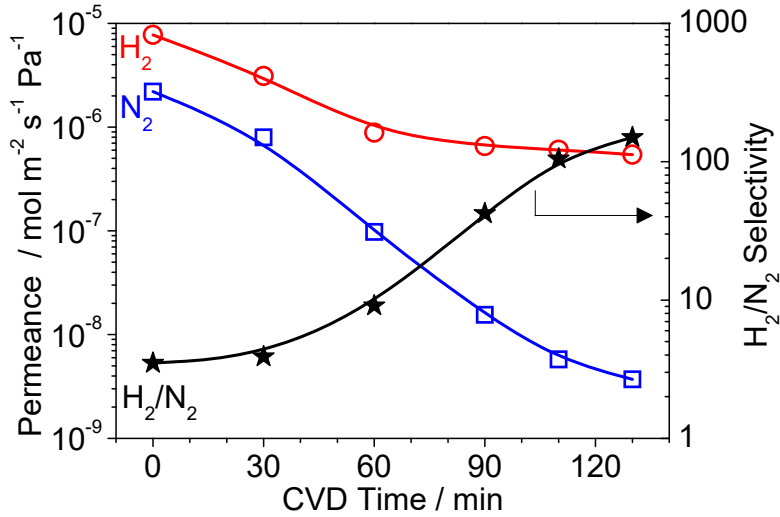


Figure 3.4. Changes in H₂ and N₂ permeance and H₂/N₂ selectivity with CVD time (CVD conditions: 873 K, 0.25 MPa)

The CVD was conducted on the alumina substrate using VTES as silica precursor at 873 K, and the changes in the H₂ and N₂ permeances and the H₂/N₂ ideal selectivity as a function of CVD time are shown in Figure 3.4. Before the CVD, the alumina substrate had high H₂ and N₂ permeances of the order of 10⁻⁶ mol m⁻² s⁻¹ Pa⁻¹ with a H₂/N₂ selectivity of 3.5, which was close to the value of 3.7 predicted for Knudsen diffusion. For the first 1 h, the H₂ and N₂ permeances decreased and the H₂/N₂ selectivity increased slightly. With further progress of the CVD, the H₂ permeance became almost stable but the N₂ permeance decreased rapidly, resulting in an increase in the H₂/N₂ selectivity. This trend is usually observed in silica-based membranes prepared using the CVD method and the result indicates that passageways through which the N₂ could pass were blocked out that the H₂ selective layer was successfully formed on the support. After 130 min of CVD, the VTES-derived silica membrane had a higher H₂ permeance of 5.4 × 10⁻⁷ mol m⁻² s⁻¹ Pa⁻¹ than the TEOS-derived pure silica membrane of 1.4 × 10⁻⁷ mol m⁻² s⁻¹ Pa⁻¹ but lower H₂/N₂ selectivity of 150 versus 1950 [34]. This is probably caused by the presence of the vinyl groups, which do not allow the formation of a continuous network of siloxy bonds. Still, a selectivity above 100 is sufficient for practical applications in membrane reactors [36].

3.3.2. Morphology and structure of VTES-derived membrane

Scanning electron microscopy (SEM) images of a cross-section of the VTES-derived membrane are shown in Figure 3.5 (a, b). The γ -alumina intermediate layer, which was prepared by sequentially depositing coatings of boehmite sols of 80 nm and 60 nm of particle sizes, was well formed on the macroporous α -alumina support without visible cracking or infiltration (Figure 3.5 (a)). After 130 min of CVD on the γ -alumina

intermediate layer, a dense VTES-derived silica layer was formed with a thickness of around 200 nm (Figure 3.5 (b)).

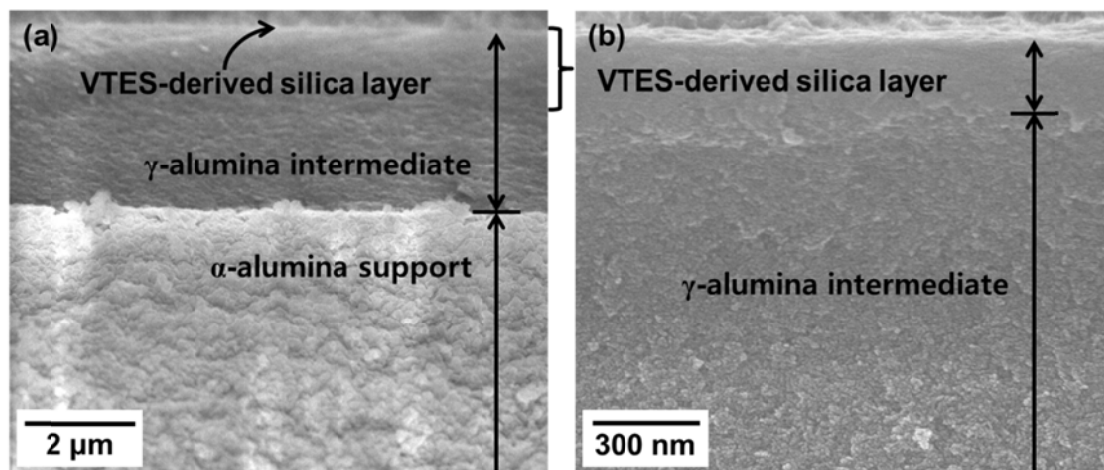


Figure 3.5. SEM images of the cross-section of the VTES-derived silica membrane. (a) Overall structure at low magnification (b) Surface layer at high magnification

To analyze the structure of the VTES-derived membrane, in situ FTIR measurements were applied on the calcined γ -alumina disk for CVD, thermal stability and hydrothermal stability tests at 873 K. The IR measurements were conducted in absorbance mode using a spectrum (before CVD) as background, and for this reason the spectrum before CVD is flat. After 130 min of CVD using VTES, there are three well-defined peaks at 1566, 1456, and 1232 cm^{-1} corresponding to C=C vibrations, in-plane C-H deformation vibration of the $-\text{CH}=\text{CH}_2$ (vinyl) groups, and typical Si-O covalent bonds vibrations, respectively [37,38]. Interestingly, it was found that there was absence of a bond at 1384 cm^{-1} belonging to ethoxy groups derived from VTES. These results indicate that the ethoxy groups were consumed to form the silica network, but that at least some of the vinyl groups were retained. This makes sense because Si-O-C bonds

are easily hydrolyzed but not Si-C bonds. After 1 h thermal stability test in Ar flow, peaks of the vinyl groups at 1566 and 1456 cm^{-1} were slightly decreased, but still remained in the silica structure. After 1 h hydrothermal stability test with 16 mol% of steam exposure, the peaks at 1566 and 1456 cm^{-1} decreased, and this result indicates that some vinyl groups were removed by steam at the test conditions.

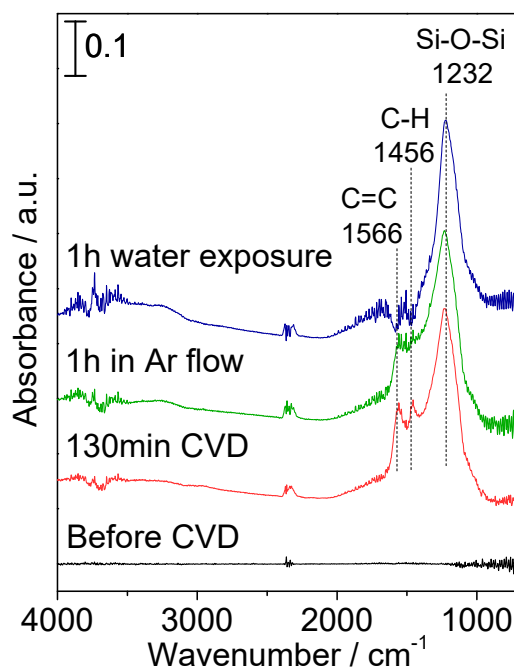


Figure 3.6. Infrared spectra of the calcined γ -alumina disk before and after CVD, after 1h exposure Ar and 1 h exposure 16 mol% water. All treatments and measurements were carried out at 873 K.

3.3.3. Hydrothermal stability of the VTES-derived membrane

Figure 3.7 shows the H_2 and N_2 permeance of the VTES-derived membrane (a) and the TEOS-derived membrane (b) as a function of exposure time to 16 mol% water vapor in Ar at 873 K. For the VTES-derived membrane, the H_2 permeance decreased to 57 %, and the N_2 permeance decreased to 45 % after 1 h exposure to 16 mol% water vapor.

which are slightly smaller levels of decrease than for TEOS-derived silica membranes [34,39]. However, the permeance curves are seen to be leveling off, which indicates that the membranes reach a point of hydrothermally stability. The H_2 permeance of the VTES-derived membrane was still above the order of $10^{-7} \text{ mol m}^{-2} \text{ s}^{-1} \text{ Pa}^{-1}$, which is the threshold level for practical applications [40]. In contrast, the N_2 permeance increased considerably with the exposure time, and as a consequence the H_2/N_2 selectivity of the membrane decreased to 40 during the test.

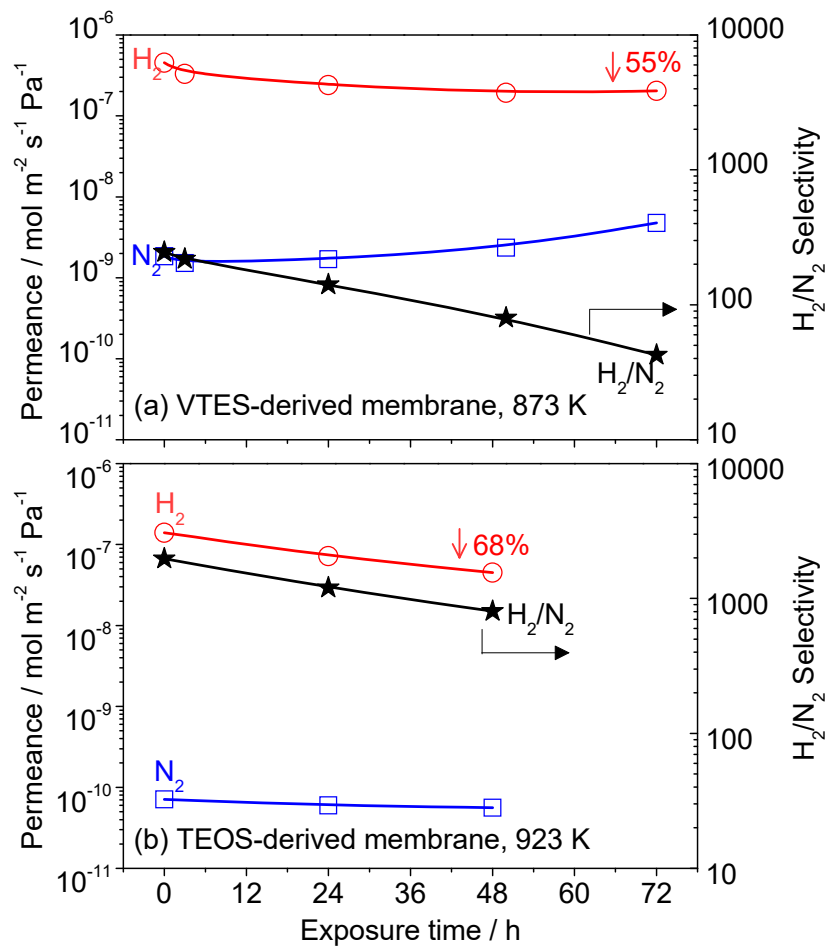


Figure 3.7. Changes in the H_2 and N_2 permeances of the VTES-derived silica membrane with exposure to 16 mol% of water vapor at 873 K for 72 h.

3.3.4. Permeation mechanism through the VTES-derived membrane before and after hydrothermal stability test

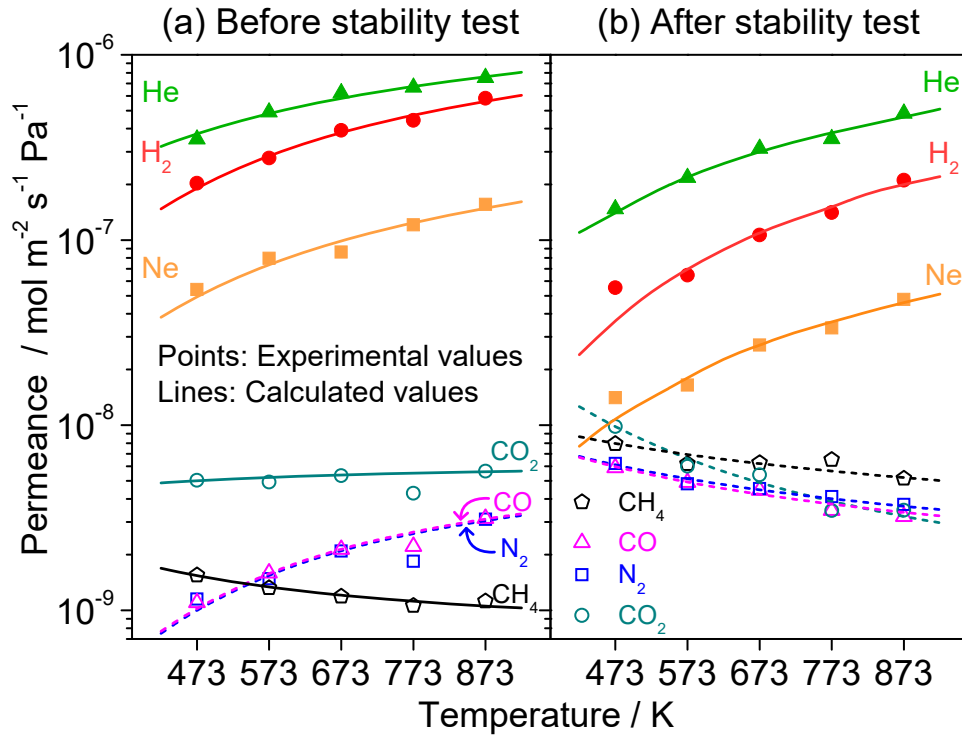


Figure 3.8. Temperature dependence of the permeances of various gases through the VTES-derived membrane before (a) and after (b) the hydrothermal stability test at 873 K with 16 mol% of water vapor

To investigate the permeation mechanism through the VTES-derived silica layer, permeance tests were conducted before and after the hydrothermal stability test with the pure gases He, Ne, H_2 , CO_2 , N_2 , CO and CH_4 at different temperatures in the range 473-823 K. The experimental temperature-dependent values of the permeance through the VTES-derived silica layer are shown in Figure 3.8 as points, which were obtained by subtracting the resistance of the γ -alumina intermediate layer (before CVD) from the resistance of the VTES-derived silica layer on the alumina substrate (after CVD):

$$\frac{1}{\bar{P}_{\text{VTES-derived silica layer}}} = \frac{1}{\bar{P}_{\text{afterCVD}}} - \frac{1}{\bar{P}_{\text{beforeCVD}}} \quad (3.3)$$

Figure 3.8 (a) shows the permeance of the various gases through the VTES-derived silica layer before the hydrothermal stability test. Smaller species such as He, Ne and H₂ had high permeance, while larger molecules like CO₂, N₂, CO and CH₄ had low permeance. The permeance of the smaller species increased with temperature, indicating an activated diffusion transport mechanism through the membrane. The permeance of the larger gases exhibited similar behavior as the smaller species, except that of CH₄ which decreased as temperature increased.

The permeance of the various gases was also tested after exposure to 16 mol% water vapor at 873 K for 72 h as shown in Figure 3.8 (b). The smaller gases followed a similar trend before and after the hydrothermal stability tests with the permeance increasing with temperature, but with the overall permeance declining. This was due the densification of silica which led to compaction of the silica structure, making it difficult for small gases to pass through the silica structure. The larger gases did not follow the same trend before and after the hydrothermal exposure. Overall, their permeance increased, probably because the densification of the silica structure also formed defect pores. Moreover, the pores became larger in size so that the mechanism of permeation changed, with the permeance of all large gases decreasing with temperature.

In order to quantitatively explain the mechanism of permeation the transport of various gases through the VTES-derived silica layer was measured and analyzed using a solid-state diffusion model for small gases and surface diffusion and gas-translation models for large gases. First the data for the small-sized gases will be discussed. The analysis was conducted using Eq. (3.4), derived earlier [14] using statistical mechanics. The equation has as parameters the number of solubility sites per m³ of membrane

volume (N_S), the vibrational frequency of the species in the passageways between the sorption sites (ν^*), the activation energy of diffusion (ΔE_a) and the jump distance (d).

$$\bar{P}_i = \frac{1}{6L} \left(\frac{d^2}{h} \right) \left(\frac{h^2}{2\pi m_i k T} \right)^{3/2} \left(\frac{\sigma h^2}{8\pi^2 I k T} \right)^\alpha \times \frac{(N_S/N_A)}{(e^{h\nu^*/2kT} - e^{-h\nu^*/2kT})^2} e^{-\Delta E_a/RT} \quad (3.4)$$

where \bar{P}_i is the permeance of species i through the VTES-derived silica layer [$\text{mol m}^{-2} \text{s}^{-1} \text{Pa}^{-1}$], L the thickness of the top permselective layer, m_i the mass of the species i , T the temperature [K], h Planck's constant, k Boltzmann's constant, N_A Avogadro's number, R the gas constant, I the moment of inertia, α an exponent accounting for incomplete loss of rotation (0 for He and Ne, and 0.2 for H_2), σ the symmetry factor of the species (2 for H_2). The membrane thickness was 200 nm as obtained from the SEM image in Figure 3.5 (b). Use was also made of the polynomial relationship previously found [14] between d and N_S as shown in Eq. (3.5):

$$d \text{ (nm)} = a + bN_S + cN_S^2 + dN_S^3 \quad (3.5)$$

where $a = 0.84649$, $b = -1.74523 \times 10^{-29}$, $c = 5.60055 \times 10^{-58}$, and $d = -7.66678 \times 10^{-87}$.

The calculated permeance is shown in Figure 3.8 as curves, and the fitted parameters are summarized in Table 3.1. Before discussing the values in detail it should be noted that the quantities obtained are physically realistic. The number of sites are of the order of 10^{27} m^{-3} and the inverse cube root is $1 \times 10^{-9} \text{ m}$ or 1 nm, which is of the order of the distance between solubility sites d . The vibrational frequency of 10^{12} s^{-1} corresponds to that expected for molecular vibrations and the activation energies of the order of 10 kJ mol^{-1} which is reported for passage of small gases through vitreous glasses [41,42].

Before and after the hydrothermal stability test, the number of solubility sites N_S are in the order $\text{He} > \text{Ne} > \text{H}_2$, which follows the species size. This result is understandable

since on average smaller molecules will fit into more solubility sites. The order of activation energy ΔE_a has an inverse relation with N_s because the larger molecules must overcome a larger barrier to squeeze through the silica-based rings. However, size is not the only factor that determines the permeance order. Another property that affects permeance is the jump frequency between sites and this has an inverse relationship with the mass of the species. This can be understood from consideration of the vibrational frequency of a harmonic oscillator, $\nu = \frac{1}{2\pi} \sqrt{\frac{k}{m}}$, which decreases as the reciprocal of the square root of the mass. As captured in Eq. (3.4), the permeance depends on both species size and mass, and gives rise to the order observed.

Table 3.1.

Calculated parameters for the VTES-derived membrane based on the solubility site model.

| Gas | N_s / site m^{-3} | ν^* / s^{-1} | ΔE_a / $kJ\ mol^{-1}$ | d / nm | Regression coefficient | |
|------------------------------------|--------------------------|------------------------|----------------------------------|-----------|---------------------------|-------|
| SiO ₂ (V) Before HTS | He | 0.475×10^{27} | 2.21×10^{12} | 3.4 | 0.8382 | 0.973 |
| | Ne | 0.391×10^{27} | 1.08×10^{12} | 6.8 | 0.8397 | 0.955 |
| | H ₂ | 0.335×10^{27} | 2.39×10^{12} | 7.3 | 0.8407 | 0.982 |
| SiO ₂ (V) After HTS | He | 0.885×10^{27} | 2.94×10^{12} | 7.3 | 0.8311 | 0.978 |
| | Ne | 0.665×10^{27} | 2.06×10^{12} | 9.6 | 0.8351 | 0.966 |
| | H ₂ | 0.396×10^{27} | 3.03×10^{12} | 12.5 | 0.8396 | 0.961 |

In comparison with the case before water exposure, the permeances of He, H₂ and Ne were lower after the steam treatment. The activation energies of the membrane after exposure water vapor were higher and the jump distances were smaller, resulting in a

larger number of solubility sites. This result indicates that the silica structure, which allows small species to permeate through, shrank after hydrothermal stability test due to densification caused by condensation of silanol groups (Si-OH). The mode of permeation here is the major contributor to transport as it involves the entire silica network through a solid-state jump mechanism not involving pores.

The large molecules are considered to permeate through a few small passageways in the silica-based layer with a surface flow process such as surface diffusion or gas-translation. From the experimental results, the permeances of CO₂ and CH₄ before the water exposure were fitted to a surface diffusion model using Eq. (3.6), and the calculated permeances are shown in Figure 3.8 (a) as lines. For the other gases, which are not condensable, the permeances were fitted to a gas-translational model using in Eq. (3.7) and the calculated permeances are shown in Figure 3.8 as dotted lines. The experimental data at 773 K show deviations (Figure 3.8) and were omitted from the calculations. The calculated parameters are summarized in Table 3.2 and 3.3.

Surface diffusion model:

$$\bar{P}_{SD} = P_0 \exp\left(\frac{-\Delta H_a - \Delta E_{SD}}{RT}\right) \quad (3.6)$$

where P_0 is a pre exponential factor, ΔH_a [J mol⁻¹] enthalpy of adsorption, ΔE_{SD} the energy barrier for moving to an adjacent adsorption site, and the others symbols are the same as above.

Gas-translational model:

$$\bar{P}_{GT} = \frac{C}{\sqrt{M_i RT}} \exp\left(-\frac{\Delta E_a}{RT}\right) \quad \text{where } C = \frac{\varepsilon d_p \rho_g}{\tau L} \sqrt{\frac{8}{\pi}} \quad (3.7)$$

where ε is the porosity, τ the tortuosity, d_p the pore size, ρ_g a pre-exponential factor, M_i the molecular weight of component i , and the others symbols are the same as above.

Table 3.2.

Calculated parameters for the VTES-derived membrane based on the surface diffusion model.

| | Gas | M / g mol ⁻¹ | Kinetic diameter / nm | P_0 / mol m ⁻² s ⁻¹ Pa ⁻¹ | $-\Delta H_a - \Delta E_{SD}$ / kJ mol ⁻¹ | Regression coefficient |
|-----------------------------|-----------------|------------------------------|-----------------------------|---|---|---------------------------|
| Before water exposure | CH ₄ | 16 | 0.38 | 7.2×10^{-10} | 2.9 | 0.9693 |
| | CO ₂ | 44 | 0.33 | 8.0×10^{-9} | -2.5 | 0.9491 |

Table 3.3.

Calculated parameters for the VTES-derived membrane based on the gas-translational model.

| | Gas | M / g mol ⁻¹ | C | ΔE_a / kJ mol ⁻¹ | Regression coefficient |
|-----------------------------|-----------------|------------------------------|----------------------|--|---------------------------|
| Before water exposure | CO | 28 | 2.5×10^{-7} | 12.4 | 0.9268 |
| | N ₂ | 28 | 3.2×10^{-7} | 14.5 | 0.9456 |
| After water exposure | CH ₄ | 16 | 4.9×10^{-8} | -1.0 | 0.9903 |
| | CO | 28 | 3.3×10^{-8} | -2.8 | 0.9409 |
| | N ₂ | 28 | 3.4×10^{-8} | -2.3 | 0.9911 |
| | CO ₂ | 44 | 2.5×10^{-8} | -6.3 | 0.9725 |

Before the water exposure in Figure 3.8 (a), the order of permeance was CO₂ > N₂ ≈ CO > CH₄ which follows the kinetic diameter of the molecules at high temperature, but the order was changed to CO₂ > CH₄ > N₂ ≈ CO at low temperature. This result

indicates that condensable gases such as CO₂ and CH₄ followed a surface diffusion mechanism, and N₂ and CO followed a gas-translational mechanism. Again it should be noted that these mechanisms are minority contributors to the permeance and involve a few connected pores that are defects in the silica structure.

After the water exposure in Figure 3.8 (b), the small pores were enlarged and the permeances of the large-sized gas species increased. These permeances decreased with increasing temperature, which can be well described by the gas-translational mechanism. This makes sense since as the pores grew in size their associated surface area decreased and surface diffusion became less important. The order of the permeance was CO₂ > CH₄ > N₂ ≈ CO at low temperature, but the order was changed to CH₄ > N₂ ≈ CO > CO₂ which follows inverse mass. This result indicates that the gas-translational mechanism transitions to a Knudsen-like behavior at high temperature as shown by the crossing of the permeation curves (Figure 3.8 (b)). This crossover in curves is not observed with pure silica membranes derived from TEOS [43] and indicates a structural difference between the two types of membranes. In the VTES-derived membrane those are likely to be the polarizable vinyl groups in the small defect pores, with the groups having strong interactions between CH₄ and CO₂ and leading to the surface diffusion mechanism.

3.4. Conclusions

Hydrogen selective VTES-derived silica membranes were successfully prepared on a macroporous alumina support with pore size 60 nm by chemical vapor deposition (CVD) of pure vinyltriethoxysilane (VTES) at 873 K. The membrane had a high H₂ permeance of $5.4 \times 10^{-7} \text{ mol m}^{-2} \text{ s}^{-1} \text{ Pa}^{-1}$ with selectivities over CO₂, N₂, CO and CH₄ of

95, 170, 170 and 480, respectively. The thickness of this membrane was around 200 nm as measured by scanning electron microscopy (SEM). Analysis by Fourier transform infrared spectroscopy demonstrated that vinyl groups were retained in the silica network after CVD, but not ethoxy groups. Results of permeation tests of He, H₂, and Ne as a function of temperature were well described by a solid-state permeation mechanism involving jumps between solubility sites. The fitting parameters were physically realistic, and described the results quantitatively.

The hydrothermal stability of the membrane was studied by exposure to 16 mol% water vapor at 872 K for 72 h. The H₂ permeance (major path way: solid-state diffusion through the silica-) decreased 57 %, which was less than the 68 % reduction observed for a pure silica membrane. However the N₂ permeance (major path way: gas-translation through small defect pores) increased considerably with exposure time, and resulted in a decrease of the H₂/N₂ selectivity to 40. The temperature dependence of the permeance of various molecules before and after hydrothermal exposure gave information about the mechanism of transport. For large species the mechanism changed from surface diffusion to gas-translation. Overall the silica-based structure shrunk, while small-pore defects grew after with vapor exposure.

Reference

-
- [1] P. Li, Z. Wang, Z. Qiao, Y. Liu, X. Cao, W. Li, J. Wang, S. Wang, Recent developments in membranes for efficient hydrogen purification, *J. Membr. Sci.* 495 (2015) 130-168.
 - [2] D.S. Sholl, R.P. Lively, Seven chemical separations to change the world, *Nature* 532 (2016) 435-437.
 - [3] F. Gallucci, E. Fernandez, P. Corengia, M.V. Annaland, Recent advances on

-
- membranes and membrane reactors for hydrogen production, *Chem. Eng. Sci.* 92 (2013) 40-66.
- [4] T. Okubo, H. Inoue, Introduction of specific gas selectivity to porous glass membranes by treatment with tetraethoxysilane, *J. Membr. Sci.* 42 (1989) 109-117.
- [5] G.R. Gavalas, C.E. Megiris, S.W. Nam, Deposition of H₂ permselective SiO₂ films, *Chem. Eng. Sci.* 44 (1989) 1829-1835.
- [6] R.S.A. Delange, J.H.A. Hekkink, K. Keizer, A.J. Burggraaf, Formation and characterization of supported microporous ceramic membranes prepared by sol-gel modification techniques, *J. Membr. Sci.* 99 (1995) 57-75.
- [7] R.M. de Vos, H. Verweij, High-selectivity, high-flux silica membranes for gas separation, *Science* 279 (1998) 1710-1711.
- [8] T. Tsuru, Nano/subnano-tuning of porous ceramic membranes for molecular separation, *J. Sol-Gel Sci. Technol.* 46 (2008) 349-361.
- [9] M. Asaeda, S. Yamasaki, Separation of inorganic/organic gas mixtures by porous silica membranes. *Sep. Purif. Technol.* 25 (2001) 151-159.
- [10] Y. Gu, P. Hacırlıoğlu, S.T. Oyama, Hydrothermally stable silica-alumina composite membranes for hydrogen separation, *J. Membr. Sci.* 310 (2008) 28-37.
- [11] S.S. Kim, B.K. Seo, Gas permeation characteristics of silica/alumina composite membrane prepared by chemical vapor deposition, *Korean J. Chem. Eng.* 18 (2001) 322-329.
- [12] S. Gopalakrishnan, Y. Yoshino, M. Nomura, B.N. Nair, S.I. Nakao, A hybrid processing method for high performance hydrogen-selective silica membranes, *J. Membr. Sci.* 297 (2007) 5-9.
- [13] S.-I. Nakao, T. Suzuki, T. Sugawara, T. Tsuru, S. Kimura, Preparation of microporous membranes by TEOS/O₃ CVD in the opposing reactants geometry. *Microp. Mesop. Materials* 37 (2000) 145-152.
- [14] S.T. Oyama, D. Lee, P. Hacırlıoğlu, R.F. Saraf, Theory of hydrogen permeability in nonporous silica membranes, *J. Membr. Sci.* 244 (2004) 45-53.
- [15] Y. Gu, S.T. Oyama, High molecular permeance in a poreless ceramic membrane, *Adv. Mater.* 19 (2007) 1636-1640.
- [16] T. Tsuru, H. Shintani, T. Yoshioka, M. Asaeda, A bimodal catalytic membrane

-
- having a hydrogen-permselective silica layer on a bimodal catalytic support: Preparation and application to the steam reforming of methane, *Appl. Catal. A: Gen.* 302 (2006) 78-85.
- [17] S.T. Oyama, P. Hacırlıoğlu, Y. Gu, D. Lee, Dry reforming of methane has no future for hydrogen production: Comparison with steam reforming at high pressure in standard and membrane reactors, *Int. J. Hydrogen Energy* 37 (2012) 10444-10450.
- [18] H.M. van Veen, Y.C. van Delft, C.W.R. Engelen, P.P.A.C. Pex, Dewatering of organics by pervaporation with silica membranes, *Sep. Purif. Technol.* 22-23 (2001) 361-366.
- [19] M. Asaeda, J. Yang, Y. Sakou, Porous silica-zirconia (50%) membranes for pervaporation of iso-propyl alcohol (IPA)/water mixtures, *J. Chem. Eng. Jpn.* 35 (2002) 365-371.
- [20] I. Agirre, P.L. Arias, H.L. Castricum, M. Creatore, J.E. ten Elshof, G.G. Paradis, P.H.T. Ngamou, H.M. van Veen, J.F. Vente, Hybrid organosilica membranes and processes: Status and outlook, *Sep. Purif. Technol.* 121 (2014) 2-12.
- [21] R.M. de Vos, W.F. Maier, H. Verweij, Hydrophobic silica membranes for gas separation, *J. Membr. Sci.* 158 (1999) 277-288.
- [22] H.L. Castricum, A. Sah, R. Kreiter, D.H.A. Blank, J.F. Vente, J.E. ten Elshof, Hybrid ceramic nanosieves: stabilizing nanopores with organic links, *Chem. Commun.* (2008) 1103-1105.
- [23] J. Campaniello, C.W.R. Engelen, W.G. Haije, P.P.A.C. Pex, J.F. Vente, Long-term pervaporation performance of microporous methylated silica membranes, *Chem. Commun.* (2004) 834-835.
- [24] N.K. Raman, C.J. Brinker, Organic "template" approach to molecular sieving silica membranes, *J. Membr. Sci.* 105 (1995) 273-279.
- [25] M. Kanezashi, K. Yada, T. Yoshioka, T. Tsuru, Organic-inorganic hybrid silica membranes with controlled silica network size: Preparation and gas permeation characteristics, *J. Membr. Sci.* 348 (2010) 310-318.
- [26] M. Kanezashi, M. Kawano, T. Yoshioka, T. Tsuru, Organic-inorganic hybrid silica membranes with controlled silica network size for propylene/propane separation,

Ind. Eng. Chem. Res. 51 (2012) 944-953.

- [27] H.R. Lee, M. Kanezashi, Y. Shimomura, T. Yoshioka, T. Tsuru, Evaluation and fabrication of pore-size-tuned silica membranes with tetraethoxydimethyl disiloxane for gas separation, *AIChE J.* 57 (2011) 2755-2765.
- [28] H.R. Lee, T. Shibata, M. Kanezashi, T. Mizumo, J. Ohshita, T. Tsuru, Pore-size-controlled silica membranes with disiloxane alkoxides for gas separation, *J. Membr. Sci.* 383 (2011) 152-158.
- [29] K. Kusakabe, S. Sakamoto, T. Saie, S. Morooka, Pore structure of silica membranes formed by a sol-gel technique using tetraethoxysilane and alkyltriethoxysilanes, *Sep. Purif. Technol.* 16 (1999) 139-146.
- [30] M. Nomura, K. Ono, S. Gopalakrishnan, T. Sugawara, S.-I. Nakao, Preparation of a stable silica membrane by a counter diffusion chemical vapor deposition method, *J. Membr. Sci.* 251 (2005) 151-158.
- [31] M. Nomura, T. Nagayo, K. Monma, Pore size control of a molecular sieve silica membrane prepared by a counter diffusion CVD method, *J. Chem. Eng. Jpn.* 40 (2007) 1235-1241.
- [32] Y. Ohta, K. Akamatsu, T. Sugawara, A. Nakao, A. Miyoshi, S. Nakao, Development of pore size-controlled silica membranes for gas separation by chemical vapor deposition, *J. Membr. Sci.* 315 (2008) 93-99.
- [33] X.-L. Zhang, H. Yamada, T. Saito, T. Kai, K. Murakami, M. Nakashima, J. Ohshita, K. Akamatsu, S. Nakao, Development of hydrogen-selective triphenylmethoxysilane-derived silica membranes with tailored pore size by chemical vapor deposition, *J. Membr. Sci.* 499 (2016) 28-35.
- [34] S.-J. Ahn, A. Takagaki, T. Sugawara, R. Kikuchi, S.T. Oyama, Permeation properties of silica-zirconia composite membranes supported on porous alumina substrates, *J. Membr. Sci.* 526 (2017) 409-416.
- [35] Y. Gu, S.T. Oyama, Ultrathin, hydrogen-selective silica membranes deposited on alumina-graded structures prepared from size-controlled boehmite sols, *J. Membr. Sci.* 306 (2007) 216-227.
- [36] S. T. Oyama, H. Lim, An operability level coefficient (OLC) as a useful tool for correlating the performance of membrane reactors, *Chem. Eng. J.* 151 (2009)

351–358.

- [37] Y.-S. Li, P.B. Wright, R. Puritt, T. Tran, Vibrational spectroscopic studies of vinyltriethoxysilane sol-gel and its coating, *Spectrochim. Acta, Part A* 60 (2004) 2759-2766.
- [38] R. Al-Oweini, H. El-Rassy, Synthesis and characterization by FTIR spectroscopy of silica aerogels prepared using several $\text{Si}(\text{OR})_4$ and $\text{R}^n\text{Si}(\text{OR}')_3$ precursors, *J. Mol. Struct.* 919 (2009) 140-145.
- [39] Y. Gu, S.T. Oyama, Permeation properties and hydrothermal stability of silica-titanic membranes supported on porous alumina substrates, *J. Membr. Sci.* 345 (2009) 267-275.
- [40] H. Lim, Y.F. Gu, S.T. Oyama, Studies of the effect of pressure and hydrogen permeance on the ethanol steam reforming reaction with palladium- and silica-based membranes, *J. Membr. Sci.* 396 (2012) 119-127.
- [41] P. Hacırlıoğlu, D. Lee, G.V. Gibbs, S.T. Oyama, Activation energies for permeation of He and H_2 through silica membranes: An ab initio calculation study, *J. Membr. Sci.* 313 (2008) 277-283.
- [42] D. Lee, S.T. Oyama, Gas permeation characteristics of a hydrogen selective supported silica membrane, *J. Membr. Sci.* 210 (2022) 291-306.
- [43] S.T. Oyama, M. Yamada, T. Sugawara, A. Takagaki, T. Kikuchi, Review on mechanism of gas permeation through inorganic membranes, *J. Jpn. Petrol. Inst.* 54 (2011) 298-309.

Chapter 4

Dehydrogenation of Ethane over Cr/ZSM-5 Catalyst in a Hydrogen Selective Silica Membrane Reactor

4.1. Introduction

Ethylene is one of the most important petrochemicals due to its extensive use as feedstock for the production of a vast array of chemicals, including polymers (e.g., polyethylene, polyester, and polystyrene), oxygenates (e.g., ethylene oxide, ethylene glycol, and acetaldehyde), and chemical intermediates (e.g., ethyl benzene and ethylene dichloride) [1]. The current worldwide production of ethylene amounts to 160 million tons per year [2]. Ethylene is commercially produced by steam cracking and fluid catalytic cracking of naphtha, light diesel, and other oil byproducts, but these processes require high-energy and are not selective, producing substantial quantities of methane and coke as byproducts.

Catalytic dehydrogenation of ethane provides an alternative for producing ethylene with hydrogen as a byproduct, an important reagent in refineries. One of the drawbacks of catalytic dehydrogenation of ethane is the thermodynamic constraint in the ethane conversion. To alleviate this problem, membrane reactors are considered possible solutions because they can overcome the equilibrium limitation of the reaction by extracting H_2 continuously from the catalyst bed [3,4]. There have been a number of studies of alkane dehydrogenation. Gobina et al. reported ethane dehydrogenation over 0.5 wt% Pd/Al₂O₃ in a membrane reactor incorporating a hydrogen selective Pd-Ag

membrane at 660 K and 129 kPa [5]. They also developed a two-dimensional mathematical model to describe the performance of the membrane reactor [6]. Avila et al. studied ethane dehydrogenation over 1 wt% Pt-Sn/Al₂O₃ in a membrane reactor with a hydrogen selective natural mordenite membrane disk using pure ethane at 773-823 K and 0.1 MPa [4]. Collins et al. reported propane dehydrogenation over Pd-based catalyst in membrane reactor with microporous silica-based membranes and a palladium membrane at 773-848 K and 0.1 MPa [7]. Medrano et al. studied propane dehydrogenation over a Pt-Sn/MgAl₂O₄ catalyst in a Pd-Ag membrane coupled to two-zone fluidized bed reactor with different reactor configurations at 848 K and 0.1 MPa [8]. The propylene yield in reactor with membrane was higher than other reactor configurations. Previous studies mainly focused on Pd-based or Pt-based catalyst with Pd-based membrane, and there has been limited previous work using Cr-based catalyst and hydrogen selective silica-based membrane on the dehydrogenation of ethane in membrane reactors. Especially, there is very limited studies considered pressure effect on catalytic membrane reactors for ethane dehydrogenation.

In this study the dehydrogenation of ethane was conducted over a 5 wt% Cr/ZSM-5 catalyst coupled to a H₂ selective silica membrane. Various reaction conditions were varied such as feed flow rates (20-100 cm³ min⁻¹), total pressures (0.1-0.5 MPa) and temperatures (723-823 K) and were applied to packed bed reactor (PBR) and membrane reactor (MR) modes of operation. A general parameter, the operability level coefficient (OLC), the ratio between the actual permeation rate and the actual formation rate of a H₂ in a membrane reactor, was used to correlate the performance of the membrane reactor.

4.2. Experimental

4.2.1. Preparation and characterization of the silica membrane

The silica membranes used in this work were prepared as described before [9]. First a γ -alumina intermediate layer was prepared on a tubular macroporous α -alumina support by a sol-gel method. Then a silica layer was placed on top of the γ -alumina intermediate layer by a chemical vapor deposition (CVD) method. The CVD was conducted using vinyltriethoxysilane (VTES, TCI, 98 %) as the silica precursor at 873 K and 0.1 MPa with the VTES bubbler at room temperature. The CVD was conducted until an adequate H_2 permeance and H_2/N_2 selectivity were obtained by interrupting the CVD and checking the performance of the membrane periodically. After CVD, the permeances of various gases such as He, Ne, H_2 , CO_2 , N_2 , CH_4 , C_2H_6 and C_2H_4 were measured at 573 K and 0.25 MPa. A low temperature of 573 K was chosen for the permeance measured in order to avoid reaction of ethane and decomposition of ethylene.

4.2.2. Preparation and characterization of Cr/ZSM-5 catalyst

A 5 wt% Cr/ZSM-5 was synthesized by the incipient wetness impregnation method. The 4 g of ZSM-5 ($SiO_2/Al_2O_3 = 1900$, Tosoh) support was impregnated with an aqueous solution of chromium (III) nitrate, which was prepared by stirring 1.55 g of chromium (III) nitrate nonahydrate (Alfa Aesar, 98.5 %) with 3 ml of deionized water for 10 min at room temperature, followed by drying at 393 K overnight and calcination at 1023 K for 5 h. The powder precursor was pelletized and sieved to particles of 650-1180 μm diameter.

The calcined catalyst was characterized by X-ray diffraction (Rigaku RINT 2400) using $CuK\alpha$ radiation ($\lambda=1.5418\text{\AA}$) at 40 kV and 100 mA. The sample was scanned

from 2θ values of 10° to 80° with a step size of 0.02° and a dwell time of 1.0 s.

The specific surface area of the samples was calculated from the linear portion of BET plots ($P/P_0 = 0.01 - 0.20$) obtained from N_2 adsorption isotherms at 77 K using a BELSORP mini II micropore size analyzer. Prior to the measurements, the sample was dried and evacuated at 393 K overnight.

The X-ray absorption fine structure (XAFS) spectra were measured at the BL-9C beam line of the Photon Factory (PF) in the Institute of Materials Structure Science, High-Energy Accelerator Research Organization (KEK-IMSS-PF). The synchrotron ring was operated at 2.5 GeV with 450 mA of ring current. The Cr K-edge absorption spectra were recorded in transmission mode using ionization chambers for the detection of the incident X-ray beam (I0, 70% He in N_2) and transmitted beam (IT, 15% Ar in N_2). The calcined disk sample (20 mg) was set in the middle of an in situ cell equipped with Kapton windows, and treated at 823 K for 1 h under a He flow in the same manner as for the activity tests. The EXAFS data were analyzed by REX software (Rigaku, Tokyo, Japan). Phase shift and amplitude functions of Cr were calculated by FEFF8.

4.2.3. Reactivity test with catalytic membrane reactor

A schematic diagram of the catalytic membrane reactor is shown in Figure 4.1. Reactions were carried out in a quartz up-flow tubular reactor (O.D.= 16 mm, I.D.= 14 mm, length = 250) equipped with a hydrogen selective VTES-derived silica membrane, which had a H_2 permeance of $2.7 \times 10^{-7} \text{ mol m}^{-2} \text{ s}^{-1} \text{ Pa}^{-1}$ with H_2/C_2H_6 selectivity of 250 at 573 K and 0.25 MPa. Prior to testing, 0.4 g of 5 wt% Cr/ZSM-5 was heated at 1.5 K min^{-1} to 823 K in Ar flow and maintained for 2 h. In order to reach the steady-state of reaction, 20 % C_2H_6 diluted in Ar was fed into the reactor at a flow rate of $20 \text{ cm}^3 \text{ min}^{-1}$

at 823 K for 2 h. After the reaction stabilized, various feed flow rates ($20\text{-}100\text{ cm}^3\text{ min}^{-1}$), total pressures ($0.1\text{-}0.5\text{ MPa}$) and reaction temperatures ($723\text{-}823\text{ K}$) were applied for both conventional and membrane reactor modes. The tests were applied consecutively with first 30 min of packed bed reactor (PBR) operation followed by 30 min of membrane reactor (MR) operation. The system was switched between MR and PBR modes by turning the sweep gas on and off. Separate studies showed that the permeance of H_2 dropped to zero when the sweep gas was turned off. In this study the flow rate of sweep gas (Ar) was $100\text{ cm}^3\text{ min}^{-1}$.

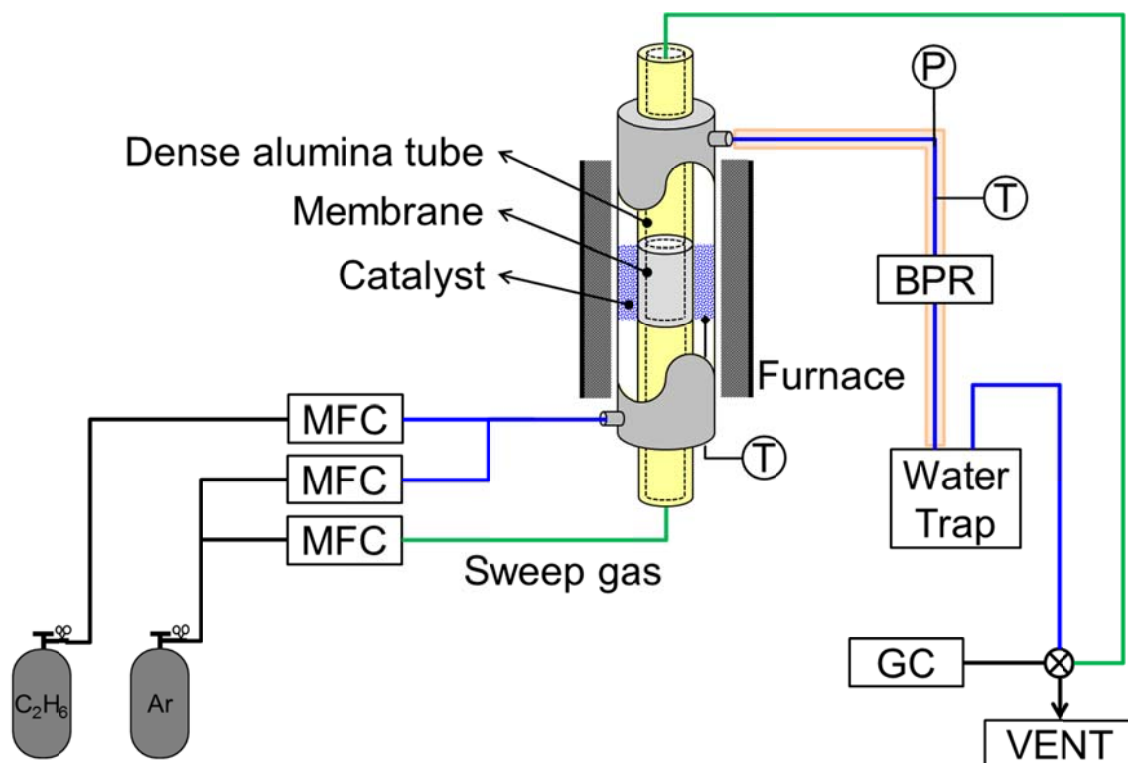


Figure 4.1. Schematic of catalytic membrane reactor for ethane dehydrogenation

The conversion, yield, H₂ permeance and productivity were calculated according to the following equations:

$$\text{Conversion (C}_2\text{H}_6) = \frac{F_{\text{C}_2\text{H}_6}^{\text{in}} - F_{\text{C}_2\text{H}_6}^{\text{out}}}{F_{\text{C}_2\text{H}_6}^{\text{in}}} \times 100 \text{ [\%]} \quad (4.1)$$

$$\text{Yield (j)} = \frac{F_j^{\text{out}}}{F_{\text{C}_2\text{H}_6}^{\text{in}}} \times 100 \text{ [\%]} \quad (4.2)$$

$$\text{Permeance (H}_2) = \frac{F_{\text{Permeated H}_2}}{A \Delta P_{\text{H}_2}} \text{ [mol m}^{-2}\text{s}^{-1}\text{Pa}^{-1}] \quad (4.3)$$

$$\text{Productivity (H}_2) = \frac{F_{\text{produced H}_2}}{\text{Weight of catalyst}} \text{ [mol s}^{-1}\text{g}^{-1}] \quad (4.4)$$

where F_i is the molar flow rate of the gas i [mol s⁻¹], A is the surface area of the membrane [m²] and ΔP_{H_2} is the partial pressure difference of H₂ between the inner and outer side of the membrane tube [Pa].

The ethylene yield enhancement was defined from quantities obtained experimentally in the MR and PBR.

$$\text{Ethylene yield enhancement (\%)} = \frac{\text{ethylene yield(MR)} - \text{ethylene yield(PBR)}}{\text{ethylene yield(PBR)}} \quad (4.5)$$

The operability level coefficient (OLC) is defined as the ratio of the actual permeation rate and the actual formation rate of a critical product in a membrane reactor (Eq.4.6) [10]. The critical product is usually the one for which the membrane is permselective, in this case hydrogen. The product formation rate is the total production rate, including that which permeates.

$$\text{OLC} = \frac{\text{product permeation rate}}{\text{product formation rate}} = \frac{\text{molar flow rate of permeated H}_2}{\text{molar flow rate of produced H}_2} \quad (4.6)$$

4.2.4. Modeling of ethane dehydrogenation in a membrane reactor

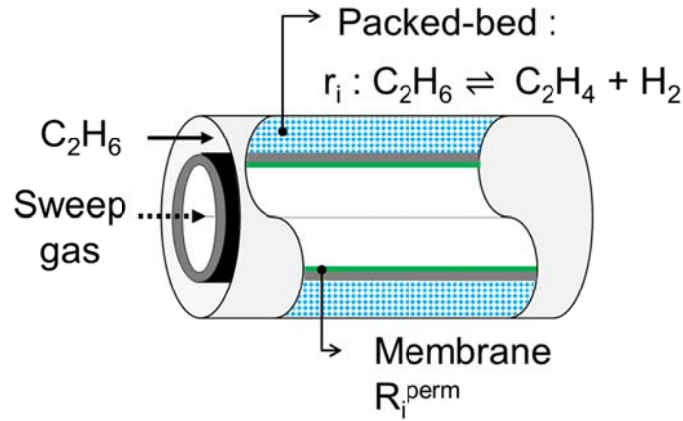


Figure 4.2. Schematic reaction model for simulations

Figure 4.2 showed the schematic reaction system model used for the simulation of the membrane reactor. The one-dimensional modeling of the membrane reactor was used for the simulation with the following assumptions: (1) Steady-state in both the reaction and permeation sides, (2) isothermal condition, (3) radially isobaric.

The mass balance of the species in the reaction and permeation sides was described in Table 4.1.

Table 4.1.

Model equations for the one-dimensional model

| Reaction side | Permeation side |
|--------------------------------------|---|
| $\frac{dF_i}{dw} = r_i - R_i^{perm}$ | $\frac{dF_i}{dw} = R_i^{perm}$ |
| | where $R_i^{perm} = k'_c a (C_i^{reaction\ side} - C_i^{permeate\ side})$ |

The kinetic rate expression for the ethane dehydrogenation and parameters used in the simulation were summarized in Table 4.2. The calculations were conducted by using Polymath program.

Table 4.2

Reaction rate expression and kinetic parameters for ethane dehydrogenation

| | |
|--------------------------------|---|
| Reaction rate, r_i | $-r_{C_2H_6} = r_{C_2H_4} = r_{H_2} = k \left(C_{C_2H_6} - \frac{C_{C_2H_4} C_{H_2}}{K_e} \right)$ |
| Reaction rate constant, k | 0.0225 s ⁻¹ (calculated based on Power Law) |
| Equilibrium constant, K_e | 0.0003 at 823 K and 0.1MPa |
| Total concentration, C_{tot} | 0.0148 mol dm ⁻³ |

4.3. Results and discussion

4.3.1. Permeance of VTES-derived silica membrane

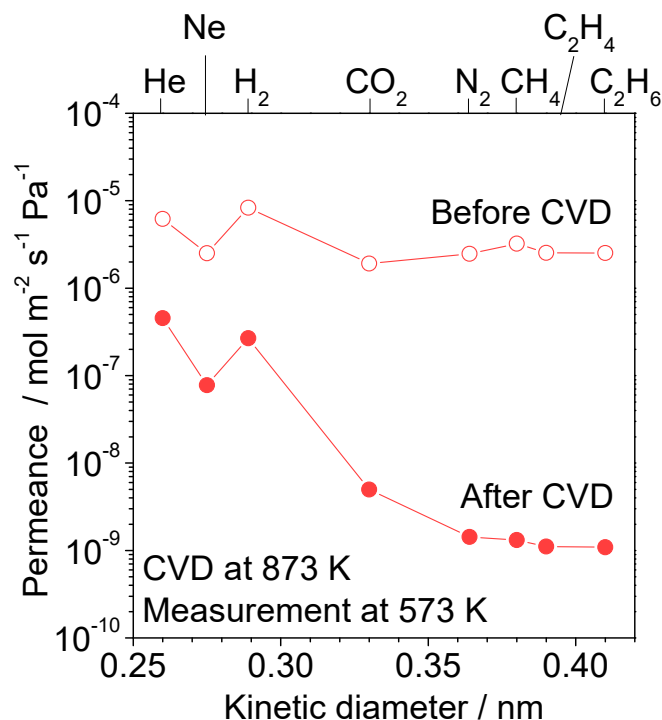


Figure 4.3. Permeance of various gases before and after CVD (CVD temperature: 873 K, measurement temperature: 573 K)

Figure 4.3 shows the permeance of various gases (He, Ne, H₂, CO₂, N₂, CH₄, C₂H₄, C₂H₆) through the alumina multilayers (before CVD) and VTES-derived silica membrane (after CVD) as a function of kinetic diameter of the species. The CVD was conducted at 873 K and 0.1 MPa, and the permeance measurements were conducted at 573 K and 0.25 MPa. Before CVD, all gases showed high permeance in the range of 10^{-6} $\text{mol m}^{-2} \text{s}^{-1} \text{Pa}^{-1}$, and the order of permeances followed inverse of their mass ($\text{H}_2 > \text{He} > \text{CH}_4 > \text{C}_2\text{H}_4 > \text{C}_2\text{H}_6 > \text{Ne} > \text{N}_2 > \text{CO}_2$). After 130 min of CVD, the permeance of all gases decreased, and the order of permeances generally followed their size. This indicated a transition from Knudsen diffusion to molecular sieving. The permeance of

H_2 was $2.7 \times 10^{-7} \text{ mol m}^{-2} \text{ s}^{-1} \text{ Pa}^{-1}$ and the selectivity of H_2/C_2H_6 was 250 and H_2/C_2H_4 was 240 at 573 K. These values were considered to be high enough for successful application in a catalytic membrane reactor [11]. The exact permeance of H_2 at the reaction conditions will be discussed in section 4.3.3.

4.3.2. Characterization of catalyst

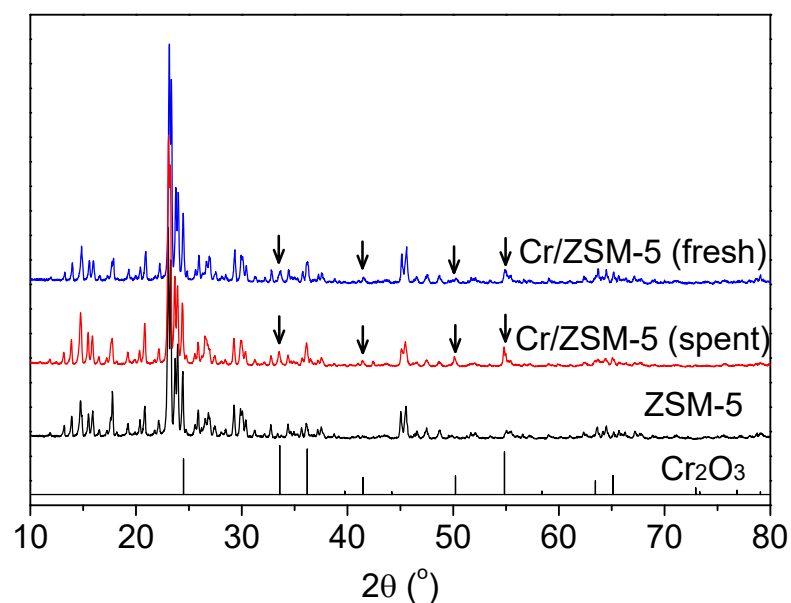


Figure 4.4. XRD patterns of ZSM-5 support, fresh and spent Cr/ZSM-5 catalysts

Figure 4.4 shows the XRD patterns of the ZSM-5 support, and the fresh and spent 5 wt% Cr/ZSM-5 catalysts. All samples exhibit diffraction peaks that are typical for crystalline ZSM-5. The XRD pattern of fresh Cr/ZSM-5 catalyst clearly shows additional small peaks at $2\theta = 34^{\circ}$, 42° , 51° , and 56° , which is attributed to Cr_2O_3 (PDF#38-1479). Those peaks remained in the XRD pattern of the spent Cr/ZSM-5 catalyst, indicating that the catalyst was stable during reaction. However, it cannot be ruled out that Cr_2O_3 was a spectator species.

Table 4.3.

BET surface areas, pore volumes and crystallite size of the ZSM-5 support, and the fresh and spent Cr/ZSM-5 catalyst samples

| Sample | Condition | $S_{\text{BET}} / \text{m}^2 \text{g}^{-1}$ | $V_{\text{Pore}} / \text{cm}^3 \text{g}^{-1}$ | Crystallite size / nm |
|----------|-------------|---|---|-----------------------|
| ZSM-5 | As received | 339 | 0.171 | - |
| Cr/ZSM-5 | Fresh | 279 | 0.144 | 29 |
| | Spent | 260 | 0.131 | 35 |

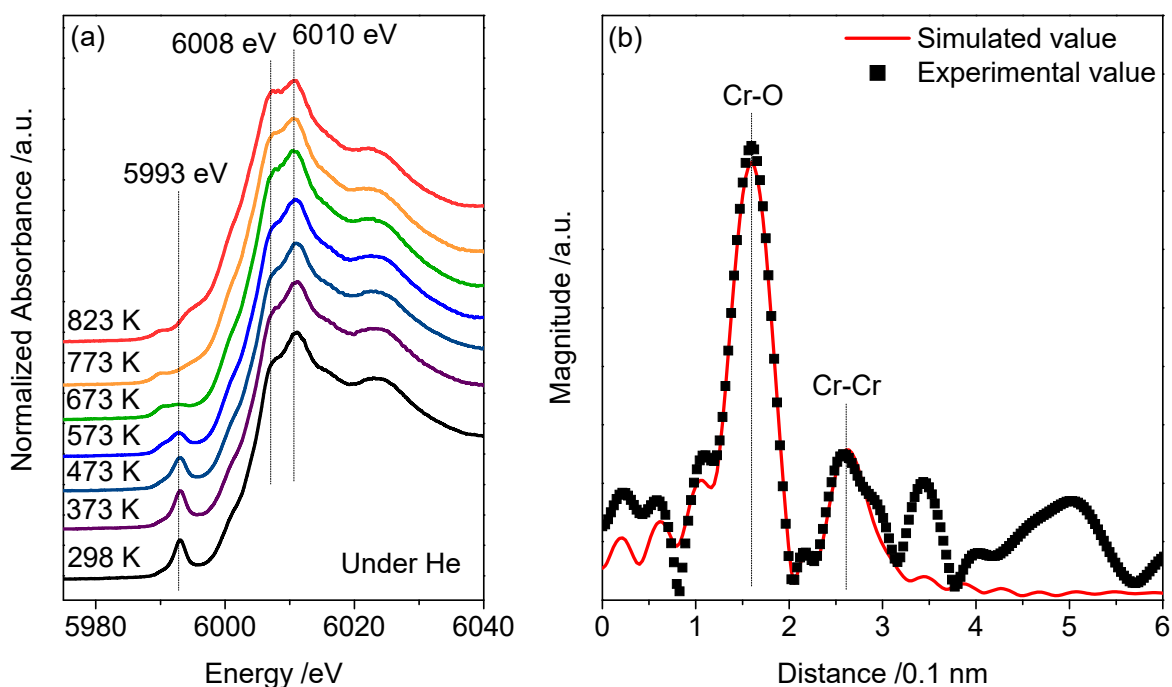


Figure 4.5. (a) XANES spectra of the Cr/ZSM-5 catalyst after He treatment at 298-823 K and (b) EXAFS spectra after He treatment at 823 K. Spectra were taken at room temperature.

The surface areas and pore volumes of the support, the fresh and spent catalysts are also presented in Table.4.3. After loading the chromium metal, the surface area

decreased with a reduction in pore volume due to the presence of Cr₂O₃ phase on the support.

Table 4.4.

Curve-fitting results for Cr/ZSM-5 catalyst after pretreatment at 823 K

| | N | R | dE | DW | R |
|-------|-------|-------|-------|-------|-------|
| Cr-O | 5.993 | 1.987 | 0.291 | 0.067 | 1.305 |
| Cr-Cr | 3.221 | 2.971 | 3.163 | 0.099 | |

Figure 4.5 (a) shows the X-ray absorption near edge spectroscopy (XANES) results of the Cr/ZSM-5 catalyst during He treatment at 298-823 K. These temperatures were the same as those used in the pretreatment step before reactivity measurements, and can give evidence for the state of Cr species. The spectrum at 298 K displayed a small pre-edge peak at 5993 eV corresponding to a terminal Cr⁶⁺=O species with tetrahedral structure [12]. Interestingly, as temperature increased in He flow, the intensity of the pre-edge gradually decreased. The shape of the XANES spectra changed slightly with a peak at 6008 eV increasing and a peak at 6010 eV decreasing. After the thermal treatment the overall shape of the spectrum was similar to that of a reference Cr₂O₃ spectrum as reported in previous work [13]. Figure 4.5 (b) shows the extended X-ray absorption fine-structure (EXAFS) of the Cr/ZSM-5 catalyst at 823 K and a calculated curve of Cr₂O₃, with the results of curve-fitting of the spectrum summarized in Table 4.4. Only two paths were used (Cr-O at ~ 0.1987 nm and Cr-Cr at ~ 0.297 nm) but good fits were obtained. There were two main peaks in the Fourier transforms located at 0.1987 nm for a Cr-O distance and 0.297 nm for a Cr-Cr distance. The coordination number was 6 for Cr-O and 3.2 for Cr-Cr. These values are similar to those of a Cr₂O₃

reference sample suggesting that after pretreatment in He at 823 K, the Cr_2O_3 phase was fully formed. The phase is known to be effective for alkene dehydrogenation [14].

4.3.3. Catalytic performance of 5 wt% Cr/ZSM-5 in the dehydrogenation of ethane

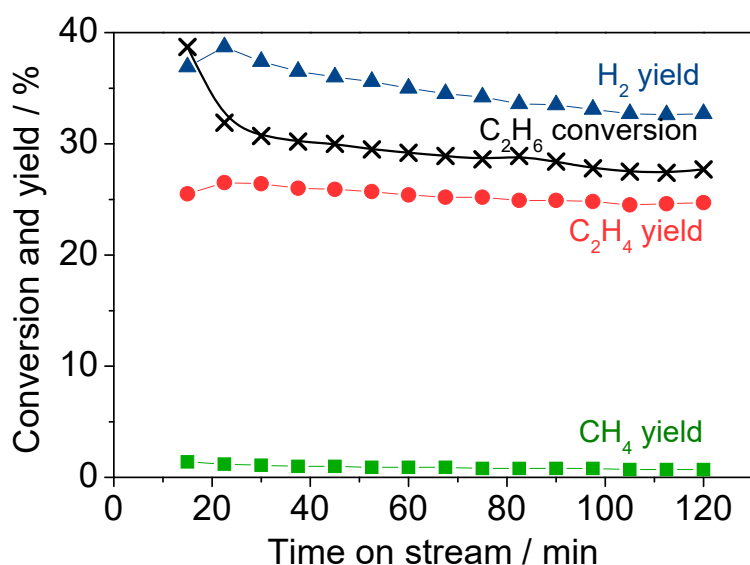


Figure 4.6. Conversion of C_2H_6 and yields of C_2H_4 , H_2 and CH_4 as a function of time for the dehydrogenation of ethane in the PBR with $20 \text{ cm}^3 \text{ min}^{-1}$ of 20% C_2H_6 diluted in Ar at 823 K and 0.1 MPa.

Ethane dehydrogenation over the 5 wt% Cr/ZSM-5 catalyst was carried out at 823 K and 0.1 MPa with $20 \text{ cm}^3 \text{ min}^{-1}$ of 20 % ethane diluted in Ar and was allowed to run for 2 h to stabilize the catalyst. Figure 4.6 shows the conversion of C_2H_6 and yields of products such as C_2H_4 , H_2 and CH_4 as a function of time on stream. The catalyst exhibited a rapid loss in conversion during the first 30 min of time on stream, but attained almost constant conversion and yield during the test period. After 2 h of reaction the C_2H_6 conversion was stabilized to 28 % and the ethylene selectivity was 88 %. Theoretically the H_2 yield should be the same as the C_2H_4 yield, but the H_2 yield

was higher than the C₂H₄ yield. This is because of a side reaction where absorbed C₂H₄ on catalyst was decomposed to produce CH₄, H₂ and coke [15,16].

4.3.4. Effect of feed flow rate on ethane dehydrogenation in the PBR and MR

The effect of various reaction was studied over the 5 wt. % Cr/ZSM-5 catalyst in the PBR and the MR. Figure 4.7 (a, b) show the conversion of C₂H₆ and yields of C₂H₄, H₂ and CH₄ with various feed flow rates in the PBR and the MR at 823 K and 0.1 MPa. In the PBR (Figure 4.7 (a)), the C₂H₆ conversion decreased with increasing feed flow rate from 28 % for 20 cm³ min⁻¹ to 10 % for 100 cm³ min⁻¹ due to the lower contact time of ethane on the catalyst. However, the selectivity of C₂H₄ increased slightly with decreasing CH₄ yield with increasing feed flow rate from 89 % for 20 cm³ min⁻¹ to 92 % for 100 cm³ min⁻¹ because of the decrease in side reactions such as coking and cracking.

In the MR (Figure 4.7 (b)), the trends of the conversion of C₂H₆ and yields of C₂H₄ and H₂ were the same as in the PBR, but the values were higher in the MR than in the PBR. The enhancement of the C₂H₄ yield in the MR, which is defined as the difference between the C₂H₄ yield in the MR and the PBR divided by the C₂H₄ yield in the PBR, increased with decreasing feed flow rate (Figure 4.7 (c)). The H₂ permeance at these reaction conditions increased with decreasing feed flow rate (Figure 4.7 (c)), but the values were in a similar range as the single gas permeance results presented before. Figure 4.7 (d) shows the C₂H₄ yield enhancement as a function of the operability level coefficient (OLC), which is defined as the ratio of the actual permeation rate and the actual formation rate of the H₂ in the reaction condition. The C₂H₄ yield enhancement increased with increasing OLC as the feed flow rate was decreased. This indicates that the OLC is a useful parameter for describing the performance of a membrane reactor.

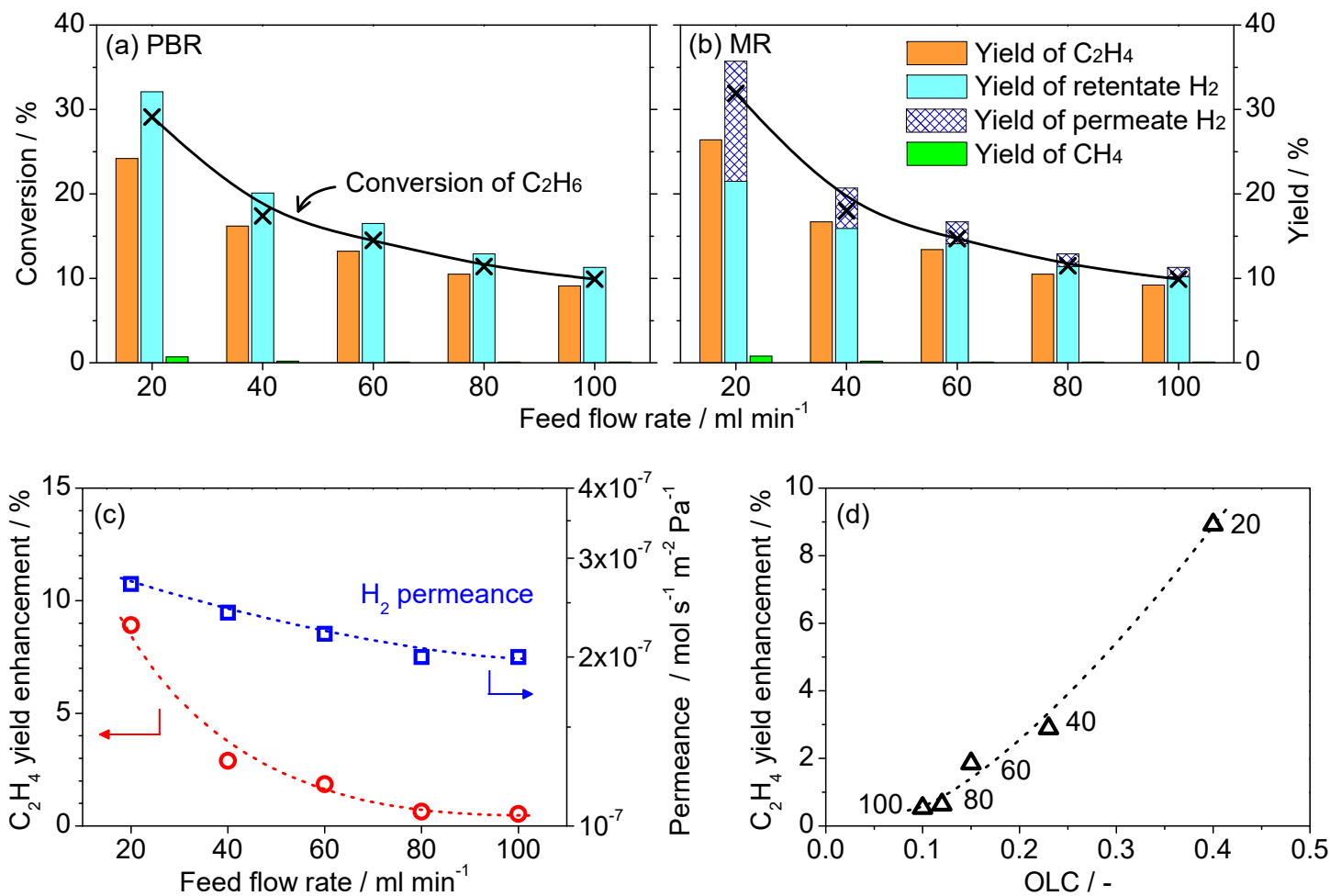


Figure 4.7. Conversion of C₂H₆ and yields of C₂H₄, H₂ and CH₄ for dehydrogenation of ethane at feed flow rates in the range of 20-100 cm³ min⁻¹ at 823 K and 0.1 MPa using 20 % C₂H₆ diluted in Ar. (a) PBR (b) MR (c) Yield enhancement and H₂ permeance as feed flow rate

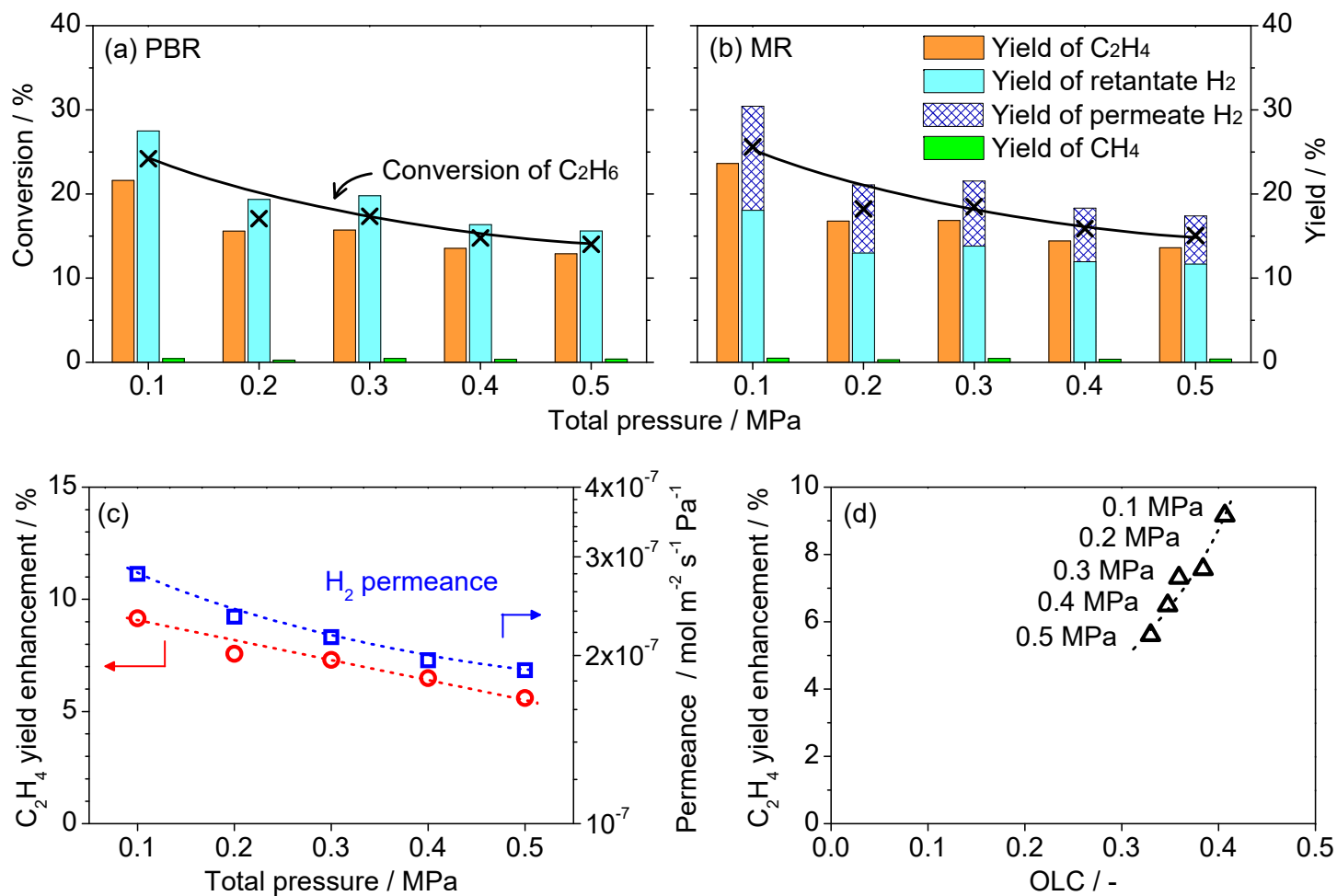


Figure 4.8. Conversion of C_2H_6 and yields of C_2H_4 , H_2 and CH_4 for dehydrogenation of ethane at various total pressures 0.1-0.5 MPa and 823 K. (a) PBR (b) MR (c) Yield enhancement and H_2 permeance as feed total pressure

4.3.5. Effect of total pressure on ethane dehydrogenation in PBR and MR

The effect of pressure on the dehydrogenation of ethane in the PBR and the MR was investigated at 823 K at various pressures (0.1 – 0.5 MPa) with $20 \text{ cm}^3 \text{ min}^{-1}$ of 20 % ethane diluted in Ar. In order to keep the residence time constant, the feed was continuously supplied to the reactor with the overall feed flow rate increasing in proportion to the pressure. Figure 4.8 (a, b) shows the conversion of C_2H_6 and the yields of C_2H_4 , H_2 and CH_4 as a function of the pressure in the PBR and the MR. In the PBR (Figure 4.8 (a)), the conversion and yields decreased with increasing pressure from 24 % for 0.1 MPa to 14 % for 0.5 MPa, and this is in accordance with Le Chatelier's principle since the stoichiometry of ethane dehydrogenation results in a net increase in moles, which is disfavored with increasing pressure.

The trends of the conversion and yields in MR were similar to these in the PBR, but the conversion and yields were higher in the MR at all pressures (Figure 4.8 (b)). This is also explained by Le Chatelier's principle, since selective removal of the product hydrogen through the membrane shifts the equilibrium of the reaction and increases the conversion and yields. The H_2 permeance at the reaction conditions was in a similar range as the permeances that were obtained in the single gas permeance measurements, but the permeance decreased even though the pressure increased (Figure 4.8 (c)). This result could be due to the constant flow rate of sweep gas ($100 \text{ cm}^3 \text{ min}^{-1}$), which was used at all reaction conditions and which may not here been sufficient at higher pressure. From the result of activity and the H_2 permeance, the enhancement of the C_2H_4 yield in the MR mode decreased with increasing total pressure (Figure 4.8 (c)). A relation between the C_2H_4 yield enhancement and the OLC is shown in Figure 4.8 (d). The C_2H_4 yield enhancement increased with increasing OLC as the total pressure decreased.

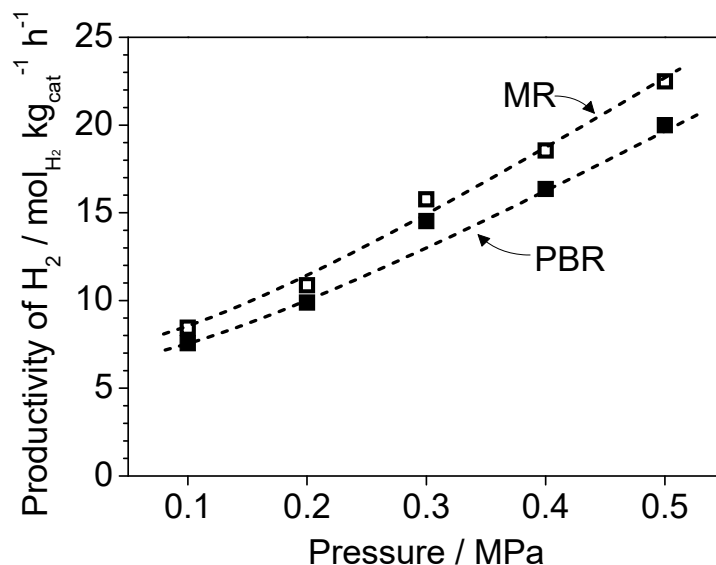


Figure 4.9. Productivity of H₂ for dehydrogenation of ethane in the MR and PBR at various total pressures 0.1-0.5 MPa and 823 K.

Figure 4.9 shows the productivity of H₂, obtained from the molar flow rate of produced H₂ normalized by the weight of catalyst, in the PBR and MR as a function of total pressure. Although the conversion of C₂H₆ and the yields of C₂H₄ and H₂ decreased with increasing total pressure (Figure 4.8), the productivity of H₂ increased with increasing pressure in the PBR and MR. This is because the decrease in conversion is more than affect by the increase in inlet flow rate. In addition, the productivity of H₂ was higher in the MR than in the PBR, especially at high pressure.

4.3.6. Effect of temperature on ethane dehydrogenation in PBR and MR

The effect of temperature on the dehydrogenation of ethane in the PBR and the MR was also investigated in temperature range of 723-823 K at 0.1 MPa with 20 cm³ min⁻¹ of 20 % ethane diluted in Ar, and the conversion of C₂H₆ and yields of C₂H₄, H₂ and CH₄ are shown in Figure 4.10 (a, b). In both reactors, the conversion of C₂H₆ and yields

of C₂H₄ and H₂ increased with increasing temperature because the dehydrogenation of ethane is an endothermic reaction. However, the yield of CH₄, which is the side product, also increased with increasing temperature due to the coking and cracking as side reactions. In the MR, the C₂H₄ yield increased at all temperatures and the C₂H₄ yield enhancement rose and was highest at 823 K at 7 % (Figure 4.10 (c)). The H₂ permeance was very stable during the activity tests showing a permeance of $2\text{-}3 \times 10^{-7} \text{ mol m}^{-2} \text{ s}^{-1} \text{ Pa}^{-1}$. Figure 4.10 (d) shows that the C₂H₄ yield enhancement correlates well with the OLC with changes of temperature, again indicating that the OLC is a useful descriptor of the reactor performance.

4.3.7. Effect of membrane properties on yield enhancement

The effect of membrane properties on the enhancement of C₂H₄ yield for the dehydrogenation of ethane was investigated with different hydrogen selective membranes at 823 K and 0.1 MPa with $20 \text{ cm}^3 \text{ min}^{-1}$ of 20 % ethane over 0.2 g of 5 wt.% Cr/ZSM-5 catalyst. In the present study VTES-derived silica membranes were mostly used in the membrane reactor studies, but this section describes a silica-zirconia composite membrane for comparison. The silica-zirconia membrane has lower H₂ permeance but larger H₂/C₂H₆ selectivity. The H₂ permeance and H₂/C₂H₆ selectivity of the membranes at reaction conditions and the enhancement of C₂H₄ yield are summarized in Table 4.5. Comparison of enhancements of C₂H₄ yield shows that a higher H₂ permeance is more important than selectivity for the enhancement of the C₂H₄ yield from 7.3 to 12.1 %. This supports earlier findings that selectivity about 100 did not affect membrane reactor performance [11].

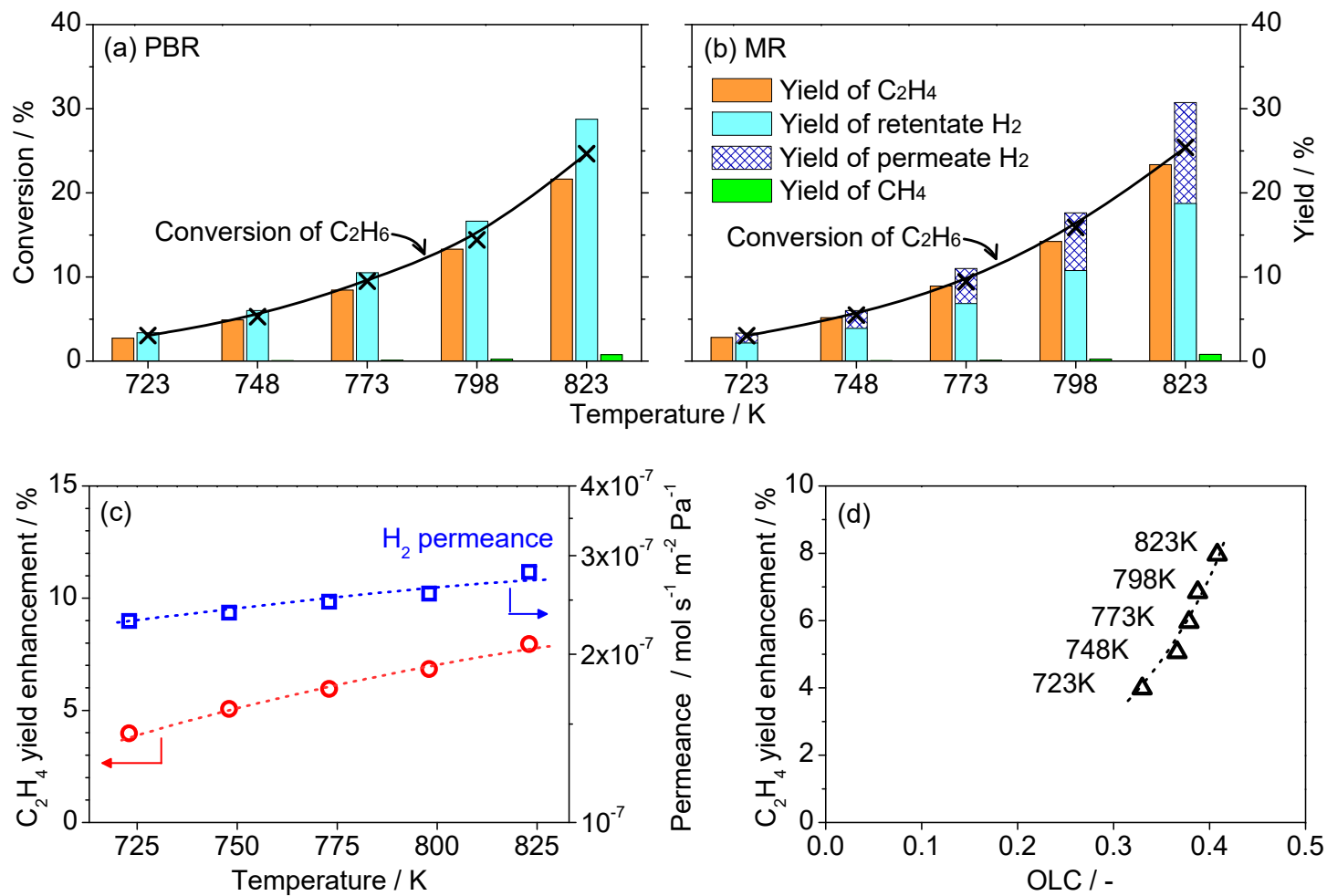


Figure 4.10. Conversion of C_2H_6 and yields of C_2H_4 , H_2 and CH_4 for dehydrogenation of ethane at various temperatures from 723 K to 823 K and 0.1 MPa. (a) PBR (b) MR (c) Yield enhancement and H_2 permeance as temperature

Table 4.5.

Enhancement of C₂H₄ yield for dehydrogenation of ethane in membrane reactor with different membranes at 823 K and 0.1 MPa with 20 cm³ min⁻¹ of 20 % ethane

| Membrane | H ₂ permeance / mol m ⁻² s ⁻¹ Pa ⁻¹ | H ₂ /C ₂ H ₆ Selectivity / - | OLC / - | Enhancement of C ₂ H ₄ yield / % |
|---|---|---|---------|--|
| SiO ₂ -ZrO ₂ ^[9] | 1.9 × 10 ⁻⁷ | 4300 | 0.34 | 7.3 |
| VTES-derived SiO ₂ | 4 × 10 ⁻⁷ | 240 | 0.47 | 12.1 |

The enhancement of C₂H₄ yield was also obtained by simulation with a 1-dimensional model using various H₂ permeances and H₂/C₂H₆ selectivities. Fig. 4.11 (top) shows the C₂H₄ yield as a function of contact time with different H₂ permeances. Here, the H₂ permeance was varied from 0 to 10⁻⁶ mol m⁻² s⁻¹ Pa⁻¹, and the selectivity of H₂/C₂H₆ was fixed at infinity in all cases. The points are experimental values and the lines are calculated values. Comparison with the experimentally obtained H₂ permeance in the range of 2-3 × 10⁻⁷ mol m⁻² s⁻¹ Pa⁻¹, the calculated values showed good agreement with the experimental values. The C₂H₄ yield increased with the increase of H₂ permeance, and the yield was 51 % at a H₂ permeance of 10⁻⁶ mol m⁻² s⁻¹ Pa⁻¹. Figure 4.11 (bottom) shows the enhancement of C₂H₄ yield as a function of the OLC value, which is the ratio of the permeation rate and the formation rate of hydrogen. The points are experimental values, which were shown in Table 4.5, and the lines are calculated values. The simulated values agreed well with the experimental values. The enhancement of C₂H₄ yield increased with the increase of H₂ permeance and H₂/C₂H₆ selectivity. When the H₂/C₂H₆ selectivity was higher than 100, the enhancement of C₂H₄ yield was higher than 25 % at a H₂ permeance of the order of 10⁻⁶ mol m⁻² s⁻¹ Pa⁻¹. However, when the selectivity was 10, the enhancement of C₂H₄ yield decreased after

the H_2 permeance of $5 \times 10^{-7} \text{ mol m}^{-2} \text{ s}^{-1} \text{ Pa}^{-1}$ because the increasing C_2H_6 reactant permeance resulted in loss of the reactant on the reaction side. The results show that a selectivity of 100 is sufficient to achieve high membrane reactor performance.

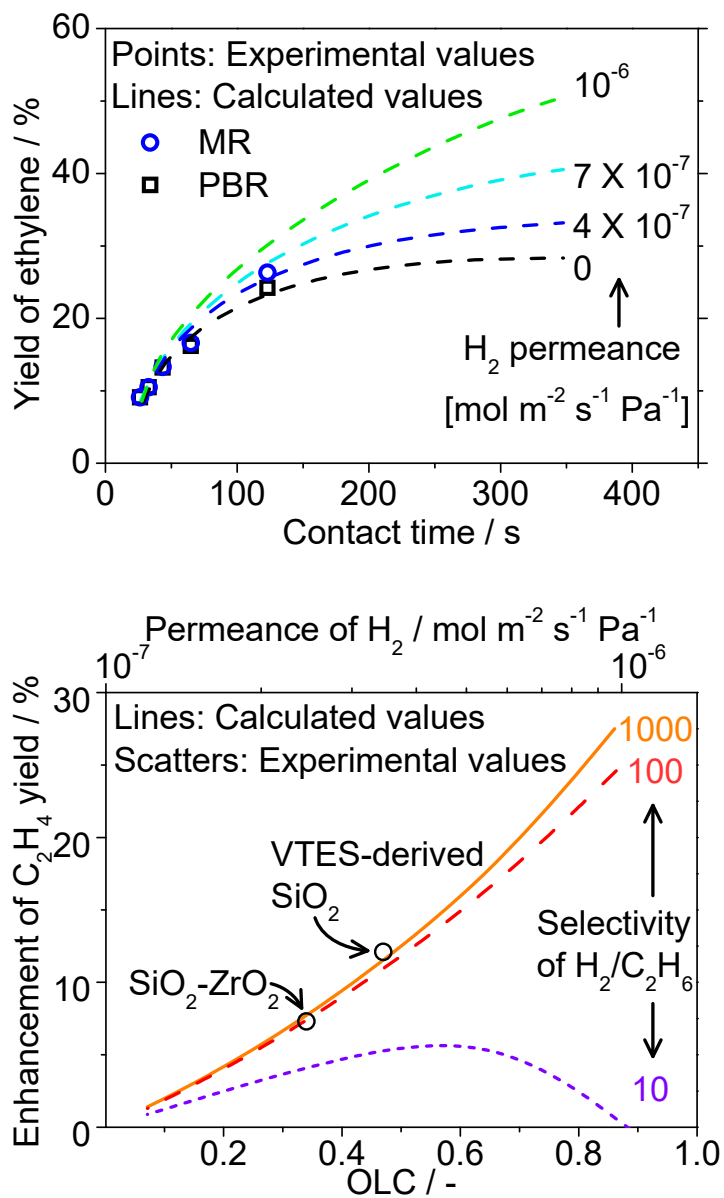


Figure 4.11. Experimental and calculated values of the C_2H_4 yield as a function of contact time (top) and the enhancement of C_2H_4 as a function of OLC (bottom)

4.4. Conclusions

The dehydrogenation of ethane was conducted over a 5 wt% Cr/ZSM-5 catalysts in a conventional packed-bed reactor (PBR) and in a membrane reactor (MR) fitted with hydrogen selective silica membranes. The silica membrane was prepared by the chemical vapor deposition of vinyltriethoxysilane (VTES) at 873 K, and the membrane had a high H₂ permeance of $4 \times 10^{-7} \text{ mol m}^{-2} \text{ s}^{-1} \text{ Pa}^{-1}$ with H₂/C₂H₆ selectivity of 240 at 823 K, respectively. The H₂ permeance at reaction conditions was similar to that obtained with single gas permeance measurement in the range of $3 \times 10^{-7} \text{ mol m}^{-2} \text{ s}^{-1} \text{ Pa}^{-1}$.

Cr/ZSM-5 catalysts were successfully synthesized, which were characterized by Brunauer-Emmett-Teller (BET), X-ray diffraction (XRD) and X-ray absorption fine-structure (XAFS) measurements. The analyzed results showed that a large proportion of the catalyst was Cr₂O₃.

The effect of various reaction conditions including feed flow rates, total pressures and temperatures on the dehydrogenation of ethane were investigated in the PBR and the MR. At all conditions, conversion of C₂H₆ and yields of C₂H₄ and H₂ in the MR were higher than those in the PBR. Another result was that the productivity in H₂ formation increased with increasing pressure even though the conversion of C₂H₆ and yield of C₂H₄ and H₂ decreased.

A C₂H₄ yield enhancement and an operability level coefficient (OLC) were used to evaluate the MR, and C₂H₄ yield enhancement was correlated with the OLC values. The enhancement of C₂H₄ yield was obtained from modeling simulation with various H₂ permeances and H₂/C₂H₆ selectivities. The enhancement of C₂H₄ yield was higher than 25 % at a H₂ permeance of the order of $10^{-6} \text{ mol m}^{-2} \text{ s}^{-1} \text{ Pa}^{-1}$ and a H₂/C₂H₆ selectivity of 100.

Reference

- [1] J.J.H.B. Sattler, J. Ruiz-Martinez, E. Santillan-Jimenez, B.M. Weckhuysen, Catalytic dehydrogenation of light alkanes on metals and metal oxides, *Chem. Rev.* 114 (2014) 10613-10653.
- [2] D. Lippe, Planned maintenance to slow first-half 2016 ethylene production, *Oil Gas J.* 114 (2016) 62-69.
- [3] F. Gallucci, E. Fernandez, P. Corengia, M. van Sint Annaland, Recent advances on membranes and membrane reactors for hydrogen production, *Chem. Eng. Sci.* 92 (2013) 40-66.
- [4] A.M. Avila, Z. Yu, S. Fazli, J.A. Sawada, S.M. Kuznicki, Hydrogen-selective natural mordenite in a membrane reactor for ethane dehydrogenation, *Microporous Mesoporous Mater.* 190 (2014) 301-308.
- [5] E. Gobina, R. Hughes, Ethane dehydrogenation using a high-temperature catalytic membrane reactor, *J. Membr. Sci.* 90 (1994) 11-19.
- [6] E. Gobina, K. Hou, R. Hughes, Ethane dehydrogenation in a catalytic membrane reactor coupled with a reactive sweep gas, *Chem. Eng. Sci.* 50 (1995) 2311-2319.
- [7] J.P. Collins, R.W. Schwartz, R. Sehgal, T.L. Ward, C.J. Brinker, G.P. Hagen, C.A. Udovich, Catalytic dehydrogenation of propane in hydrogen permselective membrane reactors, *Ind. Eng. Chem. Res.* 35 (1996) 4398-4405.
- [8] J.-A. Medrano, I. Julian, J. Herguido, M. Menendez, Pd-Ag membrane coupled to a two-zone fluidized bed reactor (TZFBR) for propane dehydrogenation on a Pt-Sn/MgAl₂O₄ catalyst, *Membranes* 3 (2013) 69-86.
- [9] S.-J. Ahn, A. Takagaki, T. Sugawara, R. Kikuchi, S.T. Oyama, Permeation properties of silica-zirconia composite membranes supported on porous alumina substrates, *J. Membr. Sci.* 526 (2017) 409-416.
- [10] S.T. Oyama, H. Lim, An operability level coefficient (OLC) as a useful tool for correlating the performance of membrane reactors, *Chem. Eng. Sci.* 151 (2009) 351-358.
- [11] H. Lim, Y. Gu, S.T. Oyama, Studies of the effect of pressure and hydrogen permeance on the ethanol steam reforming reaction with palladium- and silica-based membranes, *J. Membr. Sci.* 396 (2012) 115-127.

-
- [12] F.W. Kutzler, C.R. Natoli, D.K. Misemer, S. Doniach, K.O. Hodgson, Use of one-electron theory for the interpretation of near edge structure in K-shell x-ray absorption spectra of transition metal complexes, *J. Chem. Phys.* 73 (1980) 3274-3288.
- [13] N. Mimura, M. Okamoto, H. Yamashita, S.T. Oyama, K. Murata, Oxidative dehydrogenation of ethane over Cr/ZSM-5 catalysts using CO₂ as an oxidant, *J. Phys. Chem. B* 110 (2006) 21764-21770.
- [14] M.S. Kumar, N. Hammer, M. Ronning, A. Holmen, D. Chen, J.C. Walmsley, G. Oye, The nature of active chromium species in Cr-catalysts for dehydrogenation of propane: New insights by a comprehensive spectroscopic study, *J. Catal.* 261 (2009) 116-128.
- [15] A. Virnovskaia, E. Rytter, U. Olsbye, Kinetic and isotopic study of ethane dehydrogenation over a semicommercial Pt,Sn/Mg(Al)O catalyst, *Ind. Eng. Chem. Res.* 47 (2008) 7167-7177.
- [16] V. Galvita, G. Siddiqi, P. Sun, A.T. Bell, Ethane dehydrogenation on Pt/Mg(Al)O and PtSn/Mg(Al)O catalysts, *J. Catal.* 271 (2010) 209-219.

Chapter 5

General Conclusions

This thesis deals with the study on hydrogen selective silica-based membranes for ethane dehydrogenation over Cr/ZSM-5 catalyst. First, silica-based membranes were developed to improve their permeability and hydrothermal stability by modifying precursors.

A hydrogen-selective silica-zirconia composite membrane was prepared on a macroporous alumina support by chemical vapor deposition of tetraethylorthosilicate (TEOS) and zirconium (IV) *tert*-butoxide (ZTB) at 923 K. The resulting membrane had a high H₂ permeance of $3.8 \times 10^{-7} \text{ mol m}^{-2} \text{ s}^{-1} \text{ Pa}^{-1}$ with selectivities over CO₂, N₂ and CH₄ of 1100, 1400 and 3700, respectively. Studies of the temperature dependence of the permeance of He, H₂, and Ne demonstrated that the permeation mechanism was similar to that of dense silica membranes, involving solid-state diffusion with jumps of the permeating species between solubility sites. Parameters such as the site density, jump distance, and jump frequency were calculated and were physically plausible, and varied in reasonable manner with the mass and size of He, H₂, and Ne. An alternative mechanism involving an activated gas translational mechanism was shown to fit the data but to give physically unrealistic parameters. The silica-zirconia membrane showed hydrothermal stability over a limited testing period of 48 h. After exposure to 16 mol% water vapor at 923 K for 48 h, a pure silica membrane showed a 68 % decline with a H₂ permeance $4.5 \times 10^{-8} \text{ mol m}^{-2} \text{ s}^{-1} \text{ Pa}^{-1}$ and a H₂ over N₂ selectivity of 800, both of which continued to deteriorate. In comparison, a 10 % ZrO₂-SiO₂ membrane showed a decline

of 56 % but to a level of 10^{-7} mol m⁻² s⁻¹ Pa⁻¹ with a H₂ over N₂ selectivity of 5700. Importantly, the deterioration largely stabilized at that point.

Hydrogen-selective silica membranes were prepared on a macroporous alumina support by chemical vapor deposition (CVD) of vinyltriethoxysilane (VTES) at 873 K at atmospheric pressure. The membrane had a high H₂ permeance of 5.4×10^{-7} mol m⁻² s⁻¹ Pa⁻¹ with H₂ selectivity over CO₂, N₂, CO and CH₄ of 95, 170, 170 and 480, respectively. In situ Fourier transform infrared (FTIR) measurements after CVD on an alumina disk at the same conditions as for the membrane preparation showed that the vinyl groups remained in the silica structure. The temperature dependence of the permeance of various molecules (He, Ne, H₂, CO₂, N₂, CO, CH₄) before and after hydrothermal treatment gave information about the mechanism of permeance and the structure of the membrane. The membrane was composed of a contiguous silica network through which small species permeated by a solid-state mechanism and a small number of pores through which the large molecules diffused. The silica-based structure became more compact after hydrothermal treatment with decreasing permeance of small molecules (He, Ne, H₂), while small pores were enlarged increasing permeance of large molecules (CO₂, N₂, CO, CH₄). Calculation results for the small species based on a mechanism involving jumps of the permeating species between solubility sites showed lower activation energy and larger jump distances than those of a TEOS-derived silica membrane. The retention of the vinyl groups in the structure mostly associated with the defect pores resulted in interactions with CH₄ and CO₂, so that these species permeated by a surface diffusion mechanism.

Finally, the dehydrogenation of ethane ($C_2H_6 \rightarrow C_2H_4 + H_2$) over 5 wt% Cr/ZSM-5 catalysts was studied in a conventional packed-bed reactor (PBR) and in a membrane

reactor (MR) fitted with the hydrogen selective silica-based membranes at various feed flow rates, total pressures and temperatures. The membranes were prepared by chemical vapor deposition (CVD) of vinyltriethoxysilane (VTES) at 873 K and had a high H₂ permeance of $2.7 \times 10^{-7} \text{ mol m}^{-2} \text{ s}^{-1} \text{ Pa}^{-1}$ with a H₂/C₂H₆ selectivity of 250 and a H₂/C₂H₄ selectivity of 240 at 573 K. The presence of a Cr₂O₃ phase in the 5 wt% Cr/ZSM-5 catalysts was confirmed by X-ray diffraction (XRD) and X-ray absorption fine-structure (XAFS) measurements. At all reaction conditions, conversion of C₂H₆ and yields of C₂H₄ and H₂ in the MR were higher than those in the PBR. The yield enhancement of C₂H₄ and an operability level coefficient (OLC) were used to evaluate the MR, and the C₂H₄ yield enhancement was well correlated with the OLC values. The enhancement of C₂H₄ yield was also obtained from the experiment and modeling simulation with various H₂ permeances and H₂/C₂H₆ selectivities. The enhancement of C₂H₄ yield was higher than 25 % at H₂ permeance of the order of $10^{-6} \text{ mol m}^{-2} \text{ s}^{-1} \text{ Pa}^{-1}$ and the H₂/C₂H₆ selectivity of 100, but considered both the H₂ permeance and H₂/C₂H₆ selectivity the enhancement would be lower than the estimated values.

Based on the overall results in this thesis, several future works can be considered:

- Model simulation for ethane dehydrogenation would be improved by considering kinetic rate expressions based on Langmuir-Hinshelwood and using 2- or 3-dimensional model.
- The enhancement of ethylene yield could be enhanced by applying high H₂ permeance of around $10^{-6} \text{ mol m}^{-2} \text{ s}^{-1} \text{ Pa}^{-1}$ and the H₂/C₂H₆ selectivity over 100.
- The carbon dioxide-assisted dehydrogenation of ethane in membrane reactor could be effective process with solving coke formation and improvement of ethylene yield.